UNIVERSIDADE D
COIMBRA

Patrícia Pinto dos Santos

Phosphorescence lifetime imaging of O_2 sensitive biomarkers using a single pixel detector

Dissertation in the context of the Master in Biomedical Engineering, Specialization in Biomedical Instrumentation advised by Prof. João Cardoso and PhD Pedro Vaz and presented to the Faculty of Sciences and Technology / Department of Physics.

August, 2021

Phosphorescence lifetime imaging of O_2 sensitive biomarkers using a single pixel detector

Supervisor:

Professor João Manuel Rendeiro Cardoso

Co-Supervisor:

PhD Pedro Guilherme Vaz

Jury:

Professor João Sérgio Seixas de Melo

Professor João Manuel Rendeiro Cardoso

Professor Luís Alberto da Silva Cruz

Dissertation submitted in partial fulfillment for the degree of Master of Science in Biomedical Engineering.

Coimbra, 2021

This work was developed in collaboration with:

LIBPhys-UC

Esta cópia da tese é fornecida na condição de que quem a consulta reconhece que os direitos de autor são pertença do autor da tese e que nenhuma citação ou informação obtida a partir dela pode ser publicada sem a referência apropriada.

This copy of the thesis has been supplied on condition that anyone who consults it is understood to recognize that its copyright rests with its author and that no quotation from the thesis and no information derived from it may be published without proper acknowledgement.

Acknowledgements

Começo por agradecer aos meus orientadores, Professor João Cardoso pelo apoio ao desenvolvimento do projeto, e ao Professor Pedro Vaz pela enorme disponibilidade, ajuda e partilha! Muito obrigada!

Agradeço aos meus amigos de Coimbra, em especial à Rita Trindade e à Beatriz Santos! Ao longo dos últimos 5 anos, são incontáveis as horas que passamos juntas! Obrigada pelas longas sessões de estudo, pela motivação gigante e, no fundo, por me levarem a ser melhor pessoa!

Também agradeço à Alexandra Pereira que nos últimos anos se tornou minha companheira inseparável de trabalho, com quem passei horas e horas e criei uma ligação especial!

Obrigada aos meus colegas de ERASMUS, Joana Fernandes (a minha colega de quarto e pessoa absolutamente brilhante!), Daniel Bastos e Bernardo Plácido, por todas as aventuras, todas as viagens e por me ensinarem a viver a vida de forma mais descontraída!

Ao Luís Benedito, o amigo das conversas improváveis e de longas caminhadas de reflexão, deixo um grande obrigada!

Agradeço ao Diogo Santos, pela companhia e apoio dos últimos 3 anos, por estar sempre comigo e por ter tornado a minha vida e este percurso mais fácil, leve e bonito!

Por fim, o meu profundo obrigada aos meus pais por todo o esforço, colo, apoio e força! Obrigada por estarem sempre ao meu lado e me darem a liberdade que preciso! Obrigada pela coragem que me dão todos os dias e por nunca me deixarem desistir! A sorte gigante que é ter-vos como pais!

Obrigada!

"The important thing is not to stop questioning. Curiosity has its own reason for existing."

— Albert Einstein

Resumo

A imagiologia de pixel único é uma técnica de imagem recente capaz de reconstruir imagens, usando um único elemento sensor. Uma câmara de pixel único tem uma arquitetura simples e é capaz de chegar a regiões do espetro às quais as câmaras convencionais não chegam ou necessitariam de uma intrumentação complexa e cara. A IPU está normalmente associada aos conceitos de aquisição comprimida. A acquisição comprimida é uma estratégia de amostragem que permite reconstrução de imagens com um conjunto de medições sub-Nyquist, que permite reduzir o tempo de aquisição, mantendo uma boa qualidade de imagem.

Neste trabalho foi desenvolvida uma câmara de pixel único que permite obter simultaneamente imagens de fosforescência de intensidade e tempo de vida de amostras que contêm um biomarcador de oxigénio, cuja fosforescência diminui fortemente na presença de O_2. Assim, para estudar a eficiência deste esquema experimental, duas células de fluxo que contêm uma solução de tolueno com a mesma concentração do biomarcador foram colocadas lado a lado. Uma das células foi desoxigenada, enquanto a outra tem a mesma quantidade relativa de oxigénio que a atmosfera. As amostras foram estimuladas com luz com codificação espacial, padrões de Hadamard, no intervalo de 428-640 nm. A luz refletida ou transmitida pelas células, que têm um pico de emissão nos 756 nm, é coletada pelo fotodetetor. O algoritmo de reconstrução TVAL3 reconstruiu as imagens com rácios de compressão de 25%, 10%, 5% e 1%. Em ambos os mapas de fosforescência de intensidade e de tempo de vida, a amostra desoxigenada foi identificada, enquanto a oxigenada não, não tendo sido possível distingui-la do ruído de fundo. A amostra desoxigenada apresenta um valor médio de tempo de vida de, aproximandamente, 20 μs, para ambas as posições no suporte, e um valor de intensidade médio de 2.1×10^{-3} UA na posição da esquerda e de 4.0×10^{-3} UA para a posição da direita. Os resultados foram consistentes para todos os rácios de compressão, com exceção de 1%. Quanto à amostra oxigenada, os valores de tempo de vida não são consistentes e a intensidade assume valores que rondam os 4.9×10^{-3} UA.

Uma vez provada a eficiência do esquema experimental, o próximo passo consistiu em

estudar a relação entre o tempo de vida de fosforescência com o tempo de ventilação de nitrogénio gasoso. Assim, foi usada uma abordagem de ventilação sequencial para ventilar as amostras e, deste modo, reduzir progressivamente o O_2 existente nas soluções. Nesta parte experimental, as amostras tinham como solvente dimetilsulfóxido e apresentavam diferentes concentrações do biomarcador de oxigénio. As amostras foram sequencialmente ventiladas, 6 vezes, durante 30 segundos, para 3 cenários de ventilação. No primeiro apenas a amostra da esquerda foi ventilada, no segundo, ambas as amostras foram ventiladas, e no terceiro, apenas a amostra da direita foi ventilada. Os mapas de fosforescência de intensidade e tempo de vida conseguem distinguir as duas amostras. A solução mais concentrada apresenta valores de intensidade mais altos, enquanto a menos concentrada apresenta valores mais baixos. Os resultados obtidos são consistentes para ambos os rácios de compressão, 10% e 5%, e não variaram com os tempos de ventilação, não existindo, portanto, nenhuma relação entre o tempo de vida e o tempo de ventilação. Os valores de intensidade da amostra mais concentrada são uma ordem superiores aos da menos. Quanto ao tempo de vida, os valores médios para mais concentrada são menores, no intervalo de 22 μs, do que os da outra amostra, $23 - 24$ μs. Os resultados obtidos não foram os espectáveis e, portanto, é importante fazer alguns melhoramentos no esquema experimental, nomeadamente usar um fotodetetor mais sensível e redesenhar a experiência, no sentido de relacionar diretamente a quantidade de oxigénio com os tempos de vida, recorrendo, para tal, a uma câmara de hipóxia.

Palavras-chave: Câmara de pixel único, Aquisição Comprimida, Imagiologia de fosforescência de intensidade e de tempo de vida, Ventilação de Nitrogénio Gasoso, Biomarcador de oxigénio

Abstract

Single pixel imaging is a recent imaging technique capable of reconstructing images using only one photodetector. Single pixel cameras present a simple architecture, reaching a wide range of spectral regions, which may not be achievable by conventional cameras or reacquire expensive instrumentation. SPI is commonly performed using the compressive sensing concepts. Compressive Sensing is a sampling strategy that enables the scenes to be recovered with a set of sub-Nyquist measurements, which enables to reduce the acquisition time, one of the single pixel imaging drawbacks, while maintaining good image quality.

The designed single pixel camera setup was developed with the goal of performing simultaneous phosphorescence lifetime and intensity imaging of samples containing Pt(II) ring-fused chlorins, an oxygen biomarker, whose phosphorescence is strongly quenched in the presence of oxygen. Thus, to study the experimental scheme efficiency, the scene was composed by two flow cells, placed side by side, containing a toluene solution with the same concentration of the O_2 biomarker. One of the cells was deoxygenated, while the other contained a constant amount of oxygen related with atmospheric O_2. The samples were stimulated with Hadamard patterns, in the range between 428 and 640 nm. The reflected or transmitted light by the cells, peaking at 756 nm, was collected by the photodiode. TVAL3 reconstructed the images of the scene, with 25%, 10%, 5% and 1% compression ratios. In both phosphorescence intensity and lifetime maps, the deoxygenated sample was clearly identified, while the oxygenated one was not distinguished from the background noise. The deoxygenated sample presented a mean lifetime of 20 μs, for both positions on the holder, and a mean intensity of 2.1×10^{-3} AU for the left position and 4.0×10^{-3} AU for the right one. The results were consistent for all sampling ratios, except for 1%. Regarding the oxygenated solution, mean lifetime values were not consistent and the mean intensity was around 4.9×10^{-3} AU.

After proving the single pixel camera efficiency, the next step was to study lifetime dependency over the ventilation time. Thus, a gas nitrogen sequential ventilation approach was used to ventilate the samples, progressively reducing the amount of O_2 in the solutions. In this experiment, the samples contained different oxygen biomarker concentrations, in

dimethyl sulfoxide solvent. The samples were sequentially ventilated 6 times, during 30 seconds, according to 3 distinct ventilation scenarios. In the first, only the left sided sample on the support was ventilated, second both were ventilated, and in the third, only the right solution was ventilated. The phosphorescence intensity and lifetime maps clearly distinguish the two samples. The solution with high concentration presented the higher intensity values, while the least concentrated presented lower. According to the results, there is no relationship between lifetime and GN_2 ventilation time. The results obtained were consistent for both 10% and 5% compression ratios and did not vary significantly across the ventilation time. The intensity mean values of the high concentration solution were an order higher than the low concentration sample. Regarding lifetime, the high concentrated solution presented lower values, ranging from 22 μs, while the other sample presented an interval of $23 - 24$ μs. The results are not in agreement with the expectations, and so, it is necessary to perform some enhancements on the SPC system and on the experiment design, namely, using an hypoxia chamber to relate directly the amount of O_2 with lifetime values.

Keywords: Single Pixel Camera, Compressive Sensing, Phosphorescence intensity and lifetime imaging, Gas Nitrogen Ventilation, Oxygen Biomarker.

Contents

List of Acronyms

ABS-WP	Adaptive Basis Scan by Wavelet Prediction
CCD	Charge Couple Device
CMOS	Complementary Metal-Oxide Semiconductor
CS	Compressive Sensing or Compressive Sampling
DAS	Digital Acquisition System
DLP	Digital Light Processing
DMD	Digital Micromirror Device
DMSO	Dimethyl Sulfoxide
FI	Fluorescence Imaging
FLI	Fluorescence Lifetime Imaging
FMT	Fluorescence Molecular Tomography
FRET	Förster Resonance Energy Transfer
GI	Ghost Imaging
HSI	Hyperspectral Imaging
MSI	Multispectral Imaging
PI	Phosphorescence Imaging
PLI	Phosphorescence Lifetime Imaging
RIP	Restricted Isometry Property
SLM	Spatial Light Modulator

sm-SVI	spatially modulated Selective Volume Illumination
SPC	Single Pixel Camera
SPI	Single Pixel Imaging
SPIM	Selective Plane Illumination Microscopy
SVI	Selective Volume Illumination
TCSPC	Time-Correlated Single Photon Counting
TVAL3	Total Variation minimization Augmented Lagrangian and ALternating direction ALgorithms

List of Figures

List of Tables

1 Introduction

1.1 Motivation

Fluorescence and phosphorescence lifetime imaging (FLI/PLI) are luminescence imaging methods that have been increasingly studied and used in bioscience. Contrarily to other imaging techniques, FLI and PLI not only provide the distribution map of the probe, but also a functional image, in which lifetime is studied in function of a biological parameter, such as oxygen, pH, temperature, etc, [1]. Oxygen sensing is the most developed and advanced application of PLI. The design of probes with a sharp response to O_2, while having a reduced response to other biological environments, is relatively easy [1]. Oxygen biomarkers change their spectral phosphorescence response according to the amount of oxygen present. By taking advantage of this behaviour, a wide range of applications are valuable to be explored, because O_2 concentration can provide information on the cell state. Oncological detection is just one of the potential applications [2, 3].

Nowadays, we have at our disposal cameras that rely on pixelated arrays detectors. The conventional 2D sensors are CCD (charge couple device) and CMOS (active pixel sensor based on metal-oxide-conductor). The constant need for better image resolutions leads to a continuous increase of the number of the sensor elements of the detector array. Moreover, the cameras typically have a sampling frequency dictated by the Shannon-Nyquist theorem, which leads to a huge amount of data. The sensors used in lifetime imaging must be capable of collecting the wavelength of the molecule's phosphorescence, with very high frame rates. Therefore, using 2D sensors may be inconvenient, since they are expensive and even unavailable at certain spectral regions.

A solution is to use a single pixel photodetector, employing the math principles of the Compressive Sensing (CS) theory [4]. By using an unidimensional detector, the spectral band limitation is no longer an issue, being possible to reach almost any spectral region of desire. Also, the high frame rates are easier to achieve. Compressive Sensing allows to reduce the amount of information collected by using a lower sampling frequency than the required by the

Nyquist theorem. In this approach, a sequence of binary light patterns illuminates/excites the sample. The resulting light is collected by the photodetector and, with the aid of a reconstruction algorithm, the sample's 2D image is obtained. The versatility of this imaging scheme is valuable to lifetime imaging, since just by changing the photodetector, numerous phosphorescent probes with different emission wavebands may be studied in the future, while maintaining the overall idea and concepts of acquisition and the image reconstruction.

1.2 Goals

The main goal of this thesis was to develop a SPC scheme capable of performing simultaneous phosphorescence lifetime and intensity imaging of an oxygen biomarker, the Platinum(II) 4,5,6,7-tetrahydropyrazolo[1,5-a]pyridine–fused chlorins [5]. The Pt(II) ring-fused chlorins are a near infrared emitting compound, whose phosphorescence is strongly quenched in presence of oxygen. Therefore, to study the experimental setup efficiency, the solution containing the O_2 sensitive biomarker was placed in two cells, positioned side by side. One was ventilated with gas nitrogen, not having O_2, and another presenting the same relative amount of O_2 as in the atmosphere. The two cells presented different spectral behaviours as so, that the lifetime and intensity images were expected to distinguish and localize the oxygenated and deoxygenated samples. After studying the efficiency of SPC scheme, the goal was to understand if there was a relationship between the gas nitrogen ventilation time and lifetime. To do so, three samples containing different amounts of the Pt(II) ring-fused chlorins were sequentially ventilated with GN_2. By each ventilation was expected to reduce the relative amount of oxygen in the cells, leading to increase lifetime values.

The developed SPC can be used for biomedical applications, such as superficial cancer detection or burns. Burnt tissue and carcinogenic cells may present different oxygen levels. By developing adhesives or cream containing an oxygen biomarker compound that could penetrate the skin, it would be possible to determine the areas of the skin presenting low or high oxygen levels.

1.3 Workflow

Figure 1.1 shows the four main tasks developed in this thesis as well as its time table over the last 12 months. The first step was to study the concepts and techniques to understand the development of the SPC scheme and study its efficiency in performing the intensity and lifetime images - Proof-of-concept. The task that followed was to understand if there was a relationship between ventilation time and lifetime. Thus, it was used a Sequential GN_2 ventilation strategy - Pilot Study. The thesis was being written alongside the experimental part.

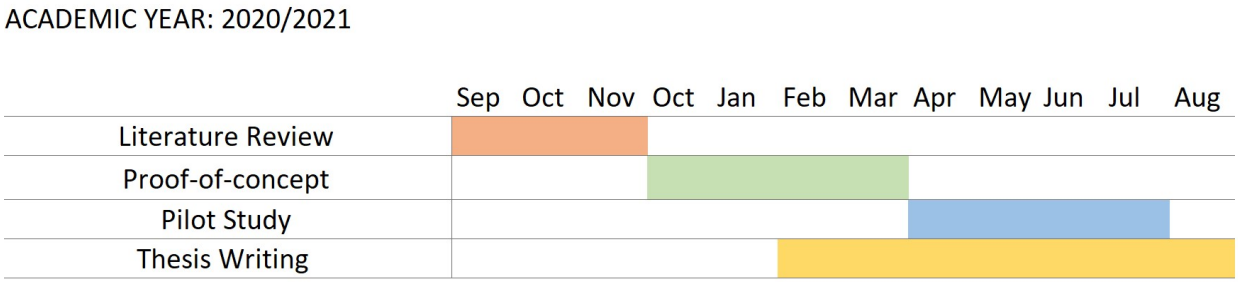

Figure 1.1: Gantt chart of this thesis.

1.4 Research Team

This master thesis was developed during the academic year 2020/2021 at LIBPhys in collaboration with CQC. LIBPhys research center placed at the Physics department at the University of Coimbra, focus its research on Instrumentation, Biomedical Engineering and Radiation Physics. CQC, Coimbra Chemistry Center, at the UC chemistry department is the main research unit dedicated to chemistry.

PhD Pedro Vaz PhD Student Andreia Gaudêncio Professor João Cardoso Professor Miguel Morgado	LIBPhys
Professor Marta Pinheiro Professor Teresa Pinho e Melo PhD Nelson Pereira	CQC

1.5 Scientific Contributions

The scientific contributions resulting from this project were:

Proceedings → Patrícia P. Santos, Pedro G. Vaz, Andreia Sofia F. Gaudêncio, Miguel Morgado, Nelson A. M. Pereira, Marta Pineiro, T. M. V. D. Pinho e Melo, João Cardoso. "Compressive single pixel phosphorescence lifetime and intensity simultaneous imaging - A pilot study using oxygen sensitive biomarkers". Integrated Optics: Design, Devices, Systems and Applications VI. Vol. 11775. International Society for Optics and Photonics, 2021.

Poster → Patrícia P. Santos, Pedro G. Vaz, Andreia Sofia F. Gaudêncio, Miguel Morgado, Nelson A. M. Pereira, Marta Pineiro, T. M. V. D. Pinho e Melo, João Cardoso. "Compressive single pixel phosphorescence lifetime and intensity simultaneous imaging - A pilot study using oxygen sensitive biomarkers". Integrated Optics: Design, Devices, Systems and Applications VI. International Society for Optics and Photonics, 2021. 12 April 2021 (Online).

1.6 Document Structure

This thesis is organized into 5 chapters:

- Chapter 1 - Introduction - presentation of the motivation, goals, workflow, research team and scientific contributions.
- Chapter 2 - Single Pixel Imaging - historical context of single pixel imaging and math principles of compressive sensing are explored, as well as TVAL3 reconstruction algorithm. Explanation of phosphorescence and fluorescence concepts and its potential applications in the biomedical field, employing SPI.
- Chapter 3 - Methods - description of the experimental setup, oxygen biomarker and signal processing used to obtain the results. This chapter is divided in two sections, the proof-of-concept and the Pilot Study.
- Chapter 4 - Results - presentation and discussion on the obtained results of both section, Proof-of-concept and Sequential GN_2 ventilation strategy.
- Chapter 5 - Conclusion - final considerations on the achieved results, acknowledgement of limitations, proposal of improvements and future work.

2 Single Pixel Imaging

Single pixel imaging is a novel and emerging imaging technique that reconstructs 2D and 3D images, using a single photodetector without spatial resolution. The architecture of a single pixel camera is based on two main components - a photodetector and a fast-programmable Spatial Light Modulator (SLM), [6]. The SLM modulates the light projected to the target, whose reflected or transmitted light is collected by the detector as intensity measurements [4]. Intensity values are the input of a reconstruction algorithm that decodes the measurements into spatial information, and so, the image can be obtained.

In this chapter, the single pixel imaging concept is explored, beginning with a historical context, in which SPI's first approaches are described; passing by the math formulation of compressive sensing (a concept commonly associated with SPI) and fluorescence and phosphorescence concepts clarification; and ending with SPI applications, within fluorescence and phosphorescence imaging techniques.

2.1 Context

The first attempt to SPI may date the invention of the flying-spot camera [7]. In 1884, Paul Nipkow proposed a scanning imaging system aiming to transduce visual images into electrical signals, that made use of a disc patterned with equally distanced and sized holes - the Nipkow disc. A light beam illuminates an image and passes through the disc's holes. Each hole scans a segment of the image while a photosensitive cell is positioned after the disc, converting it into an electrical signal. The electrical signal may be transmitted to a distant receiver, where a light bulb varies its brightness and a second Nipkow disc is used to form the image [8]. The Nipkow disc was later used in the first mechanical television, which used a single light detector [6]. However, this was proven to be inefficient.

In 1995, an imaging technique that later inspired the use of spatial light modulation in SPI was suggested - Ghost Imaging (GI) [9]. GI relies on the information collected by two light sensors – a single pixel detector, that measures the light interaction with the

target, and a multi-pixel detector to which the projected light interacts directly – reference [10]. Although GI was first studied from a quantum point of view, using as light source a pair of entangled photons, [11], it can also be considered from a classical perspective. According to [12], ghost imaging can be performed by using a pseudo-thermal source with spatial incoherent light, resulting from a laser passing through a rotating ground glass. In 2008, Shapiro made an improvement to the classical approach. By using a SLM to produce random intensity patterns, it was possible to remove the reference photodetector from the scheme, using only a single pixel detector. This new ghost imaging method was designated as computational ghost imaging, [13].

The "Dual Photography" was the first single pixel system described, in 2005, [14]. A year later, in 2006, Donoho *et al.* proposed a new sampling strategy that enables a signal's reconstruction with less measurements than the ones dictated by the Nyquist-Shannon sampling theorem, [15], named Compressive Sensing. CS concepts were rapidly suggested to be applied to single pixel imaging [16], since they allow a reduction of the number of acquisitions, as well as the acquisition time, one of the drawbacks of SPI [17]. In the past recent years, considering the fast technological advances and the advantages of this imaging system, SPI has increasingly been studied and used to a wide range of applications. See section 2.5.

2.2 Compressive Sensing

Compressive sensing allows a scene to be reconstructed into a N resolution image by M measurements, being $M < N$, if two conditions are satisfied – sparsity and incoherence, [4, 18]. Compression ratio (CR) is defined as the ratio between the set of M scene's measurements and the N resolution of the recovered image.

Sparsity condition is fulfilled when a signal can be represented by high valued coefficients, in a particular orthonormal basis, while the low valued coefficients are removed without significant losses. Mathematically, this idea is described by $x \in \mathbb{R}^{N\times 1}$, a discrete signal, whose sparse representation in a specific orthonormal basis, $\Psi \in \mathbb{R}^{N\times N}$, results in high-valued coefficients containing the majority of the spatial information, $\theta \in \mathbb{R}^{N\times 1}$, [19]:

$$x = \Psi\theta \ . \tag{2.1}$$

Incoherence is related to the sampling process. Each measurement of the scene, y_i, results from the inner product of the x and the sensing matrix used to sample the scene, $\Phi \in \mathbb{R}^{M\times N}$,

$y_i =< x, \Phi_i >, i \in [1, M]$. Taking in consideration the overall measurements, [19]:

$$y = \Phi x \ , \tag{2.2}$$

with $y \in \mathbb{R}^{M \times 1}$. The mathematical formulation that results from the combination of the two conditions is:

$$y = \Phi x = \Phi \Psi \theta = A\theta \ , \tag{2.3}$$

where $A \in \mathbb{R}^{M \times N}$ is the reconstruction matrix that is used in the reconstruction process of the signal x. Figure 2.1 show the matrix representation of the encoding equation of CS.

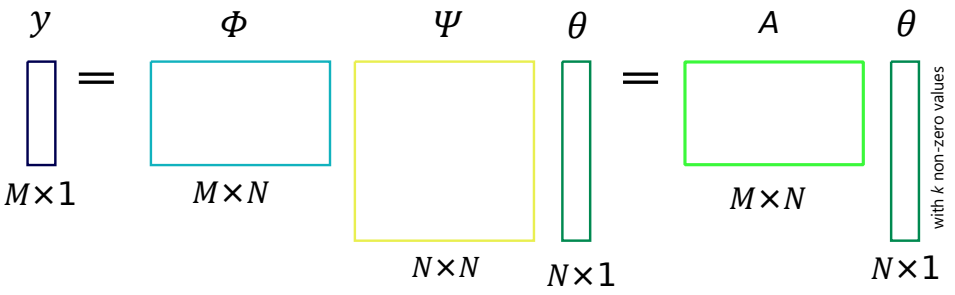

Figure 2.1: Matrix representation of CS equations, presenting the respective dimensions.

2.2.1 Mutual Coherence

Mutual coherence (μ) expresses the coherence between two matrices. If they present correlated elements, the value devolved by the mutual coherence is high; however, if the correlation is low, μ is low as well, [20]. This concept is useful to study the coherence between the sensing matrix and the basis where the signal is sparse, since Φ and Ψ should present low coherence, to assure an efficient reconstruction of the signal. Mutual coherence is mathematically formulated by [20]:

$$\mu(\Phi, \Psi) = \sqrt{N} \cdot \max_{1 \leq k,j \leq n} |\langle \phi_k, \psi_j \rangle| \tag{2.4}$$

with ϕ_k being one vector of the sensing matrix and ψ_j is one of the vectors of the orthonormal matrix responsible for the sparse representation.

2.2.2 Restricted Isometry Property

The photodetector's measurements, y, as in any real system, present some level of noise. Therefore, to measure the robustness of CS and assure an efficient reconstruction, Φ should

obey to the Restricted Isometry Property (RIP), [21, 22]. Each k integer has an isometry constant, δ_k, of a matrix Φ:

$$(1-\delta_k)\|x\|_{\ell_2}^2 \leq \|\Phi x\|_{\ell_2}^2 \leq (1+\delta_k)\|x\|_{\ell_2}^2 \tag{2.5}$$

holds for all x vectors that have exactly k non-zero coefficients. $|...|_{\ell_2}$ is ℓ_2 norm. If δ_k is not close to one, Φ obeys to RIP at k-order. This means that Φ's columns are nearly orthogonal (because it has more rows than columns), [20]. RIP also establishes the number of necessary measurements, M:

$$M \geq cK\log(\frac{N}{K}) \tag{2.6}$$

where c is a constant, [20].

2.2.3 Sensing Matrix

The sparse basis, Ψ, depends on the application, and knowing it *a priori* to choose a sensing matrix that fulfills the incoherence condition and RIP is not ideal. Random matrices were proven to satisfy the incoherence condition and RIP property despite the sparse basis chosen, with high probability, [23]. Matrices with independent and identically entries such as Hadamard can also be used as sensing matrices. Hadamard matrix is an orthogonal squared matrix composed by Walsh functions that only comprehend two values - $+1$ and -1, [24]. The natural order of Hadamard matrices may be computed as, [25, 19]:

$$H_{2^k} = \begin{bmatrix} H_{2^{k-1}} & H_{2^{k-1}} \\ H_{2^{k-1}} & -H_{2^{k-1}} \end{bmatrix} = H_2 \otimes H_{2^{k-1}}, \tag{2.7}$$

being $\otimes$ the Kronecker product, $H_1 = 1$ and 2^k the order of the Hadamard matrix.

Hadarmard matrices present different orderings, besides the natural one, such as Walsh, High Frequency, Block and 'Russian Dolls', [19, 26]. Walsh ordering has the same information as the natural one, but the functions are rearranged in order to increase the number of zero crossings, [25, 19]. The High Frequency order is simply obtained by inverting Walsh ordering Hadamard matrix. Regarding Block, the rows are rearranged in order to increase the groups of pixels with the same value, [7, 19]. 'Russian Dolls' ordering follows 3 rules:

- 1^{st} rule $\rightarrow$ the top half of the rows of a 2^k-ordered Hadamard matrix corresponds to the rows of a $H_{2^{2k-1}}$;

- 2^{nd} rule $\rightarrow$ the third quarter of $H_{2^{2k}}$ matrix corresponds to the transpose matrix of the second quarter;
- 3^{rd} rule $\rightarrow$ the last quarter is ordered accordingly to the number of blocks (the blocks are squares with the same value), [26].

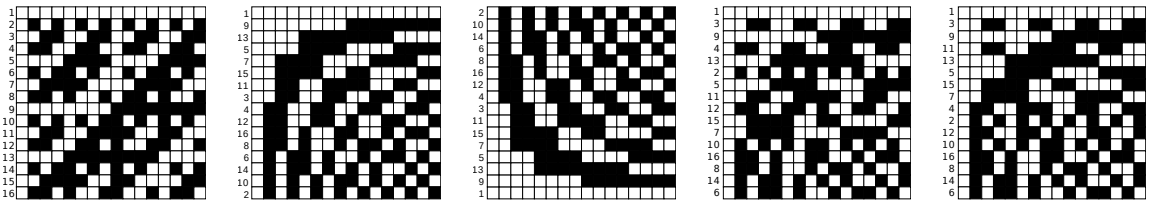

(a) natural (b) Walsh (c) high frequency (d) Block (e) russian dolls

Figure 2.2: Representation of 16^{th} order Hadamard matrices, presenting different orderings. Black squares represent -1, while the white ones correspond to +1. Adapted from [19].

2.3 Reconstruction Algorithm - TVAL3

The sparse coefficients, θ, are calculated by the equation 2.3. Considering its matrices dimensions, the number of unknown variables is higher than the number of equations, causing an algebraic problem. To solve this underdetermined system and get the optimal solutions, *i.e*, the sparsest coefficients vector θ, that produce the set of measurements y, a reconstruction algorithm for sparse signal recovery is normally used. During this work, the Total Variation minimization by Augmented Lagrangian and ALternating direction ALgorithm (TVAL3) was used [27].

When Donoho proposed CS principles, also proved that ℓ_0-minimization, an optimal method for calculating the sparsest coefficients - θ, is equivalent to ℓ_1-minimization, under CS conditions, [15, 27]:

$$\hat{\theta} = \arg\min \|\theta\|_0 \Leftrightarrow \arg\min \|\theta\|_1 \tag{2.8}$$

This equivalency is relevant, since ℓ_0-minimization is computationally demanding. However, several types of sparse signals reconstruction algorithms have been suggested, such as Greedy, Convex, non-Convex, Iterative Threshold, Bergman Iterative and Combinatorial, [28].

In 2009, Chengbo Li proposed a new Total Variation minimization algorithm that gathers Augmented Lagrangian and ALternating direction ALgorithms - TVAL3, [27]. Unlike other

reconstruction algorithms, TVAL3 does not require that the sensing matrices have specific properties, such as orthogonality or normality. Therefore, Φ may be considered universal. Moreover, TVAL3 is a fast algorithm comparatively to others, that finds the optimal solution, *i.e.*, the sparsest gradients, θ, by:

$$\min_{w_i,x} \sum_i \|w_i\|, \text{subjected to } \Phi x = y \text{ and } D_i x = w_i, \text{ for all } i \tag{2.9}$$

where $D_i x \in \mathbb{R}^2$ is the discrete gradient of x in pixel i, and $\|.\|$ is the ℓ_2-norm (the isotropic TV). The augmented Lagrangian function that corresponds to the optimization problem, equation 2.9, is:

$$\mathcal{L}_A(w_i, x) = \sum_i (\|w_i\| - \nu_i^T (D_i x - w_i) + \frac{\beta_i}{2} \|D_i x - w_i\|_2^2) - \lambda^T (\Phi x - y) + \frac{\mu}{2} \|\Phi x - y\|_2^2 \tag{2.10}$$

where $\nu_i \in \mathbb{R}^{2\times 1}$ and $\lambda \in \mathbb{R}^{M\times 1}$ are Lagrangian Multipliers, $\mu \in \mathbb{R}$ and $\beta_i \in \mathbb{R}$.

The augmented Lagrangian method is implemented as an iterative algorithm that minimizes the equation above (2.10). At each interaction ν_i and λ are updated:

$$\tilde{\nu_i} = \lambda - \beta_i (D_i x^* - w_i), \text{ for all } i \tag{2.11}$$

$$\tilde{\lambda} = \lambda - \mu (\Phi x^* - y) \tag{2.12}$$

where x^* and w_i^* are the optimal solutions obtained at each interaction.

Therefore, the objective function with the goal of minimizing x and w_i is defined as:

$$\min_{w_i,x} \mathcal{L}_A(w_i, x) = \min_{w_i,x} \sum_i (\|w_i\| - \nu_i^T (D_i x - w_i) + \frac{\beta_i}{2} \|D_i x - w_i\|_2^2) - \lambda^T (\Phi x - y) + \frac{\mu}{2} \|\Phi x - y\|_2^2 \tag{2.13}$$

The alternating direction algorithm is used at this stage to efficiently solve the equation 2.13. TVAL3 was the reconstruction algorithm used in this work, whose implementation was executed in MATLAB®. The TVAL3 function was extracted and adapted from [29]. The initial conditions, based on [30], to apply TVAL3 were $\mu = 2^8$, $\beta = 2^5$, $\mu_0 = \mu$, $\beta_0 = \beta$, opts.tol = 1e-6, opts.tol_inn = 1e-3, opts.maxit = 1025 and opts.maxcnt = 10.

2.4 Phosphorescence and Fluorescence

Photoluminescence phenomenons are characterized as light emission of certain compounds, after being subjected to a light stimulus [31]. The atom or molecule absorbs the energy, moving its electrons to a higher electronic state and when the electrons relax back to the lower state, they emit light. Within each electronic state there are numerous vibrational levels, in which the electrons can end up to. If an electron in a excited state relaxes to a lower vibrational level, some of the initial energy that led to excitation is lost. Therefore, when the electron returns back to the ground state, the emitted photon has less energy and so, a longer wavelength, than the initial one. This phenomenon corresponds to a fluorescence mechanism [32].

Both fluorescence and phosphorescence are photoluminescence phenomenons. However, while the fluorescence light emission stops immediately after the removal of the excitation source of the stimulus, phosphorescence is defined as a delayed luminescence [31].

From an atomic point of view, each atom's orbital has a maximum of two electrons, each one presenting four quantum numbers n, l, ml and ms, with n being the principal quantum number, l the azimuthal quantum number, ml the magnetic quantum number and ms the spin quantum number. Pauli exclusion principle states that the two electrons in the same orbital must not have the same four quantum numbers, so, the electrons must present opposite spin moments, $m_s = -1/2$ or $m_s = 1/2$ [33]. The spin multiplicity of an energy level is defined by $2S + 1$, where S corresponds to the sum of all spins momentum, which characterizes and gives name to the sates [34].

A singlet state is characterized by having all its electrons paired, so, $2\times(+1/2+(-1/2))+1 = 1$. When the electrons are excited, a singlet excited state or a triplet state are formed. In the first state, the excited electron presents the same spin as it had in the ground state, $2 \times (+1/2 + (-1/2)) + 1 = 1$, whereas, in the triplet state, it presents the same spin as the unpaired electron, $2 \times (+1/2 + (+1/2)) + 1 = 3$, [32]. The spins of the singlet ground and excited sates, as well as the triplet sate are schematized in Figure 2.3.

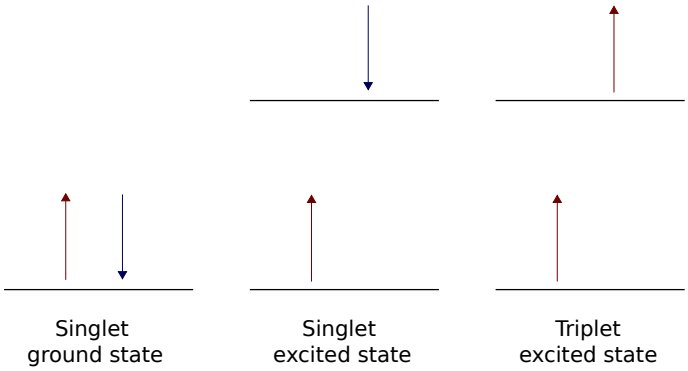

Figure 2.3: Scheme of the electron spins of the singlet ground state, singlet excited state and triplet excited state. Adapted from [32].

Figure 2.4 shows a partial Jablonski diagram, describing the absorption, fluorescence and phosphorescence phenomenons. The relaxation between the singlet excited state and the singlet ground state describes the fluorescence phenomenon. Phosphorescence is characterized by the electron relaxation between the triplet and the ground state. The triplet state may be populated by the singlet excited state by a process called intersystem crossing. Even though the triplet state has lower energy than the singlet excited state, a singlet-to-singlet transition is far more probable to occur than singlet-to-triplet and vice-versa [32]. Due to the electron's spin of the triplet state being equal to the electron's spin of the ground state, the electron relaxation involves a spin inversion, which leads the electron to be stuck in the triplet state, taking a longer period of time to return to the ground state, ranging from 10^{-3} to 10^{2} seconds, [31, 32, 35].

Intensity and lifetime are two phosphorescent/fluorescent measurements. Lifetime refers to the time during which the atom or molecule remains in the excited state and it is obtained by the exponential time decay of the intensity measurements, [36]:

$$I(t) = I_0 e^{-\frac{1}{\tau}t} \tag{2.14}$$

where $I(t)$ is the intensity value at the time t, I_0 is the initial value of intensity and τ is the lifetime. Comparatively, lifetime measurements presents some distinct relevant aspects, since it does not depend on the concentration of the molecule, neither on the excitation intensity, [37]. Since lifetime measurements may present a correlation with a biological parameter, phosphorescence and fluorescence lifetime present more advantages, comparing with intensity.

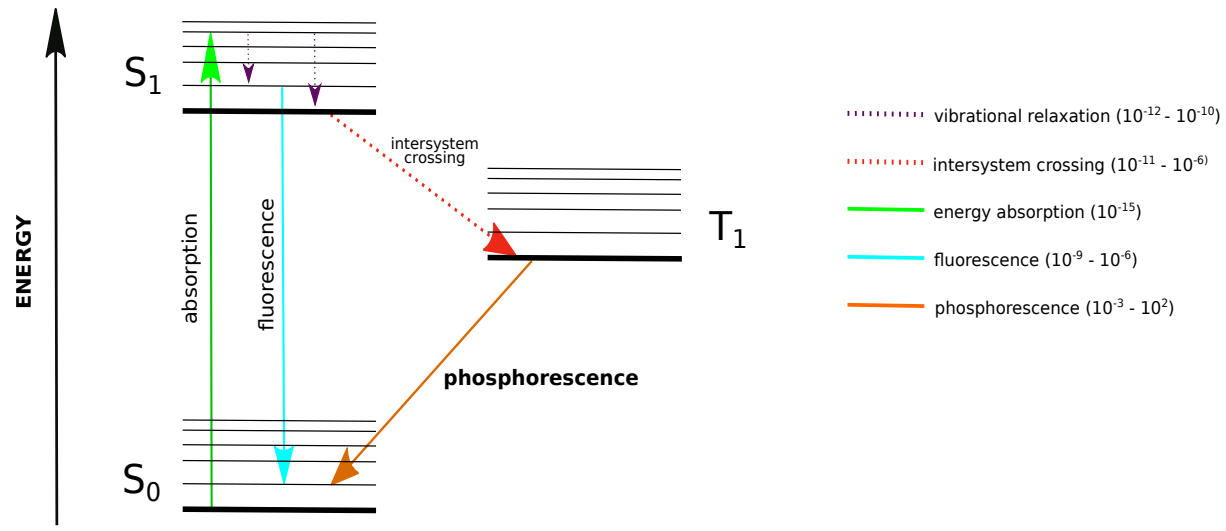

Figure 2.4: Jablonski diagram, describing fluorescence and phosphorescence phenomenons. S_1 is the first excited singlet state and S_0 is singlet ground state. T_1 is the triplet state. The relaxation $S_1 \rightarrow S_0$ represent the fluorescence phenomenon. Phosphorescence requires first an intersystem crossing $S_1 \rightarrow T_1$, switching the spin. Adapted from [38].

2.5 State of the Art

Single pixel cameras present a simple architecture, using only one photodetector. Comparing to conventional imaging sensors, such as CCDs or CMOS, SPI sensor's present a higher filling factor and quantum efficiency [4], being suitable for imaging under scattering media, [39], turbid media, [40], and under weak light conditions, [9]. By being highly versatile and enabling imaging in spectral bands that are unachievable or required very expensive and complex instrumentation, SPCs became a valuable alternative for various applications. 3D imaging [41], real-time video [42], terahertz imaging [43], X-ray imaging [44] or phosphorescence (PI) and fluorescence imaging (FI) [45] are just some examples of SPI applications.

Phosphorescence and fluorescence imaging are imaging techniques that have been increasingly studied and employed, since they enable to visualize biological processes or to monitor some biological parameters, such as pH, temperature, oxygen [46, 1]. Therefore, due to the SPI advantages, experimental SPC schemes for PI and FI have been studied and developed. In the following subsections, fluorescence and phosphorescence imaging applications, using SPI concepts, are described.

2.5.1 Fluorescence Imaging

Fluorescence Microscopic Imaging

Fluorescence microscope was first invented in 1911 [47], and since then, it has been promoting the study of cell's structures and components, as well as molecular and cellular processes. Fluorescence microscopy is an indispensable biomedical research tool, that has been developed and enhanced over the years, as so, that currently 3D microscopic images can be obtained by spatial light modulation, using CS principles [48].

Selective Plane Illumination Microscopy (SPIM) or Light Sheet Fluorescence Microscopy is an optical 3D imaging technique that has been increasingly used in biological applications. The idea behind SPIM is to confine the excitation light to a single plane of the 3D sample and acquire the fluorescence emission with a detector placed in a orthogonal position with respect to the illuminated plane [49]. The high-speed acquisition rate and the low phototoxicity makes SPIM a valuable imaging tool. Another 3D imaging technique was developed with the goal of further increase the volumetric acquisition rate, called Selective Volume Illumination (SVI) [48]. SVI applies the excitation light to a confined volume of interest, using a perpendicular illumination and detection. Figure 2.5 shows a scheme presenting the differences between SPIM and SVI. Calisesi *et. al.* [48] took advantage of SVI and presented a spatially modulated Selective Volume Illumination (sm-SVI) Microscopy setup, employing a Digital Micromirror Device (DMD) to modulate an incoherent light source. With this experimental scheme, it was possible to reduce the number of light modulated patterns by using CS principles and reduce the shadowing artifacts. To study the efficiency of sm-SVI, Calisesi *et. al.* used zebrafish embryos as volumetric samples and applied both SPIM and sm-SVI imaging methods. The obtained images demonstrated that sm-SVI provided less artifacts than SPIM. Also, CS proved to be a useful tool to reduce the acquisition time, and so, the sample's light exposure, even though the image's showed some artifacts for high compression ratios.

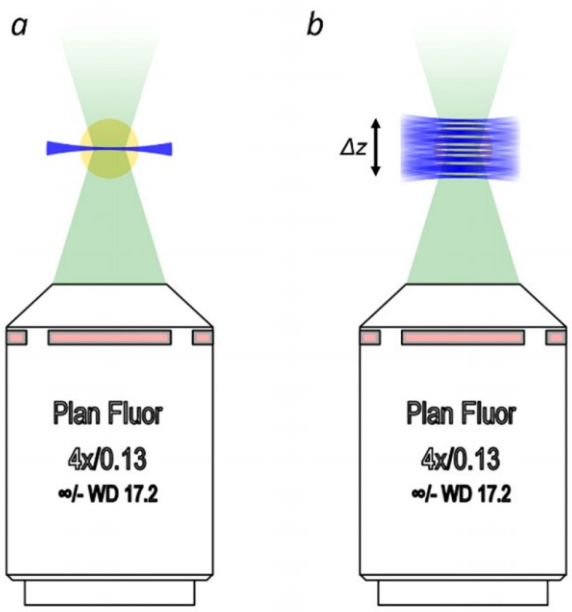

Figure 2.5: Scheme representing in *a* the light sheet illumination and detection and *b* the light modulation in SVI. Extracted from [48].

The increasing development and availability of new techniques, equipment, as well as, fluorescent proteins, dyes and probes enable the noninvasive study of gene expression, protein function, protein to protein interactions and other cell's processes, using fluorescence microscopy [50]. Fluorescence microscopy is essential across all cell and molecular biology and is a major tool to monitor cell's physiological state. Even though fluorescence microscopy provides functional features, it lacks on structural information, since some specimens are transparent to light. Therefore, fluorescence microscopy may be combined with a technique that provides a quantitative structural characterization of transparent specimens, called quantitative phase imaging [51]. Conventional simultaneous fluorescence and phase imaging either employs multiple well-aligned cameras, that requires high alignment skills or uses a single camera with spatial multiplexing, which provides a limited resolution. To overcome this limitations, Liu *et.al* [51] proposed an alignment-free full resolution simultaneous fluorescence and phase imaging, using single-pixel detectors. A proof-of-concept setup was built, where a structural illumination was used to encode both phase and fluorescence of the sample into two detection paths. One path corresponds to the phase imaging of an etched glass and the second to the fluorescence and phase imaging of a quantum dot sample. The results demonstrate a match between fluorescence and phase information matches, proving the efficiency of this setup.

A biopsy is an invasive and time consuming exam consisting of tissue removal and ex-

amination [52]. Fluorescence endomicroscopy is a real time imaging of tissue in *in situ* and can be in some cases used as an alternative to biopsy. Distal and proximal scanning systems are the two categories of conventional endomicroscopy schemes. Unconventional approaches have also been proposed with the goal of obtaining high resolutions with ultra-thin probes. However, these schemes are only suitable for rigid probe imaging, since they require former calibration. Mididoddi *et. al.*, [53], suggested a different strategy, which is to use SPI in image transmission through multimode fibers. Two different schemes were studied and compared, one using galvo mirrors and a diffuser and the other a DMD to generate the patterns. The correlation and stability of the speckle patterns produced by both systems were studied and the results showed they could be adapted to endomicroscopy schemes.

Fluorescence Molecular Tomography

Fluorescence Molecular Tomography (FMT) is a powerful tool for pre-clinical and even clinical studies, since it enables the characterization of a biological tissue in the 3 dimensions, being a valuable technique to reach deep localized fluorophores [54]. FMT presents low spatial resolution comparing with other imaging techniques; therefore, to obtain a 3D molecular map in a proper anatomical basis, FMT should be joint to a structural imaging method, such as computed tomography or magnetic resonance imaging. With the combined knowledge of tissue anatomical and functional properties, it is possible to improve both resolution and sensitivity, [46].

One of the main FMT issues is the huge dataset it generates, that can even be more complex if temporal or spectral information is taken into account. With the purpose of minimizing this problem, Farina *et. al.*, [55], suggested a time-resolved single pixel camera with structured illumination, *i.e.*, a single detector with a DMD and a time correlated single photon counting (TCSPC) to acquire the diffuse light of the target. Therefore, the images could be recovered with a smaller dataset (less acquisitions) using CS.

On a different perspective, Yao *et. al.*, [56], used a wide-field fluorescence tomography to study the performance of FMT when compressive sensing-based preconditioning is applied. The aim was to find the optimal reconstruction, *i.e.*, the preconditioned patterns subset. The results showed that the preconditioning reduces the artifacts and enhances the details in the 3D reconstructions. The best performances were obtained when the structured illumination and detection light were preconditioned independently.

Fluorescence Lifetime Imaging

Fluorescence Lifetime Imaging (FLI) is a powerful imaging tool to characterize and monitor biological parameters and tissues. Contrary to fluorescence intensity measurement, fluorescence lifetime does not depend on the concentration, but rather on the molecular environment (temperature [57], O_2 [58], pH [59], etc). FLI provides a functional image, *i.e.*, an image that depends on a certain biological parameter, being possible to obtain measurements of the metabolic state of the cell, or protein-interaction measurements by FRET (Förster Resonance Energy Transfer) [60, 50].

FRET is a mechanism which describes energy transfer between a donor fluorophore in an excited electronic state and an acceptor [61]. The energy transfer is non radioactive dipole-dipole coupling (electronic interactions between molecules with permanent dipoles), which occurs if both molecules are close to one another (typically 10-100 Å) [62]. Thus, FRET is highly sensitive to the distance. FRET is commonly used to study molecular interactions. Pian *et. al.* [45] performed *in vivo* FRET-FLI experiments to validate his developed time-resolved hyperspectral single-pixel wide-field fluorescence imaging scheme. Fluorescence lifetime images of the bladder and liver of mouses injected with both donor and acceptor transferrins were captured at 725 nm and 777 nm, corresponding to the donor and receptor emission peaks, respectively. These images clearly identify the bladder and the liver, validating the hyperspectral system.

Fluorescence Imaging *via* Multispectral and Hyperspectral SPI schemes

Multispectral imaging (MSI) is an imaging technique used by major microscopy manufacturers, which provides image's data in specific wavelength ranges across the electromagnetic spectrum [63]. MSI overcomes some of the fluorescence imaging problems, such as reducing the autofluorescence, [64].

Multispectral imaging is an important tool for understanding composite materials, since MSI spectrum's result from a mixture of the spectra of different materials. To reach the different endmembers and its relative abundance, it can be used the unmixing method. Song *et. al.* [65] combined these two techniques and proposed an imaging method in which MSI data was acquired by CS based single pixel imaging and processed by an unmixing scheme. To test the developed scheme, mouses were injected with a fluorescent agent. Both fluorescence and autofluorescence spectrum's were studied and the results prove that the scheme can be used for fluorescent imaging of small animals.

Conventional time-resolved multispectral imaging at (sub)nanosecond time scales rely on a point detector or an array connected to a spectrometer and a TCSPC. Imaging at this time frame has several applications, such as fluorescence lifetime imaging. Rousset *et. al.* [66] proposed a multispectral time-resolved single pixel camera, shown in figure 2.6, which was experimentally tested by studying the propagation of a laser pulse in fluorescent solutions. The fluorophores presented different emission spectra and lifetimes, which was visible in the both spectral and temporal recovered images, proofing the efficiency of the scheme. Rousset *et. al* described an SPC system which did not use the conventional compressive sensing approach, but an adaptive acquisition strategy, referring as Adaptive Basis Scan by Wavelet Prediction (ABS-WP). The ABS-WP's goal is to find and acquire the more significant wavelet coefficients [67]. The discrete wavelet decomposition applied to a N resolution image produces N^2 wavelet coefficients, allowing a multiresolution analysis at different scales - $1 \leq j \leq J$, with $1 \leq J \leq \log_2(N)$ [68]. Part of these coefficients correspond to an approximation image (image at J scale), while others are detailed coefficients (j). The most significant coefficients are predicted and localized by performing an interpolation followed by a 1-level wavelet transform and a non-linear approximation, in which the percentage of the greatest coefficient is saved and localized, [68].

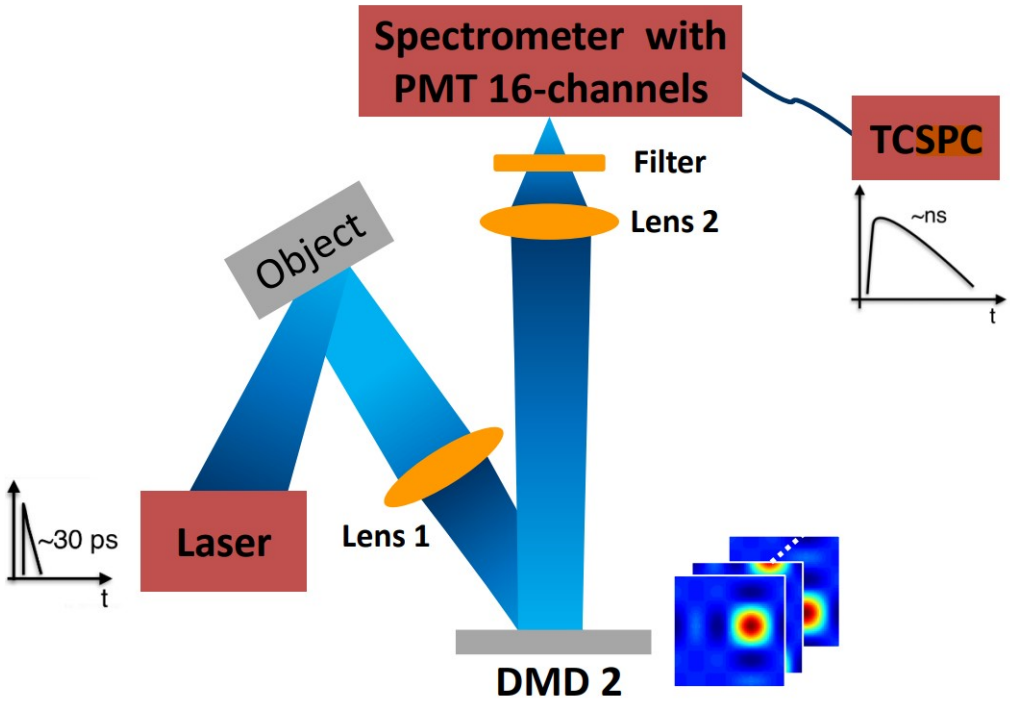

Figure 2.6: Experimental setup of a multispectral time-resolved single pixel camera developed by Rousset *et.al* [66]. Extracted from [66].

Hyperspectral imaging (HSI) is an imaging technique capable of acquiring wavelengths on an extended region of the electromagnetic spectrum, ranging from UV light to near or short-wave infrared. Comparing to MSI, HSI performs a continuous wavelength acquisition, while MSI provides the information on pre-selected wavebands [63]. Peller *et.al.* [2] proposed an hyperspectral system, using an SPI scheme based on CS, with the goal of discriminating thermally damaged from healthy tissue of *ex-vivo* porcine samples. To do so, Peller used reflectance and fluorescence emission spectroscopy. Both spectra show the damaged regions, proving the HSI system to distinguish the tissues.

2.5.2 Phosphorescence Imaging

Phosphorescence Lifetime Imaging

Phosphorescence Lifetime Imaging is an emerging imaging technique that provides functional images, similarly to FLI [1]. While fluorescence lifetime show reduced values, since the decay between the electronic states occurs almost instantly after the removal of the excitation source, phosphorescence lifetime present higher values. To obtain a more comprehensive knowledge, simultaneous fluorescence and phosphorescence can be performed, as it happens in some works [69, 70]. However, these studies do not use SPI schemes.

Zang *et al.* [71] studied several phosphorescent probes for different applications. The most advanced and explored application of PLI is the oxygen monitoring and imaging O_2 distribution in biological samples [1]. The two main properties of O_2 phosphorescent probes, which make them suitable for PLI are:

1. Both ground state of O_2 and excited state of the phosphorescent probe are triplets, meaning that when the probe is on its ground state the O_2 is on an excited state and vice versa;

2. Designing probes presenting a strong response to oxygen concentration, while showing a minimal dependence on other environmental variables, such as pH, or temperature, etc, is a relatively simple task.

Thus, some studies have been developed to monitor O_2 by taking advantage of the strong phosphorescence quenching. Figure 2.7 shows the signal processing scheme to obtain phosphorescence lifetime images. In this thesis, it was proposed a SPI application using CS principles to simultaneously obtain phosphorescence intensity and lifetime maps, enabling

O_2 motorization. In the following chapter (Chapter 3) the methods used to achieve this purpose are described.

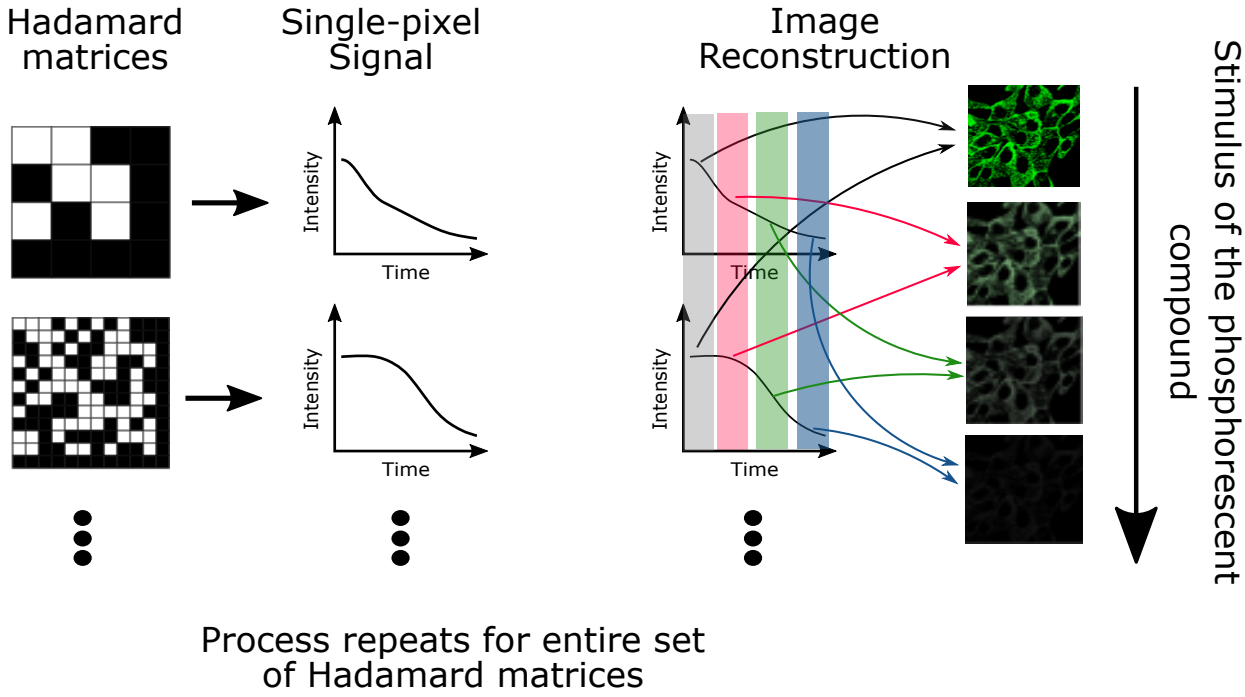

Figure 2.7: Signal processing overview.

3 Methods

A single pixel camera based on structured illumination was developed to simultaneously obtain phosphorescence lifetime and intensity images. The designed SPC was composed by three main devices, a Digital Light Processing Device (DLP) to produce the patterns to stimulate the samples to be imaged, a photodiode to capture the light coming from the scene and a Digital Acquisition System (DAS) to digitize the measurements. These measurements were used by the reconstruction algorithm TVAL3 to reconstruct the images of the scene. The scene was composed by two cells containing a solution with an oxygen sensitive biomarker, the Pt(II) ring-fused chlorins, whose phosphorescence is strongly quenched in presence of oxygen [5].

The methods chapter is divided into two parts. The first one describes the developed SPC setup and its efficiency in producing phosphorescence intensity and lifetime images, using the compressive sensing concepts. In the second part, the experimental scheme was used to image low volume solutions containing different concentrations of the O_2 biomarkers, using lower compression ratios and study a lifetime dependency over the ventilation time.

3.1 Experimental Setup

The experimental setup was composed by a digital light processing device (DLP LightCrafter ^{TM} 4500 - Texas Instruments [72]), containing a DMD and 3 LEDs - Red, Green and Blue. The DLP displayed the patterns, which were determined by the sensing matrix (Φ). Each row of the sensing matrix was reshaped into a 128×128 2D pattern. These rows correspond to Walsh functions selected from an Hadamard matrix with order equals to 14. In order to take full advantage of the DLP projection area, this pattern was expanded to a digital image of 512×1024 pixels. Due to the arrangement of the DLP mirrors, this image is projected as a square pattern.

The DMD only reads 0 and 1, corresponding to the state OFF and ON, *i.e.*, to the micromirrors positions of $-12°$ and $+12°$. Two projections by each sensing matrix row (positive

and negative) were performed, improving the signal-to-noise ratio (SNR) [73]. Therefore, the final coefficient value, of a specific pattern and time, corresponded to the difference between the photodiode measurement of a positive y_+, and a negative pattern, y_-:

$$y_p = y_+ - y_- \tag{3.1}$$

The DLP used the green and blue LEDs to illuminate the samples in the range between 428 and 620 nm. The samples were placed in front of the DLP; however, since its optical system was incapable of focusing on short distances, a +40mm lens was positioned outside the DLP. The light coming from the samples reached the photodetector (Thorlabs APD410A/M [74]), which was coupled to a band pass filter with central wavelength of 769 nm and band width of 41 nm (Edmund optics 84105 [75]) and to a +20 mm lens to improve light collection. The photodiode measurements were digitized by a DAS. The control software was written in Python 3.6 using the nidaqmx module and an extender version of pycrafter4500 and dlpc350 modules [76]. The working scheme of the single pixel camera is presented in figure 3.2.

(a) DLP

(b) Photodetector

(c) DAS 1

(d) DAS 2

Figure 3.1: Experimental setup components. (1) Digital Light Processing device, (2) avalanche photodetector, (3) *National Intruments* DAQ X USB-6361 [77] and (4) Analog Discovery 2 - Digilent [78].

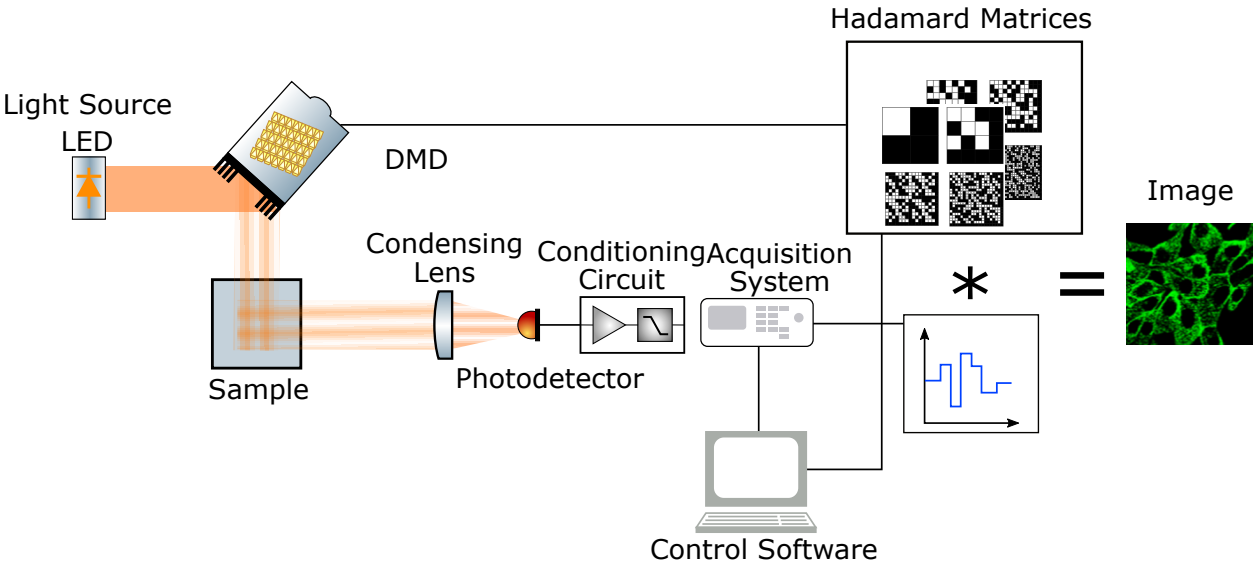

Figure 3.2: Simplified scheme of the single pixel camera.

3.2 Pt(II) Ring-Fused Chlorins

Platinum(II) 4,5,6,7-tetrahydropyrazolo[1,5-a]pyridine–fused chlorins are near-infrared (NIR) luminescent compounds, presenting simultaneous phosphorescence and fluorescence emission at room temperature, in the biological spectral window of $700 - 850$ nm. In the presence of O_2, these luminescent compounds phosphorescence is strongly quenched, while fluorescence is not affected, making them valuable to be used as oxygen sensors, in biological media.

Pt(II) ring-fused chlorins are composed by three main compounds: chlorins, ring-fused, *i.e.*, 4,5,6,7-tetrahydropyrazolo[1,5-a]pyridine and platinum. Chlorins show great spectral properties in NIR region, but present poor chemical stability. However, by adding a ring-fused, the 4,5,6,7-tetrahydropyrazolo[1,5-a]pyridine-fused, to the chlorins, the stability improves significantly. Platinum is an high atomic number metal ion, which enhances the triplet state formation, potentiating phosphorescence within the biological relevant spectral interval. Figure 3.3 shows the chemical structure of the Pt(II) ring-fused chlorins in this work and figure 3.4 shows the absorption spectra, peaking at 400 nm and the emission spectra, reaching its maximum at 756 nm.

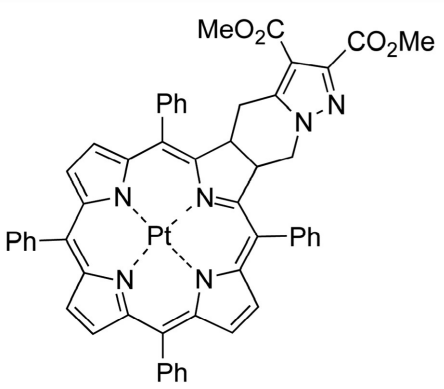

Figure 3.3: Chemical structure of the Pt(II) ring-fused chlorins. Adapted from [5]

.

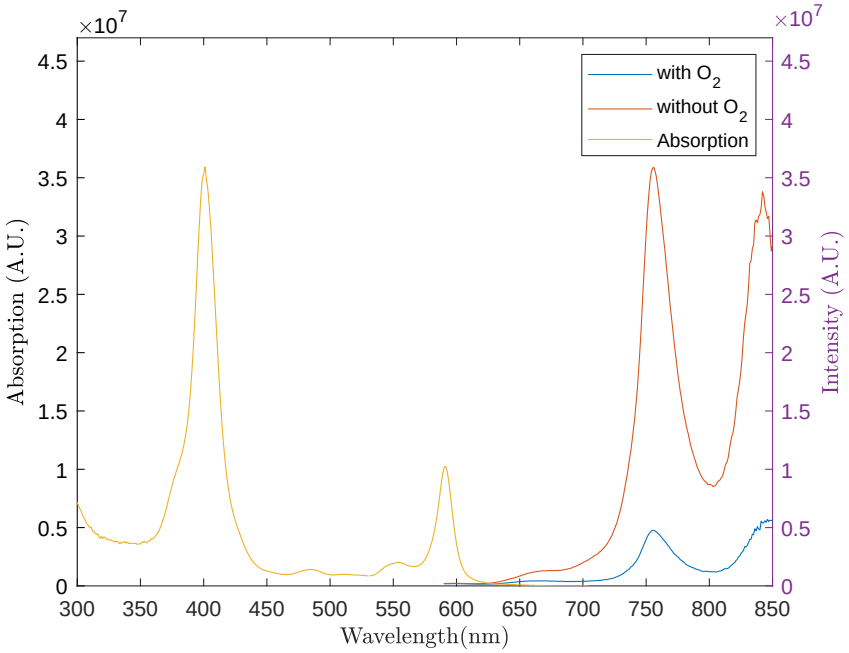

Figure 3.4: Absorption and emission Spectra of Pt(II) chlorins in the presence and absence of O_2.

3.3 Signal Processing

The sampling frequency (f_s), the exposure time (t_{exp}), the number of points acquired *per* projected pattern (P) and the compression ratio (CR) are variable acquisition parameters that affect the images reconstruction. After data collection, the set of final coefficients (y_p) were rearranged in a $P \times X$ 2D matrix, being X the number of projected patterns. So, each column corresponded to the P acquired points of a single pattern. To normalize the data, the mean value of each pattern, $\overline{y}_p$, *i.e.*, each column, was subtracted to each pattern's value y_p (with $p \in [1, P]$):

$$y_f = y_p - \frac{\sum_{p=1}^{P} y_p}{P} = y_p - \overline{y_p} \tag{3.2}$$

These coefficients were the input of the TVAL3 reconstruction algorithm, which reconstructed a stack of P images with a time interval between each other of $1/f_s$. The recovered images presented a 128×128 resolution and were reconstructed with different compression ratios. In the proof-of-concept, 25%, 10%, 5% and 1% compression ratios were studied, implying a maximum acquisition number of 4096 sampling coefficients ($\frac{1}{4} \times (128 \times 128)$). In the pilot study, only 10% and 5% compression ratios were studied, which enabled to reduce the acquisition number of coefficients to 1638, and so, reduce the acquisition time.

After the reconstruction of the stack of images, the phosphorescence intensity and lifetime maps were obtained using a pixel-by-pixel approach. The recovered images were first reshaped to half of their resolution (64×64) and then used to obtain the phosphorescence maps. Each pixel was selected in all P images and their mean value were used to obtain the phosphorescence intensity map. The phosphorescence lifetime map was obtained using a similar strategy. However, instead of calculating the mean, each pixel was fitted into an exponential decay, which was applied employing the MATLAB function `fit()`:

$$I(t) = I_0 e^{-\frac{1}{\tau}t} + c \tag{3.3}$$

being I_0 is the maximum intensity, τ is lifetime value and c is the value to which the curve tends to.

In both phosphorescence intensity and lifetime maps, two regions of interest (ROI), corresponding to the two solution of the scene, were defined. The mean and standard deviation values of the intensity and lifetime maps were obtained for each ROI.

3.4 Proof-of-concept

In the proof-of-concept, the goal was to prove the SPC scheme efficiency of determining the phosphorescence intensity and lifetime maps of the O_2 biomarker and reconstruct a stack of images with high sampling frequency. To do so, the same volume of a toluene solution, containing a $10^{-6}M$ concentration of Pt(II) ring-fused chlorins, was placed into two distinct quartz cells. One of the cells was customized to enable nitrogen gas ventilation to deoxygenate the solution. The sample was ventilated during 30 minutes. The other solution was not ventilated, and so, it contained a constant amount of oxygen related with atmospheric oxygen concentration. The O_2 biomarker phosphorescence is strongly quenched in the presence of oxygen, leading to lower intensity and lifetime values, which enabled to study and distinguish the two solutions in both phosphorescence intensity and lifetime maps.

Figure 3.5 shows the experimental setup, with both samples placed on the 3D printed support, with interchangeable positions. The cells were placed and imaged on both right and left positions of the holder. In this scheme, the DAS employed was the *National Instruments* DAQ X USB-6361.

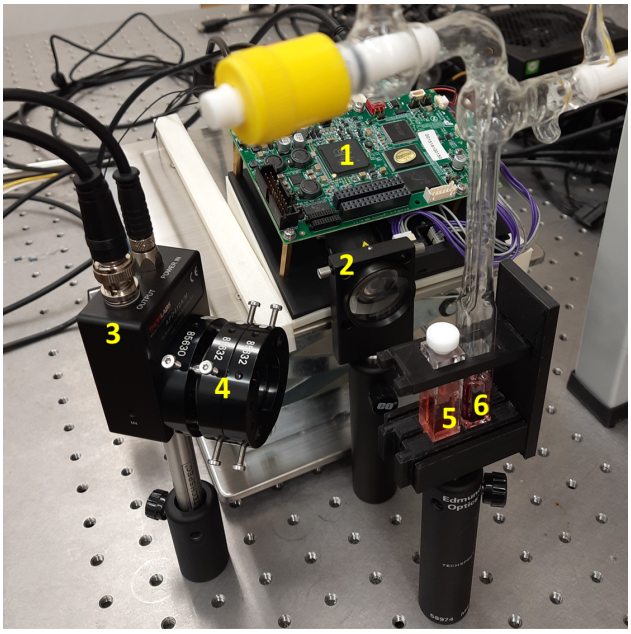

(a) Lateral view

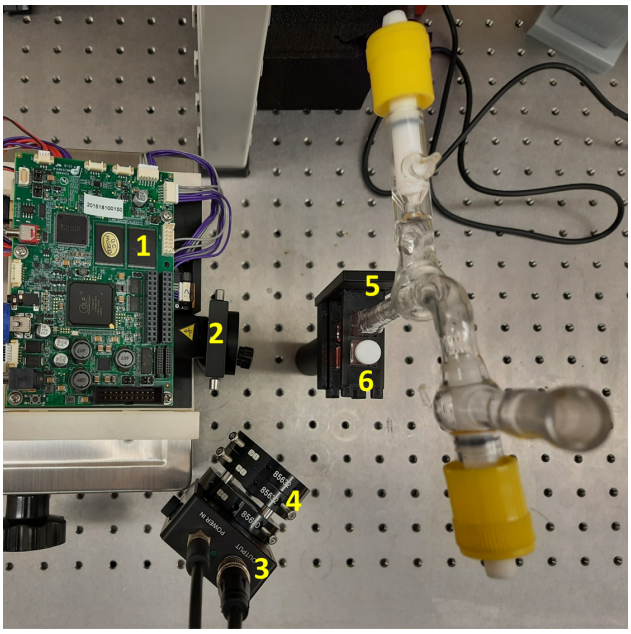

(b) Top view

Figure 3.5: Experimental Setup. (1) Digital Light Processing device, (2) a focusing lens (f=+40 mm), (3) avalanche photodetector (4) band pass optical filter and a focusing lens (f=+20 mm), (5) oxygenated sample and (6) deoxygenated sample.

The DLP projected the Hadamard Walsh ordering patterns using the green and blue LEDs. The acquisitions were performed with half of the photodiode's gain and according to the following parameters:

- $f_s = 2$ MHz;

- $t_{exp} = 20$ ms;
- $P = 250$ points;
- $CR = [25\%, 10\%, 5\%, 1\%]$

Therefore, TVAL3 reconstructed 250 images. However, due to an experimental limitation of a time delay between the end of the light pattern and the LED quench, the first 7 images were removed from the list of 250 images. Moreover, the last images were also excluded, since they only presented background noise. Overall, 200 images, over a 100 ms period, were used to obtain the phosphorescence intensity and lifetime maps.

3.5 Pilot Study

After studying the SPC scheme efficiency in obtaining the samples phosphorescence maps, the goals, in this section, were to study samples with different concentrations of Pt(II) ring-fused chlorins, study a lifetime dependency over the ventilation time, reduce the compression ratio and reduce the solution's volume. To do so, an experimental setup similar to the proof-of-concept one was used. In this setup, the DAS employed was the Analog Discovery 2 - Digilent, since it reaches 10 MHz, while the other one tops at 2 MHz. Even though in this study the sampling frequency is 20 kHz, in the future may be useful to perform acquisitions with higher sampling frequency. Moreover, the photodiode was placed in a lateral position, enhancing the light collection of both cells. Figure 3.6 shows the SPC scheme with the 3D printed support and two cells. The cells used, in this section, had a 3 ml capacity, enabling to accomplish the goal of reducing the sample's volume. They presented two terminations, one connected to the gas nitrogen cylinder and the other to a three way stopcock, allowing the oxygen removal. The plastic tube connecting the cell with the cylinder had a flux regulator, enabling to control the flux reaching the solution, which is most advantageous when both cells were being simultaneous ventilated to assure an equal flux (figure 3.7). These cells presented a light opaque wall, which were positioned to face the wall of the 3D printed support.

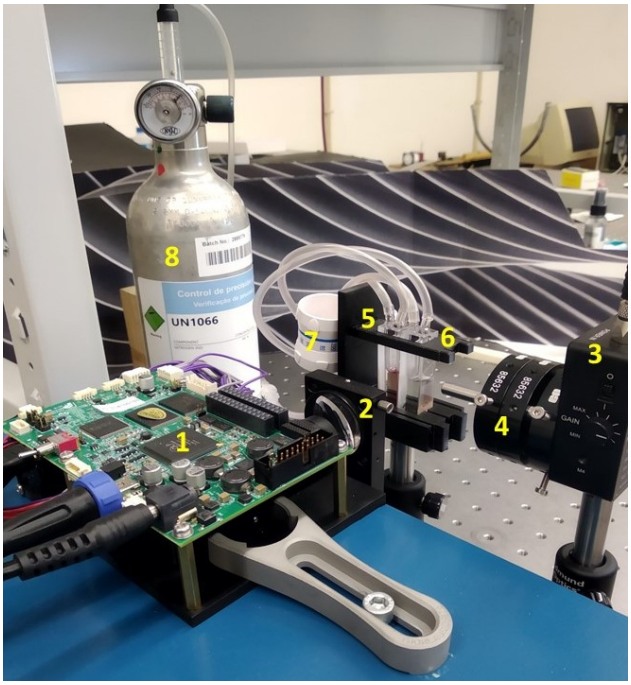

(a) Lateral view

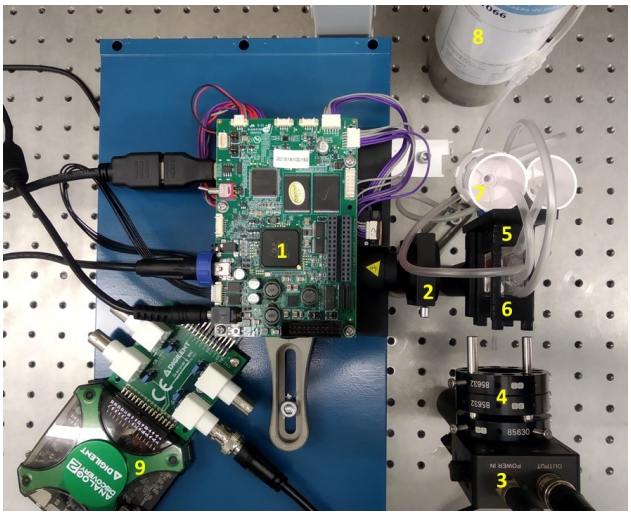

(b) Top view

Figure 3.6: Experimental Setup. (1) Digital Light Processing device, (2) a focusing lens (f=+40 mm), (3) avalanche photodetector (4) band pass optical filter and a focusing lens (f=+20 mm), (5) and (6) flow cells (7) flux regulator (8) nitrogen gas cylinder (9) DAS.

Figure 3.7: Flow cell containing the D1 solution, showing the two terminations, one connected to the gas nitrogen cylinder through a flow regulator and the other to a three way stopcock.

Three solutions containing different concentrations of Pt(II) ring-fused chlorins were studied. One contained a relative high concentration (D1), other a low one (D3) and a third an intermediate concentration (D2). The solvent of these solutions were dimethylsulfoxide (DMSO), which comparing to the toluene is a less volatile and more biocompatible compound [79]. Each cell contained a solution's volume of 1.5 ml.

To study lifetime dependency over the ventilation time, a sequential GN_2 ventilation strategy was used. The solutions were first ventilated with air, using a syringe pump [80], with a flow rate of 2.58 ml/min, during 15 min. Then, the cells were imaged with different ventilation times, starting with no ventilation (0 seconds), followed by a 30 seconds ventilation time, which was repeated five times. Therefore, the solutions were sequentially imaged with 0, 30, 60, 90, 120 and 150 ventilation times. The ventilation time of 30 seconds was chosen by a trial and error approach. The data collected in the trials suggested that for higher values, the intensity and lifetime maps would not show any differences between each ventilation, while shorten periods of time were impractical to achieve a constant ventilation flux.

The sequential GN_2 ventilation strategy was applied in three distinct scenarios, one in which the left sided sample on the support was ventilated, other with the right sided cell ventilated and a third where both cells were ventilated. Thus, an overall of 18 different scenarios were studied by combining these 3 scenarios with 6 ventilation times.

The acquisitions were performed with the number of points collected *per* pattern of 256

points, $P = 256$. The first 64 points were in-projection (pre-trigger), while the other 192 points were post-trigger. The pre-trigger points were used to obtain the phosphorescence intensity maps, since by collecting the points from a stable light emission, the maps were less noisy. The phosphorescence lifetime maps were obtained by using the post-trigger points. However, the first 3 points presented a constant behaviour, and so, they were removed from the analysis. Overall, TVAL3 reconstructed a stack of 64 images, corresponding to a period time of 3.2 ms and 189 over a time period of 94.5 ms.

Both Walsh and Block Hadamard orderings were studied [19] and projected using the blue and green LEDs. The acquisitions were performed with:

- $f_s = 2$ MHz;
- $t_{exp} = 20$ ms;
- $P = 256$ points, with 64 pre-trigger and 192 post-trigger;
- $CR = [10\%, 5\%]$

4 Results and Discussion

The results are presented in two sections, according the two experiments detailed in the methods chapter, the Proof-of-concept and the Pilot Study.

4.1 Proof-of-concept

In the proof-of-concept, the SPC was used to image two distinct samples, one in absence of oxygen and other with dissolved oxygen. The photodetector collected the light coming from the scene and produced an electrical signal. Due to the DMD limitation of only reading 0 and 1, positive and negative patterns were projected, generating two electrical signals. These electrical signals are a sequence of exponential decay curves, each one corresponding to the phosphorescent behaviour of the Pt(II) ring-fused Chlorins after being illuminated by a single pattern.

Figure 4.1 shows the electrical signals of 6 patterns for both positive and negative measurements and the difference between them. Figure 4.1 (a), (b) present the positive and negative patterns measurements with the deoxygenated sample positioned on the left side of the holder and the oxygenated on the right side, whereas (d), (e) show the signals for the inverse sample's positions (oxygenated on the right side and deoxygenated on the left). The final electrical signals, resulting from the difference between the positive and negative pattern's measurements, are shown in (c) and (f). Figure 4.2 shows a final electrical signal with 50 patterns. The peaks maximum amplitude decrease over the projected patterns, which is in agreement with the Hadamard Walsh ordering, proving that the last coefficients can be removed without affecting the image reconstruction.

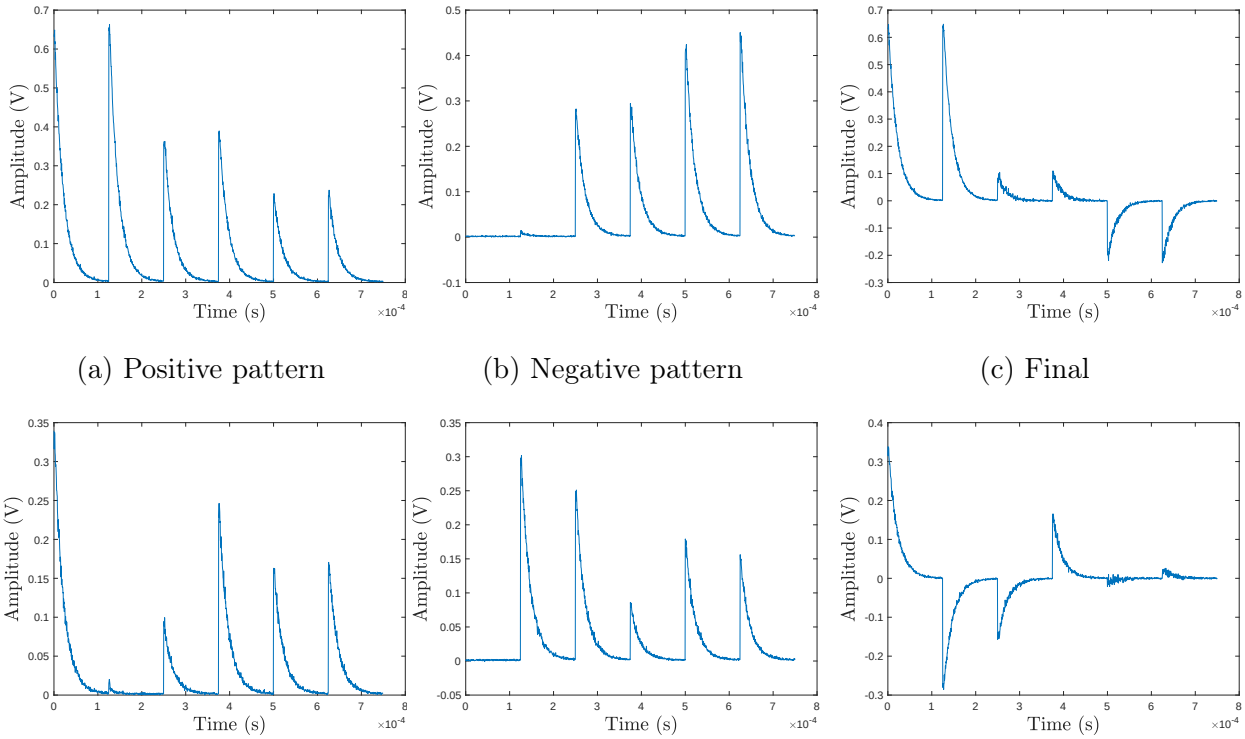

(a) Positive pattern (b) Negative pattern (c) Final

(d) Positive pattern (e) Negative pattern (f) Final

Figure 4.1: Electrical signals of the photodetector's collected light, showing 6 patterns. (a) and (d) show the electrical signal resulting from the light acquisition of the positive patterns, while (b) and (e) resulted from the negative patterns. (c) and (f) are the difference between the measurements of the positive and the negative pattern, providing the final coefficients. The deoxygenated sample was positioned on the left side of the holder at (a), (b) and (c), and on the right at (d), (e) and (f).

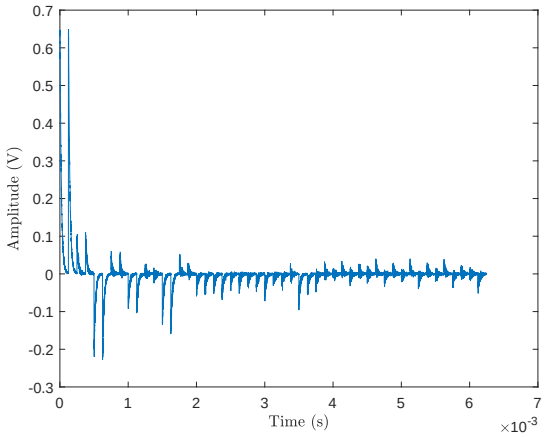

Figure 4.2: Electrical signal resulting from the difference of positive and negative patterns measurements, with the deoxygenated sample on the left side of the holder and the oxygenated one on the right.

A stack of 128×128 resolution images was reconstructed by TVAL3, with a time interval between each other of 500 ns. Figures 4.3 and 4.4 present the reconstructed images with a time delay after the stimulus termination of 0 ms, 11.5 ms and 21.5 ms, for 25% and 1% compression ratios. The black rectangles were manually segmented and correspond to the ROI of the two samples positions. In both figures the ventilated sample was clearly identified. However, the cell containing O_2 was indistinguishable from the background noise, since the intensity values were below this noise.

By comparing the two figures, 4.3 and 4.4, it was clear that the intensity of the signal depends on the sample position on the holder. When the sample is positioned on the right side, it only appears in a fraction of the ROI, which does not occur when it is on the left location. The reasons behind this imbalance intensity is the narrow field of view limited by the lens on the photodetector and the alignment procedure, which led to more light collection on the left side. Moreover, on the right edge of the reconstructed images, there is an artifact, which is reduced over time and may be related to the reconstruction parameters to the imbalance of the scene.

Figures 4.3 and 4.4 also show, within each compression ratio, a decrease in the pixel values, as the time after stimulus increases. This intensity decay was studied by obtaining the ROI's mean value for each image and fitting the values to an exponential decay curve presented at 3.3, using the MATLAB function `fit()`.

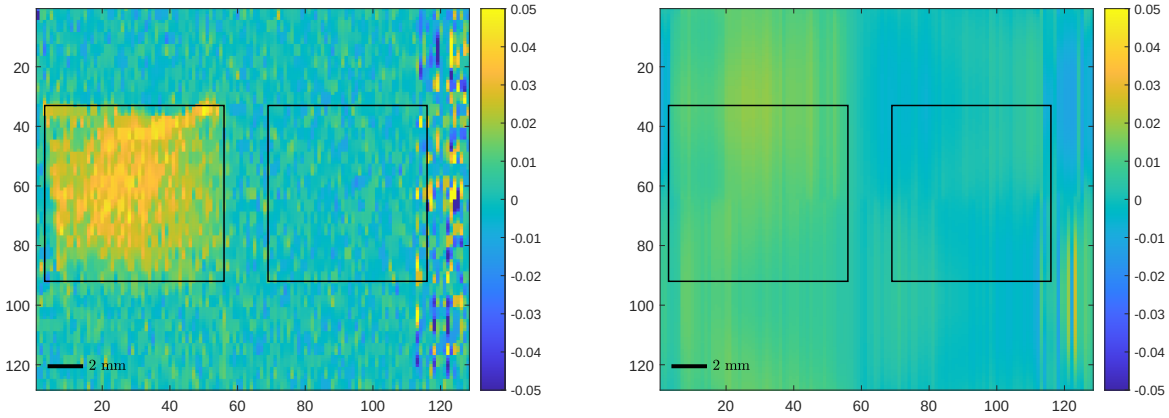

(a) CR = 25%

(b) CR = 1%

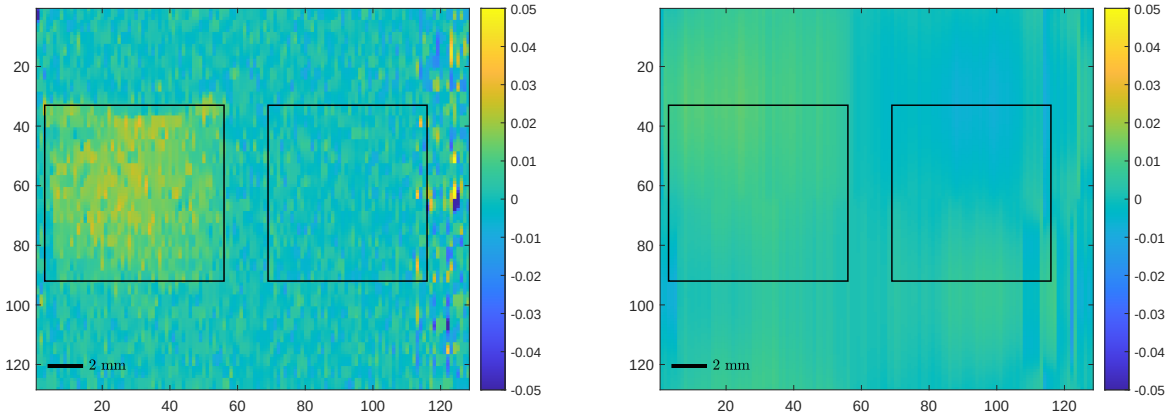

(c) CR = 25%

(d) CR = 1%

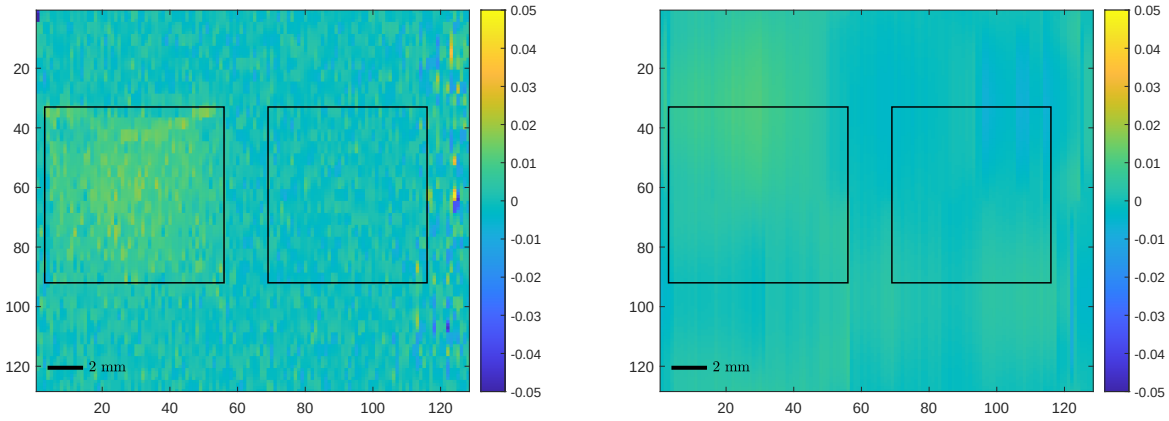

(e) CR = 25%

(f) CR = 1%

Figure 4.3: Reconstructed images with the deoxygenated sample on the left side of the holder and compression ratios of 25% and 1%. (a), (b) correspond to images with a time after stimulus of 0 ms, (c), (d) 11.5 ms and (e), (f) 21.5 ms.

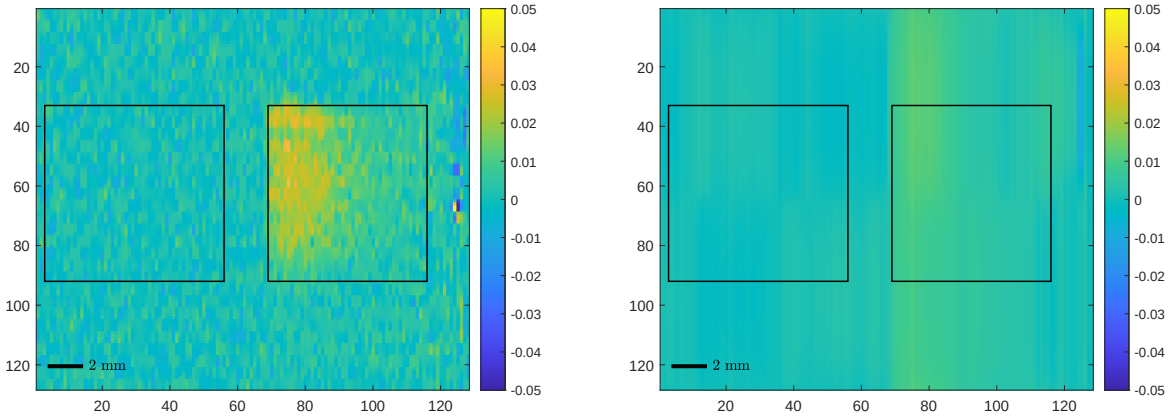

(a) CR = 25%

(b) CR = 1%

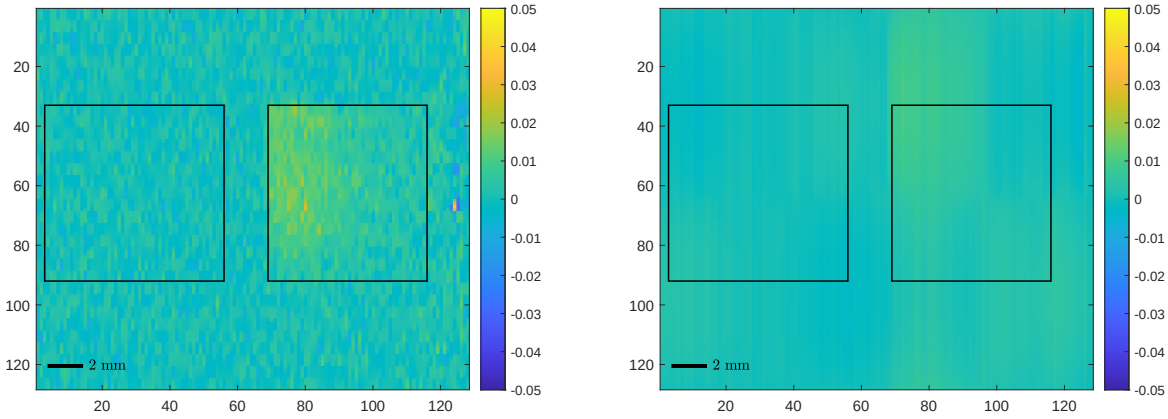

(c) CR = 25%

(d) CR = 1%

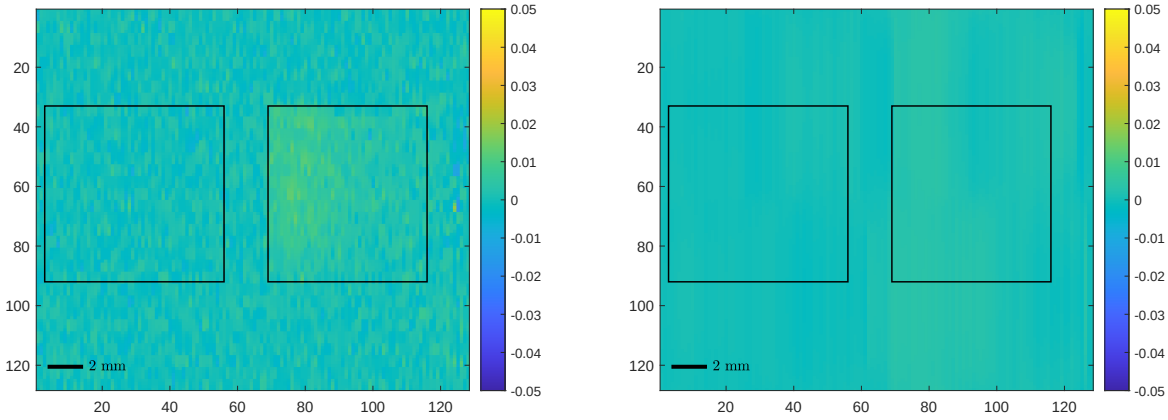

(e) CR = 25%

(f) CR = 1%

Figure 4.4: Reconstructed images with the deoxygenated sample on the right side of the holder and compression ratios of 25% and 1%. (a), (b) correspond to images with a time after stimulus of 0 ms, (c), (d) 11.5 ms and (e), (f) 21.5 ms.

Figure 4.5 shows the phosphorescence intensity decay for 25%, 1% CRs and with the sample on both positions. The yellow colored curves represent the left ROI and the blue the right one. Regardless of the samples positions on the holder or the compression ratios, the curves corresponding to the deoxygenated sample present an exponential decay, tending to 0, while the oxygenated ones remain constant, around 0. The maximum intensity value for the deoxygenated sample, when placed on the left side of the holder, was 25×10^{-3} AU and, when on the right side was 14×10^{-3} AU. Even though there is an intensity imbalance, depending on the deoxygenated sample position on the holder, the exponential behaviour was verified in both cases, proving that phosphorescence lifetime is a more robust measurement than intensity.

The phosphorescence lifetime values obtained from the curves for the four compression ratios in study, 25%, 10%, 5% and 1%, are presented in the Table 4.1. The lifetime values of the deoxygenated cell were approximately 20 μs, as for the oxygenated were around 11 μs.

Phosphorescence intensity and lifetime maps for 25% and 1% are shown in figures 4.6 and 4.7. The intensity maps show, as expected, similar information to the reconstructed images. The deoxygenated sample in the lifetime maps, comparing to the intensity ones, present an uniform region of lifetime in all the ROIs area. The phosphorescence lifetime maps present some noise, showing low SNR, since lifetime was calculated for each pixel of the image.

As CR decreases, it was verified a pixel stretching phenomenon, in which the pixels seemed to extend their area, leading to a wider image representation of the deoxygenated sample. This was evident in the 1% lifetime and intensity maps. However, the 25%, 10% and 5% maps presented a good homogeneity and delimitation of the sample's boundaries, proving to be suitable for imaging the phosphorescent compound.

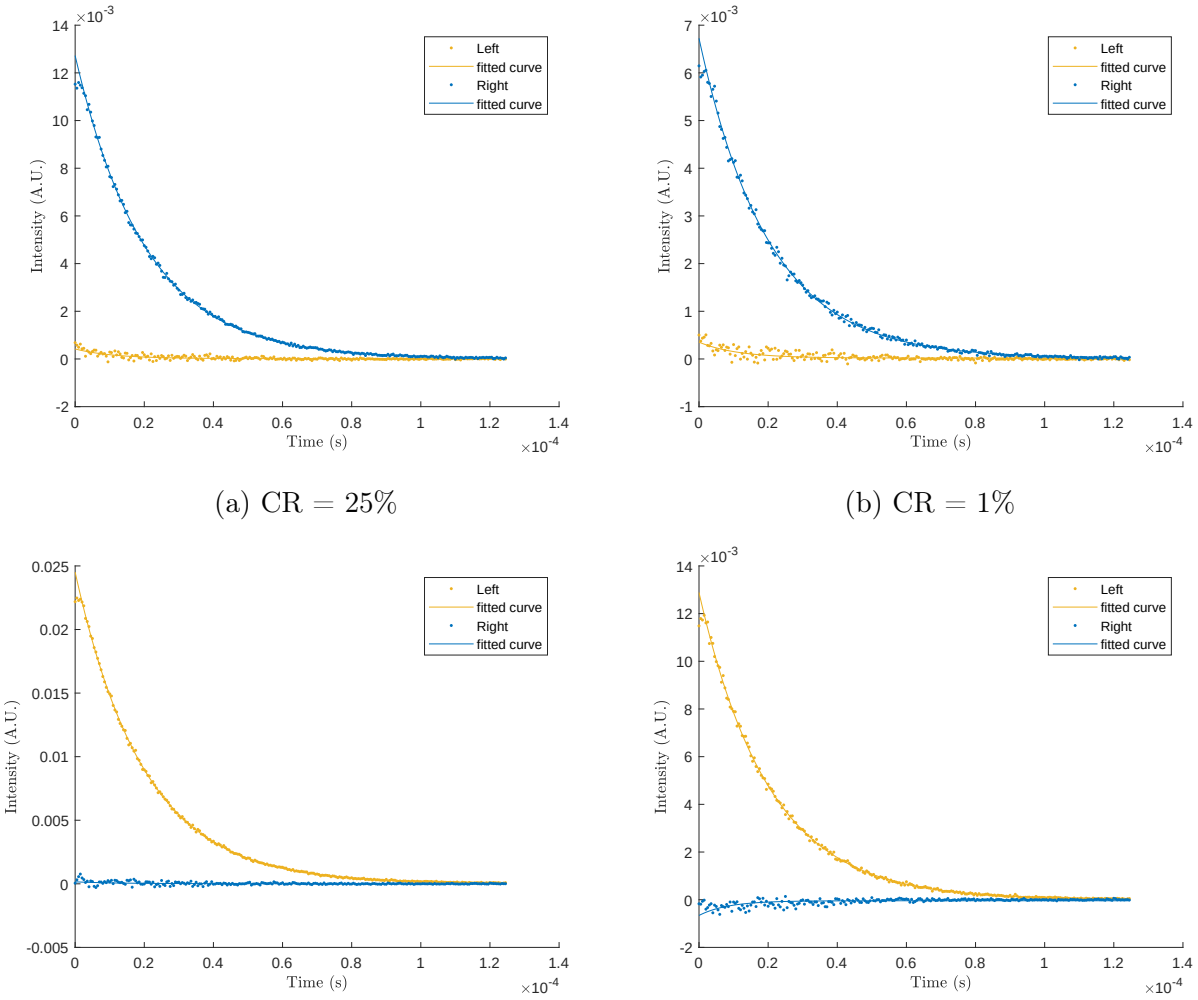

(a) CR = 25%

(b) CR = 1%

(c) CR = 25%

(d) CR = 1%

Figure 4.5: Phosphorescence lifetime curves of the right (blue curve) and left segments (yellow curve), for compression ratios of 25% and 1%. In the first row, the deoxygenated sample is positioned on the right side of the holder, while on the second one, it is placed on the left side.

.

Table 4.1: Lifetime values (s) obtained from the curves of the figure 4.5 for the four compression ratios, 25%, 10%, 5% and 1%.

Samples	Curves	25%	10%	5%	1%
Oxygenated	yellow	1.11×10^{-5}	1.11×10^{-5}	1.11×10^{-5}	1.11×10^{-5}
Deoxygenated	blue	2.03×10^{-5}	2.03×10^{-5}	2.04×10^{-5}	2.01×10^{-5}
Deoxygenated	yellow	1.99×10^{-5}	1.99×10^{-5}	1.99×10^{-5}	2.03×10^{-5}
Oxygenated	blue	1.26×10^{-5}	1.26×10^{-5}	1.28×10^{-5}	8.30×10^{-6}

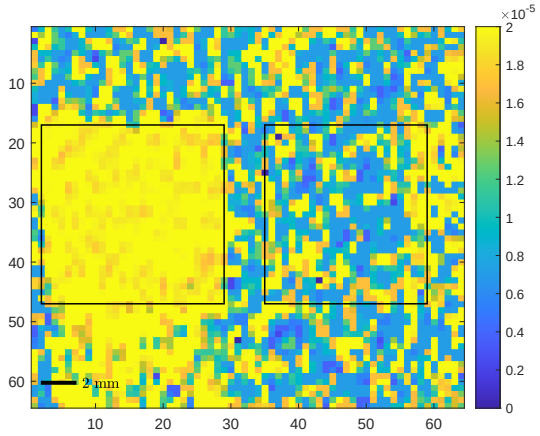

(a) CR = 25%

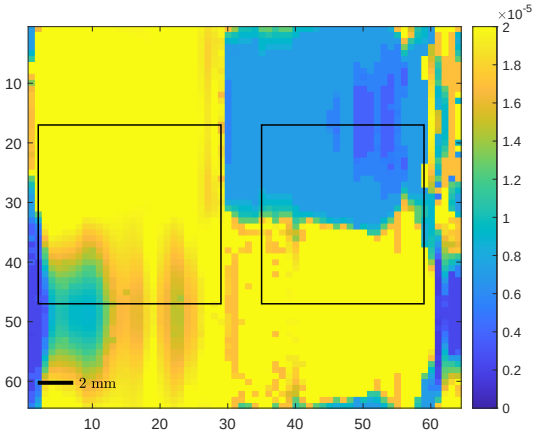

(b) CR = 1%

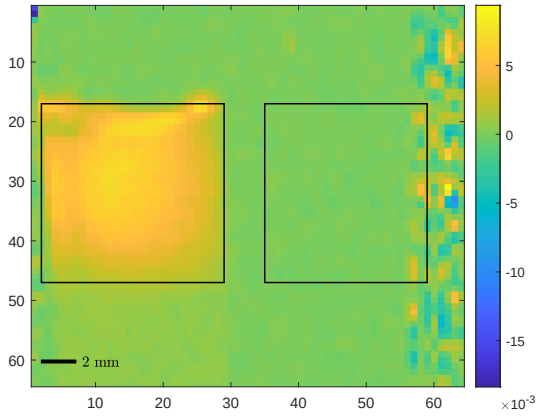

(c) CR = 25%

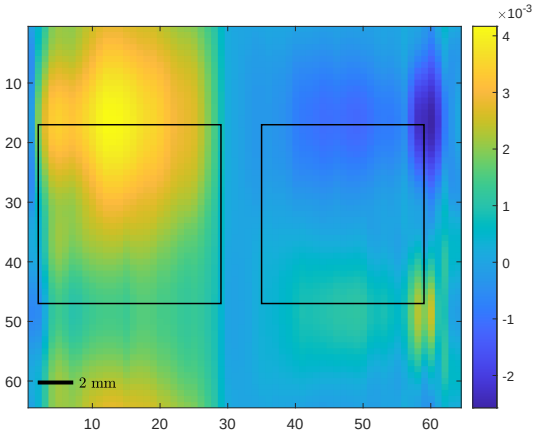

(d) CR = 1%

Figure 4.6: Phosphorescence lifetime and intensity maps of the samples, with the deoxygenated solution on the left side of the holder and compression ratios of 25% and 1%. Images (a), (b) are lifetime maps and (c), (d) are intensity maps.

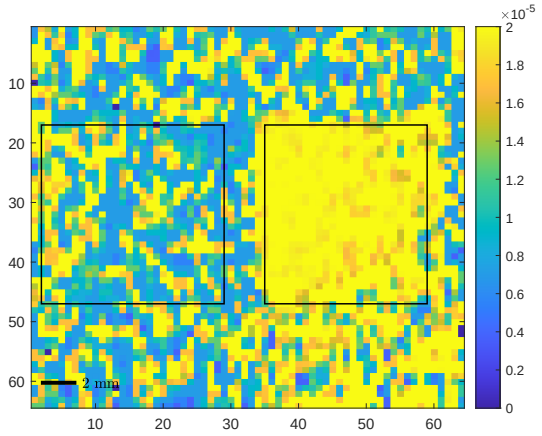

(a) CR = 25%

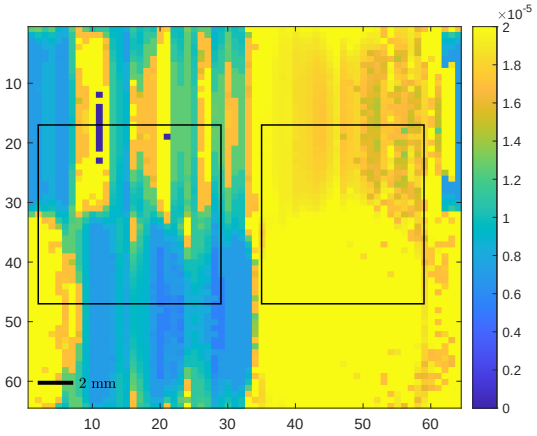

(b) CR = 1%

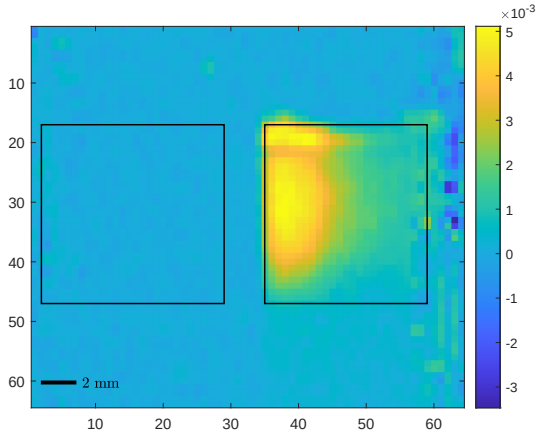

(c) CR = 25%

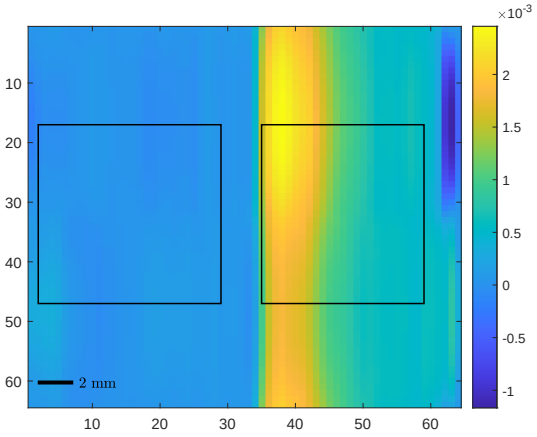

(d) CR = 1%

Figure 4.7: Phosphorescence lifetime and intensity maps of the samples, with the deoxygenated solution on the right side of the holder and compression ratios of 25% and 1%. Images (a), (b) are lifetime maps and (c), (d) are intensity maps.

Table 4.2: Mean phosphorescence lifetime and intensity values and their corresponding standard deviations for each position of the samples and for 25%, 10%, 5% and 1% compression ratios.

Positions	Sample	CR	$\overline{\tau}(\mu s)$	$\sigma_{\overline{\tau}}(\mu s)$	$\overline{I}$	σ_I
Left	Oxygenated	25%	14.9	75.9	4.88×10^{-5}	1.2×10^{-4}
		10%	22.5	127	4.89×10^{-5}	8.97×10^{-5}
		5%	20.6	77	4.87×10^{-5}	8.10×10^{-5}
		1%	1.1	183	-6.63×10^{-5}	8.10×10^{-5}
Right	Deoxygenated	25%	20.5	5	2.14×10^{-3}	1.42×10^{-3}
		10%	20.4	4	2.14×10^{-3}	1.40×10^{-3}
		5%	20.1	2	2.13×10^{-3}	1.40×10^{-3}
		1%	20.1	2.88	1.26×10^{-5}	8.3×10^{-6}
Left	Deoxygenated	25%	20.0	3.5	4.02×10^{-3}	1.83×10^{-3}
		10%	19.9	1.9	4.02×10^{-3}	1.73×10^{-3}
		5%	19.8	1.7	4.02×10^{-3}	1.68×10^{-3}
		1%	19.6	4.9	2.17×10^{-3}	9.0×10^{-4}
Right	Oxygenated	25%	17.6	334	5.05×10^{-5}	5.9×10^{-4}
		10%	-42.7	1751	4.73×10^{-5}	4.9×10^{-4}
		5%	16.3	42	4.89×10^{-5}	4.4×10^{-4}
		1%	3.86	107	-6.63×10^{-5}	6.6×10^{-4}

The mean value and the standard deviation of the pixels values within the ROIs of the intensity and lifetime maps were calculated. Table 4.2 summarizes the results of both intensity and lifetime maps. The intensity values of the deoxygenated sample strongly depended on its position on the holder, as expected. When it is on the left side of the holder, the mean intensity value is around 4.00×10^{-3} AU while on the right side, is approximately 2.00×10^{-3} AU, showing that the mean intensity double from the right to the left positions. This relationship was not verified in the 1% sampling ratio, presenting the same intensity values.

Comparing the mean values of the two samples, the deoxygenated shows intensity values two orders higher than the oxygenated one. This was also expected, since the oxygenated was not visible on the reconstructed images nor on the maps.

The mean lifetime values of the deoxygenated sample were consistent for all the com-

pression ratios, ranging from 19.6 to 20.5 μs. Regarding the standard deviation, the interval is $1.7 - 5$ μs, where 1.7 μs was achieved in a 5% map and the 5 μs in a 25% one, suggesting that using lower CRs do not mean less precision. In addiction, the standard deviation values of the right ROIs are higher than the left, which can be justified by the intensity imbalance. However, the standard deviation values are still an order lower than the mean, which does not compromise the conclusion that phosphorescence lifetime is a robust measurement, that does not depend on the sample's position.

Regarding the mean lifetime values of the oxygenated sample, they are not consistent and did not show any relationship or tendency, since the values ranged from -42.7 to 22.5 μs. The standard deviations were much higher than the mean, varying from 42 to 1751 μs.

The results obtained for the 1% compression ratio were the ones that provided less useful information. Therefore, in the pilot study approach, 1% was excluded from the study. Moreover, since 10% and 5% sampling ratios presented good results and in agreement with the 25%, only these two CRs were studied, in the following experiment.

4.2 Pilot Study

In this section, a sequential gas nitrogen ventilation strategy was used to study a relationshipship between phosphorescence lifetime and GN_2 ventilation time. To do so, both Hadamard Walsh and Block orderings were projected. Figure 4.8 shows the electrical signals of 6 patterns of both orderings, with (a), (d) showing the positive measurements, (b), (e) the negative and (c), (f) the difference between them. The first row of figure 4.8 shows the coefficients of the Walsh ordering, while the second presents the Block one, for D1 and D3 solutions placed on the left and right side of the holder, respectively, both non GN_2 ventilated. Each pattern of the signal shows a constant part, corresponding to the pre-trigger and the exponential decay to the post-trigger.

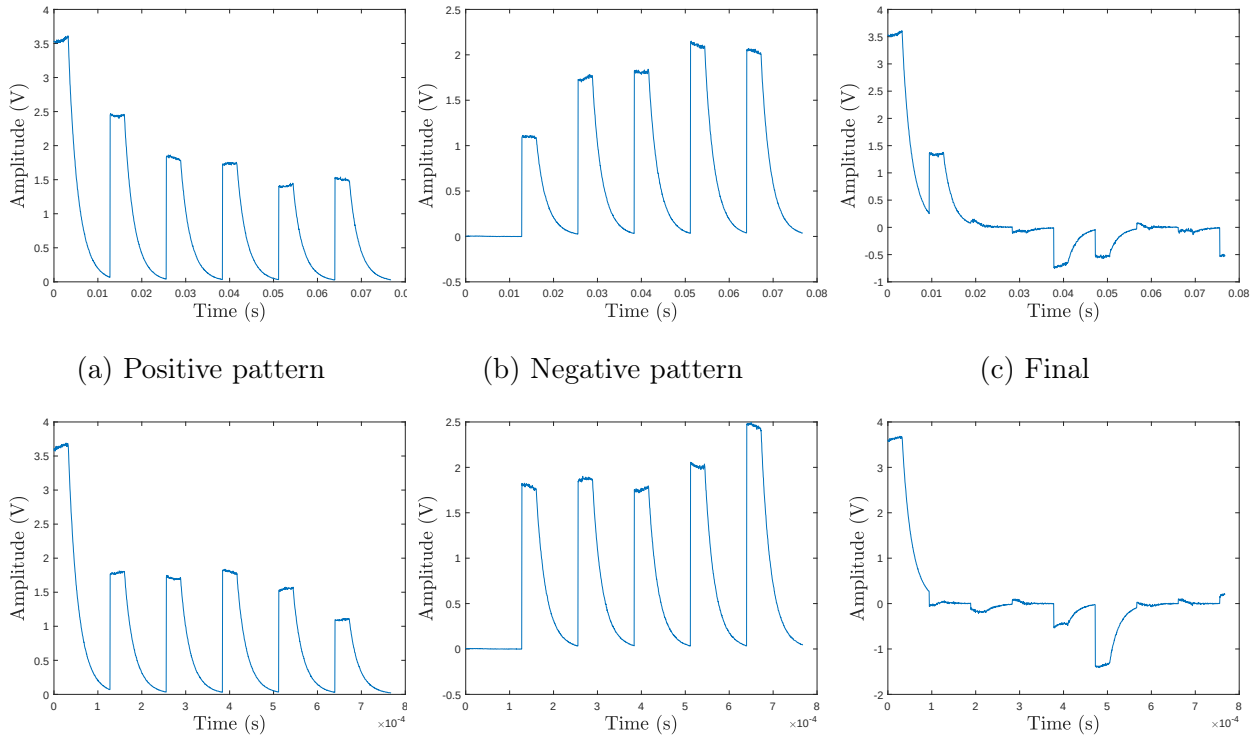

(a) Positive pattern (b) Negative pattern (c) Final

(d) Positive pattern (e) Negative pattern (f) Final

Figure 4.8: Electrical signals showing 6 patterns. The first row shows the Walsh ordering electrical signals of the positive patterns measurements (a), negative (b) and the difference between them (c). The second row, ((d), (e), (f)) shows the same signals but using a Block ordering.

TVAL3 was used to reconstruct a stack of 189 images for both Walsh and Block orderings. Figures 4.9, 4.10, 4.11 and 4.12 show the reconstructed 128×128 images of the D1 and D3 solutions on both sides of the holder, for 10% and 5% compression ratios, with times after stimulus of 0, 11.5 and 21.5 ms. Since the images were recovered using post-trigger data, as the time increases, the light emitted by the phosphorescent samples decreases, resulting in the same intensity decrease inside ROIs. This decay is clearly visible on the D1 solution, which presents high Pt(II) ring-fused chlorins concentration, and so, higher light emission. Oppositely, D3 regions shows low intensity values. The reconstructed images of both Walsh, figures figures 4.9 and 4.10, and Block orderings, 4.11 and 4.12, and both compression ratios provide similar information. Even though the Block ordering was used because Walsh images displayed a pixel stretching phenomenon for low CRs, this last ordering presents better image quality than the Block one for both CRs.

Comparing with the proof-of concept, the segmented ROIs in this experiment are smaller, corresponding exclusively to the solutions area. Even though the length and width of the ROIs were the same across all images and maps, the place of the rectangle changed according to the samples position on the image. These slight differences in the samples positions were caused by small variations of the experimental setup alignment. By replacing the samples or switching its positions on the holder, small changes in the height of the holder or of the photodetector may occur. Therefore, the ROIs position changed for each scene, D1/D3, D3/D1, D1/D2,D2/D1, D2/D3, D3/D2; however, it did not changed within the acquisitions of the 6 ventilation times.

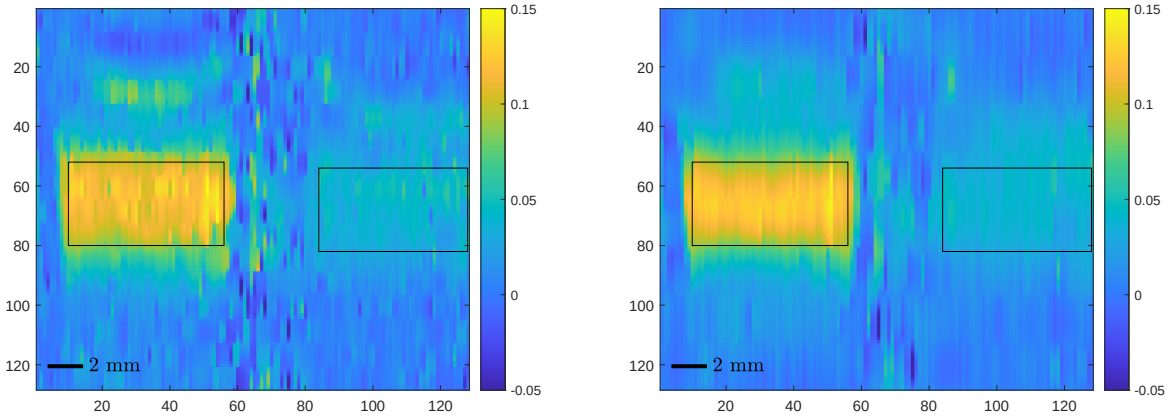

(a) CR = 10%

(b) CR = 5%

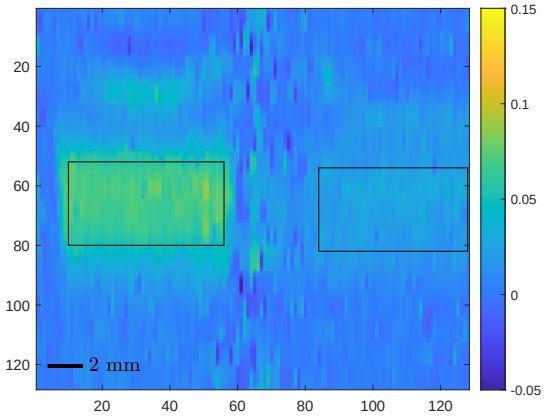

(c) CR = 10%

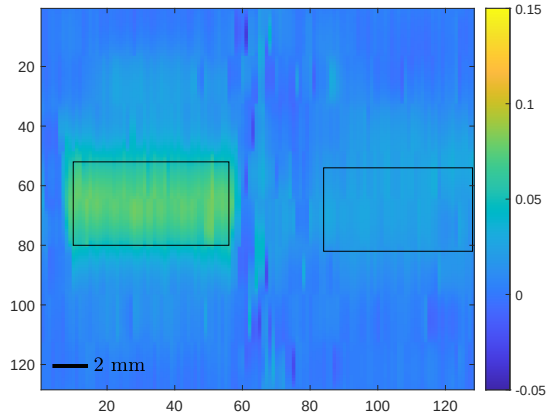

(d) CR = 5%

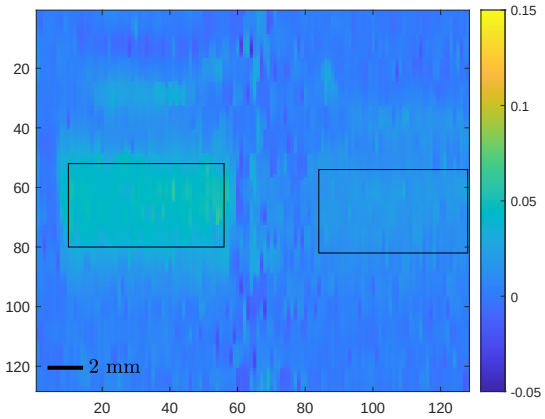

(e) CR = 10%

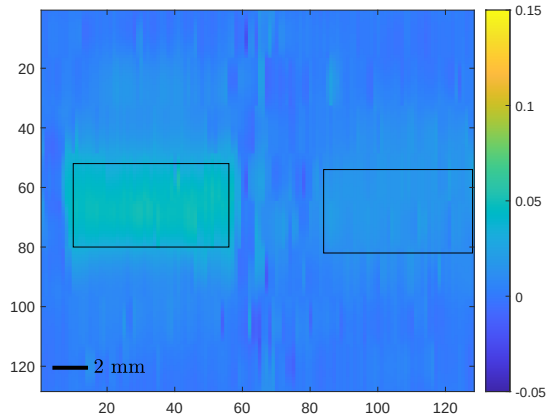

(f) CR = 5%

Figure 4.9: Walsh ordering reconstructed images, for 10% and 5% compression ratios, with D1 on the left side of the holder and D3 on the right, for times after stimulus of 0, 11.5 and 21.5 ms.

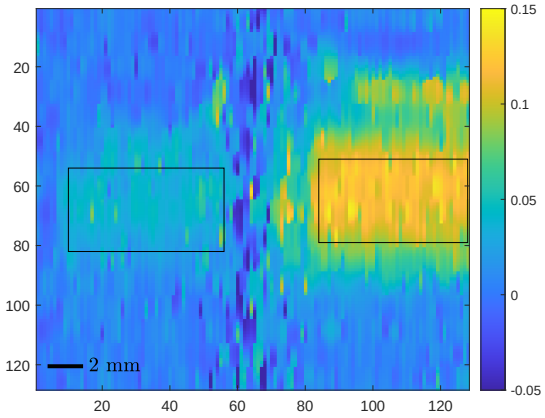

(a) CR = 10%

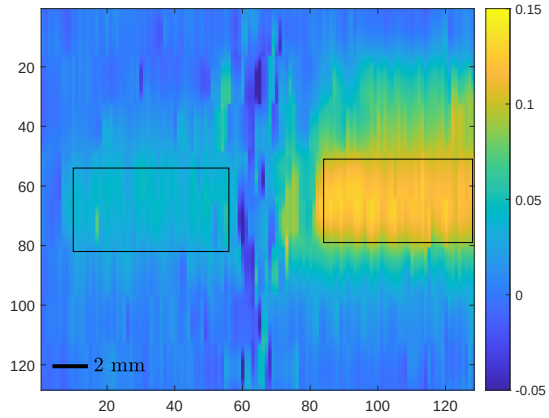

(b) CR = 5%

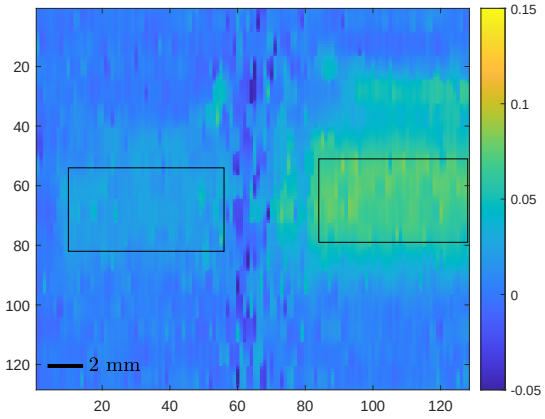

(c) CR = 10%

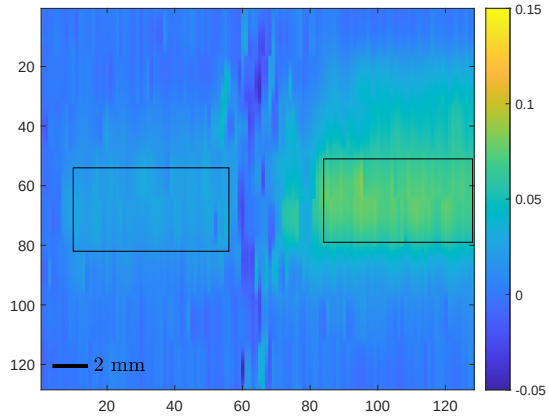

(d) CR = 5%

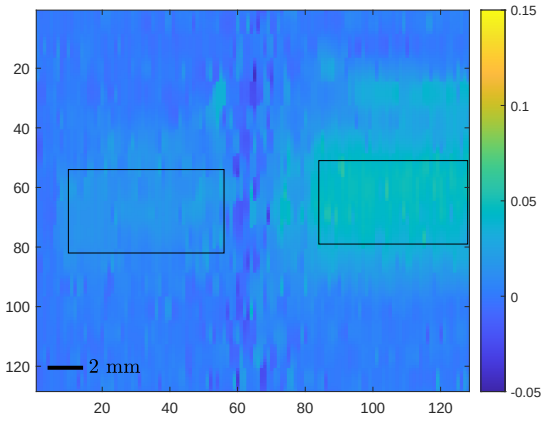

(e) CR = 10%

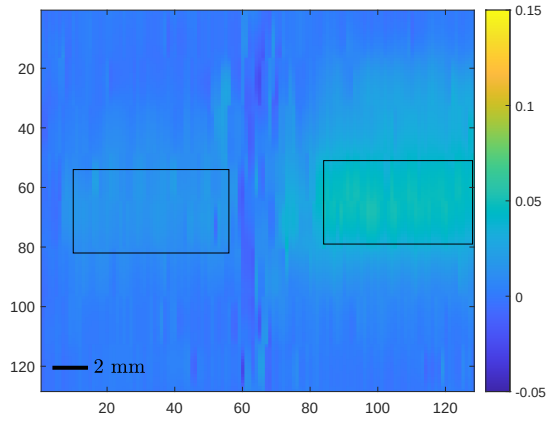

(f) CR = 5%

Figure 4.10: Walsh ordering reconstructed images, for 10% and 5% compression ratios, with D3 on the left side of the holder and D1 on the right, for times after stimulus of 0, 11.5 and 21.5 ms.

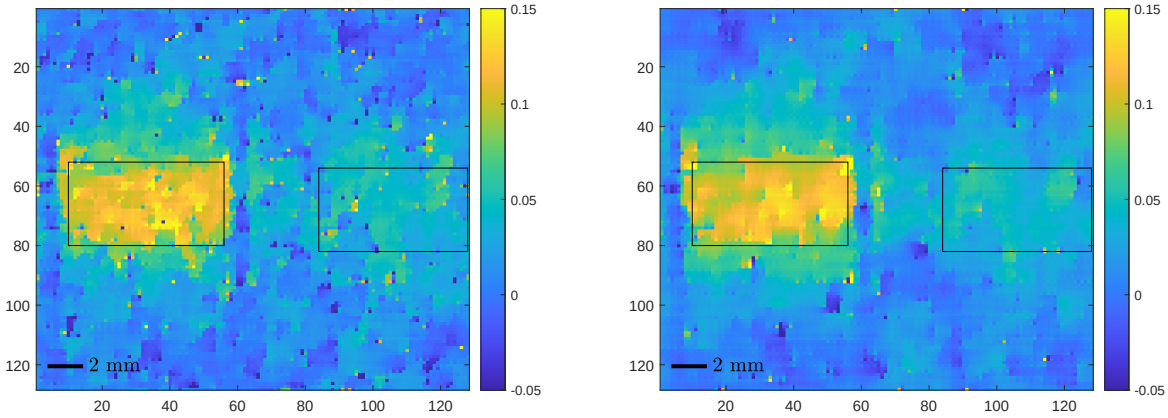

(a) CR = 10%

(b) CR = 5%

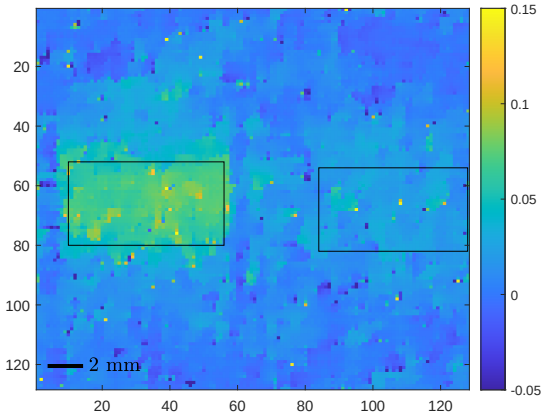

(c) CR = 10%

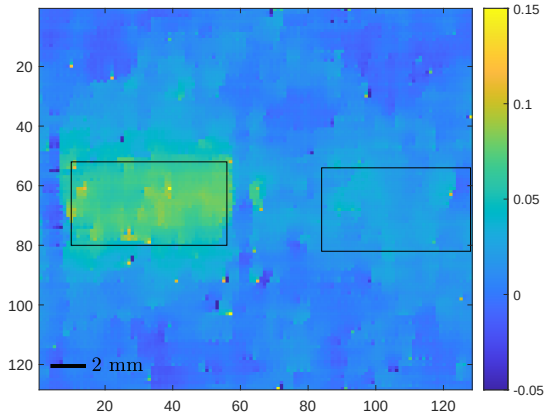

(d) CR = 5%

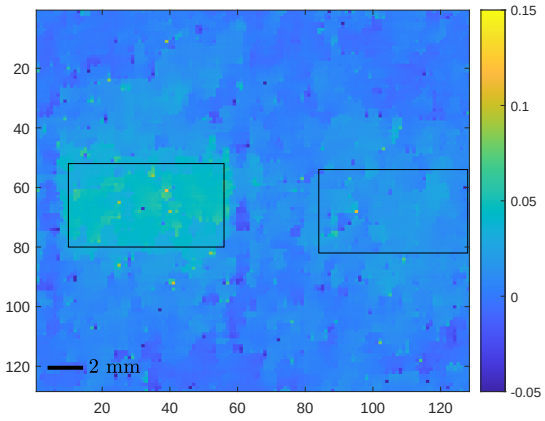

(e) CR = 10%

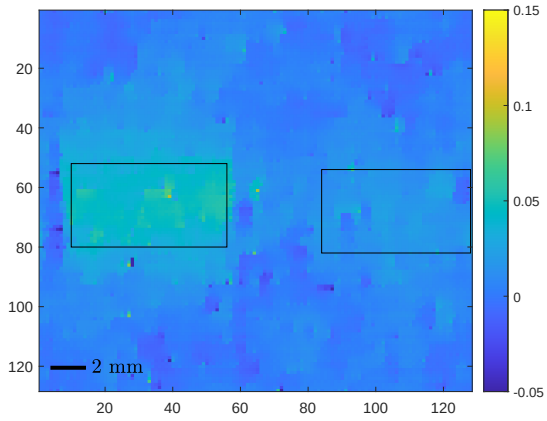

(f) CR = 5%

Figure 4.11: Block ordering reconstructed images, for 10% and 5% compression ratios, with D1 on the left side of the holder and D3 on the right, for times after stimulus of 0, 11.5 and 21.5 ms.

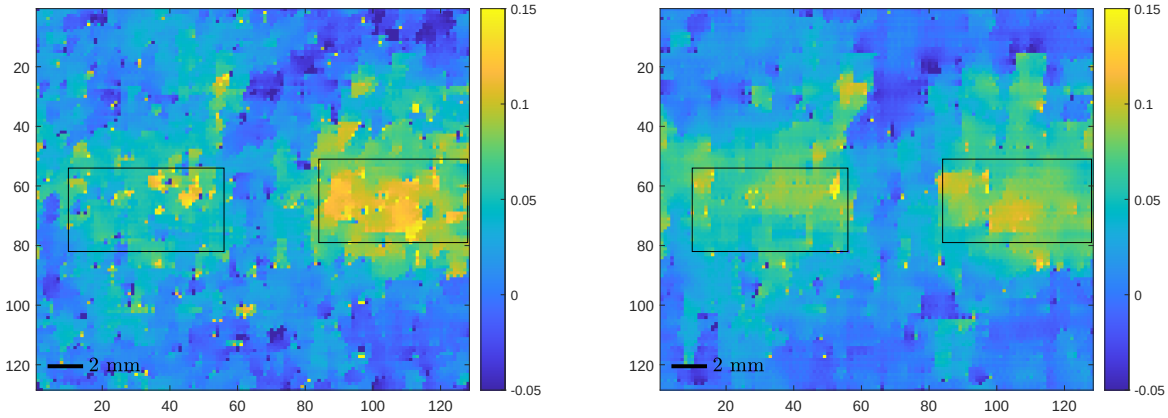

(a) CR = 10%

(b) CR = 5%

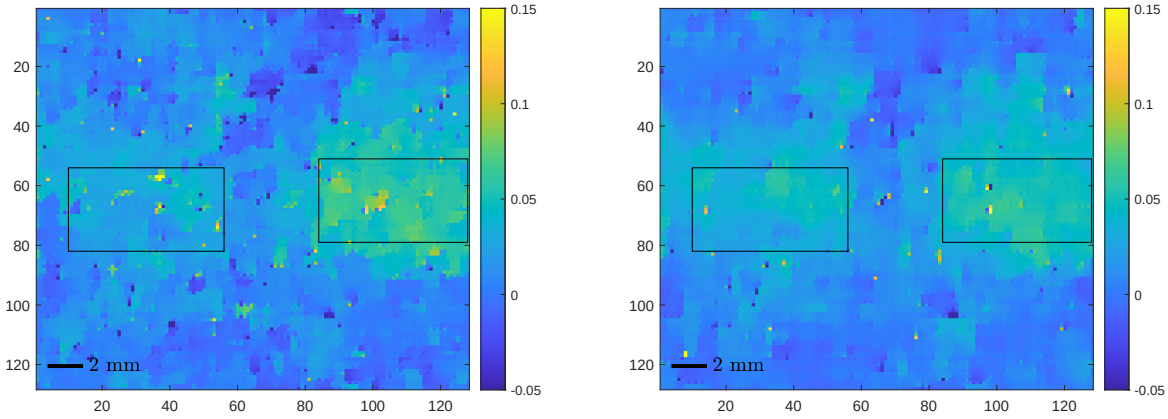

(c) CR = 10%

(d) CR = 5%

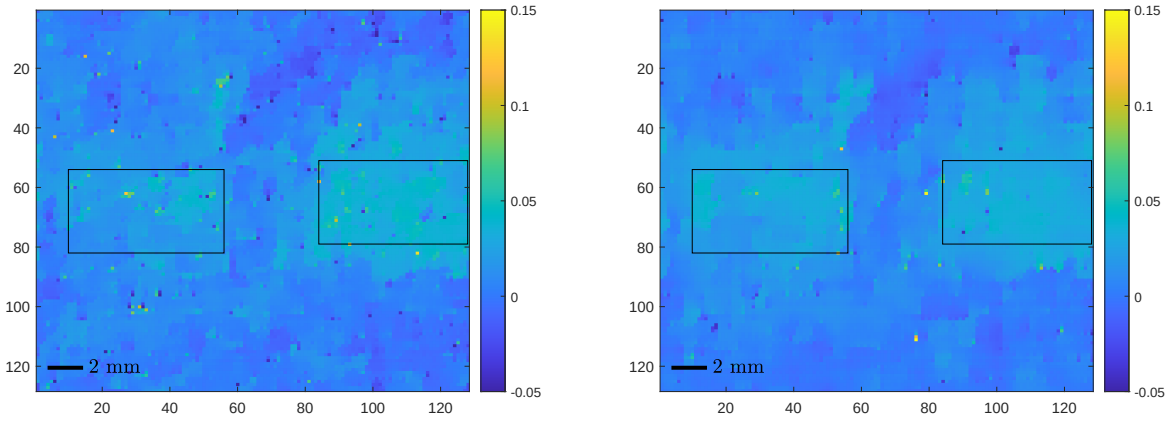

(e) CR = 10%

(f) CR = 5%

Figure 4.12: Block ordering reconstructed images, for 10% and 5% compression ratios, with D3 on the left side of the holder and D1 on the right, for times after stimulus of 0, 11.5 and 21.5 ms.

The mean of the ROIs of the 189 images were calculated and used to obtain the phosphorescence lifetime by fitting the values to an exponential decay curve, 3.3, using the MATLAB function `fit()`. Figure 4.13 shows the phosphorescence curves of D1 and D3 solutions for both Walsh and Block orderings. In the first column, the D1 solution was studied for 0 seconds (blue) GN_2 ventilation and 150 seconds (yellow), with both curves showing an exponential decay. The maximum intensity of both curves are around 0.11 AU. Table 4.3 presents the phosphorescence lifetime values obtained in the curves, showing that the lifetime values of the 150 seconds are slightly lower than the 0 seconds, which was not expected. This suggests that the SPC is not sensitive to the signal variations caused by the different oxygen concentrations in the solutions. In the second column, both phosphorescence curves of D1 and D3 solutions for 150 seconds ventilation are shown, with D3 presenting higher lifetime values than D1 and showing an approximate maximum intensity value of 0.12 AU for D1 and 0.04 AU for D3. Therefore, the setup is sensitive to the Pt(II) ring-fused chlorins concentration.

Similarly to the proof-of-concept, to obtain the intensity maps, a stack of 64 images, using the pre-trigger points, were reconstructed and reshaped to 64×64 resolution images. The phosphorescence intensity maps were formed by obtaining the mean pixel value of each pixel along the 64 images. The maps provide similar information as the reconstructed images, showing D1 sample with higher intensity values than the D3 solution. Figures 4.14 and 4.15 show the phosphorescence intensity maps with the D1 on the left side of the holder and D3 on the right, while figures 4.16 and 4.17 show the intensity maps with the inverse solutions positions (D3/D1). Each figure has three rows, the first, (a), (b), showing the results with the left sided sample ventilated with GN_2, the second, (c), (d), with both samples ventilated, and the third, (e), (f), with the right sided solution ventilated. Each row has the maps with the sample with 0 and 150 seconds GN_2 ventilation times. As the solution is sequentially ventilated, it is expected the intensity values to raise and lifetime to increase.

Comparing to the previous experiment, both reconstructed images and intensity maps show a more even representation of the samples on both left and right positions, since the solutions appear in all the ROIs area. This means that photodetector received a more balanced light coming from both sides of the support.

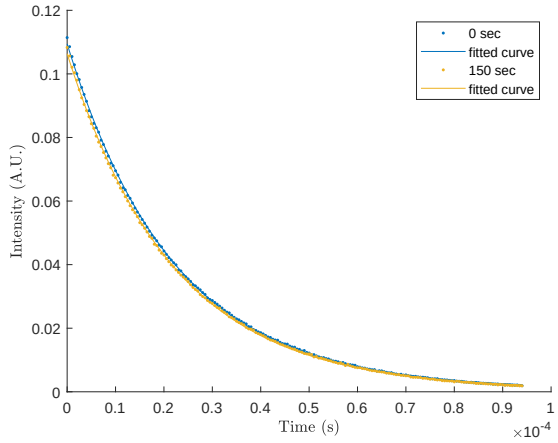

(a) Walsh

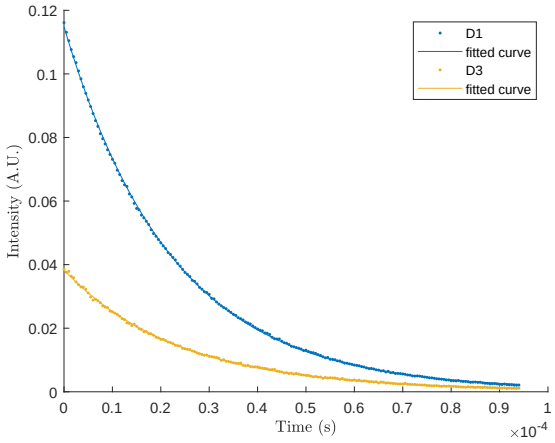

(b) Walsh

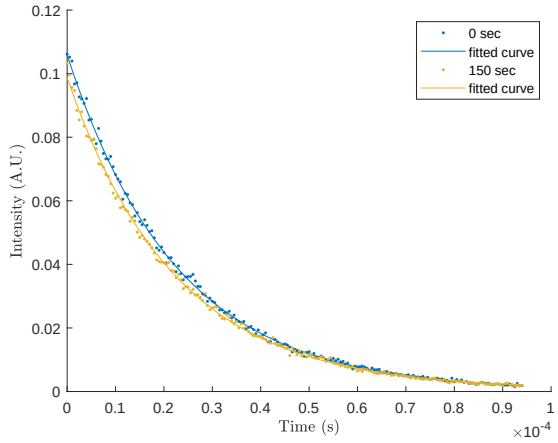

(c) Block

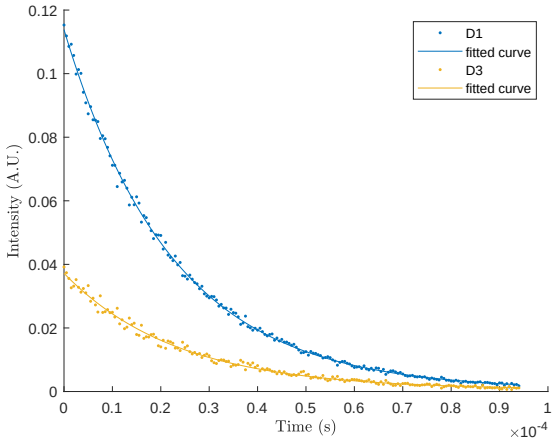

(d) Block

Figure 4.13: Phosphorescence lifetime curves. The first column, (a), (c), presents the D1 curves, with 0 (blue) and 150 seconds (yellow) of GN_2 ventilation. The second column, (b), (d), show the D1 (blue) and D3 (yellow), with 150 seconds of ventilation.

Table 4.3: Lifetime values (μs) obtained from the curves of the figure 4.13 for the 5% compression ratio.

Curves	Walsh	Block
blue (0 sec)	21.94	22.61
yellow (150 sec)	21.87	22.17

(a) D1, with 0 and 150 sec GN_2 ventilation

Curves	Walsh	Block
blue (D1)	22.19	22.34
yellow (D3)	23.71	23.36

(b) D1 and D3, with 150 sec GN_2 ventilation

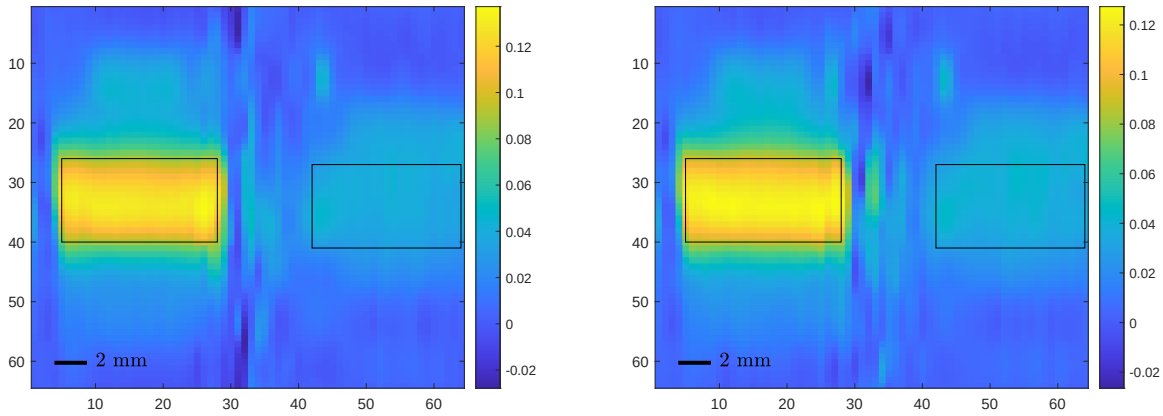

(a) 0 sec

(b) 150 sec

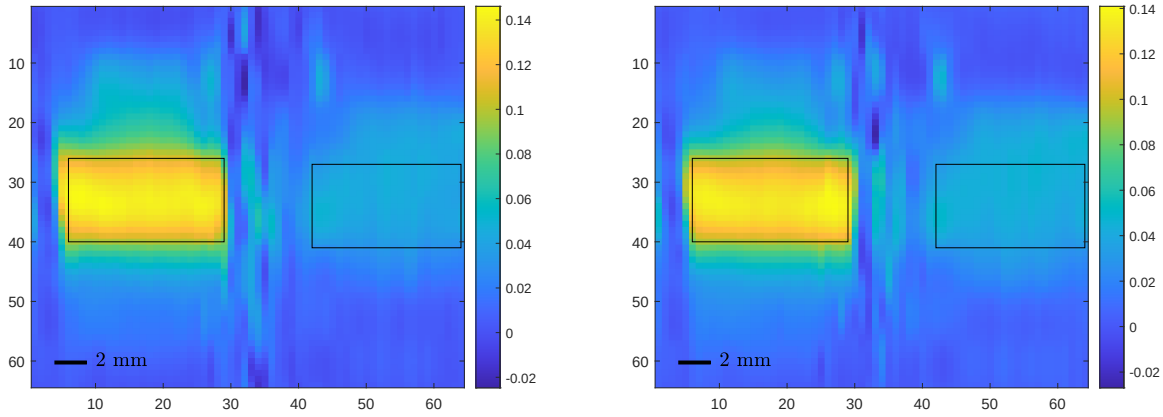

(c) 0 sec

(d) 150 sec

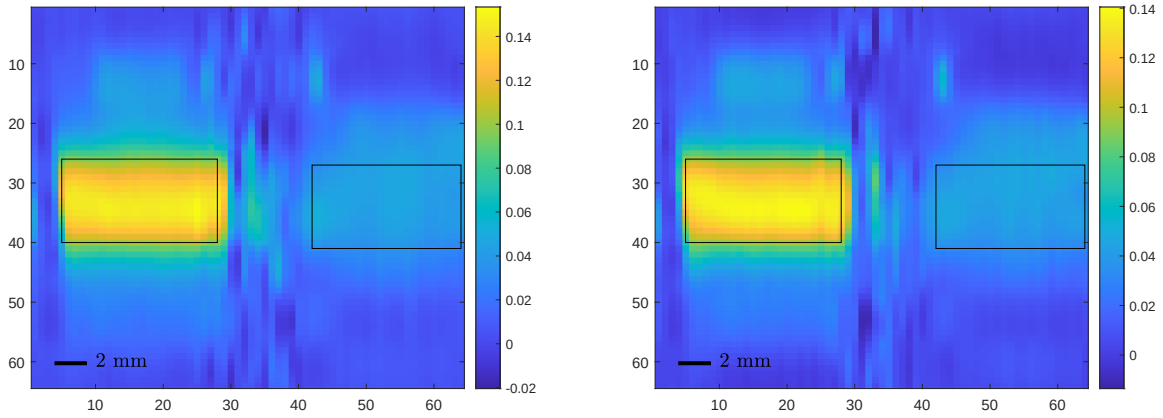

(e) 0 sec

(f) 150 sec

Figure 4.14: Walsh ordering phosphorescence intensity maps obtained with 5% compression ratio, with the D1 on the left side of the holder and D3 on the right. The first row shows the maps for 0 and 150 seconds GN_2 ventilation times, with the left sided sample ventilated, the second with both and the third with the right sided sample ventilated.

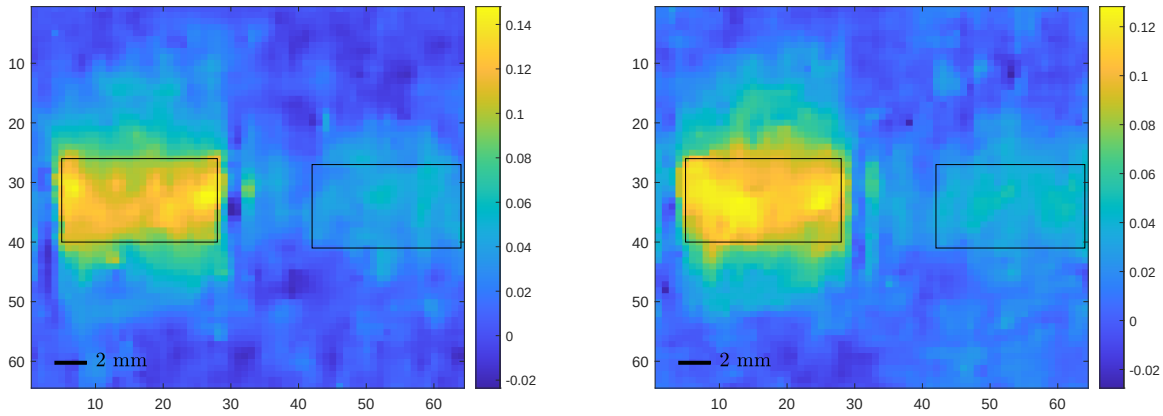

(a) 0 sec

(b) 150 sec

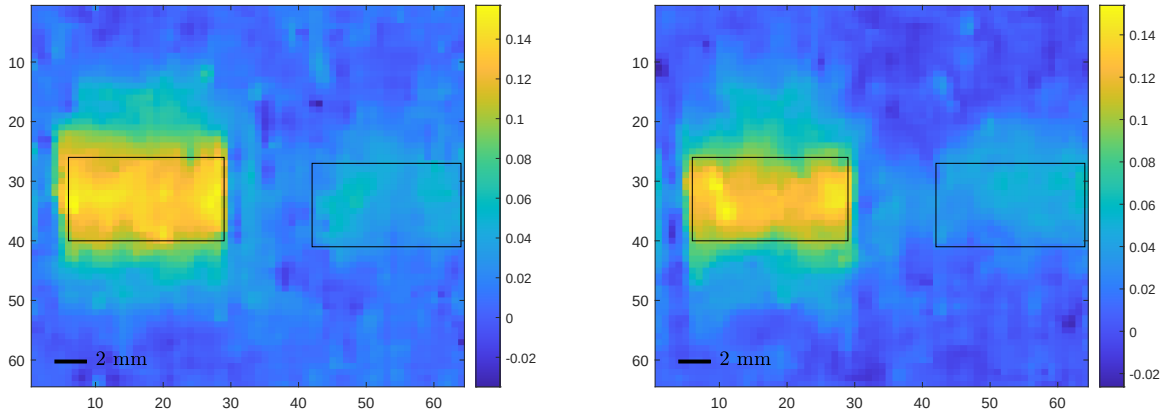

(c) 0 sec

(d) 150 sec

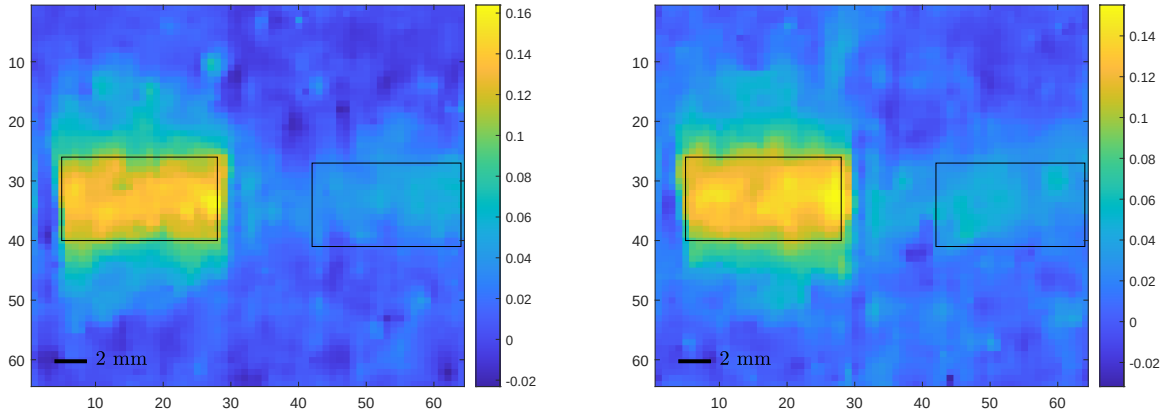

(e) 0 sec

(f) 150 sec

Figure 4.15: Block ordering phosphorescence intensity maps obtained with 5% compression ratio, with the D1 on the left side of the holder and D3 on the right. The first row shows the maps for 0 and 150 seconds GN_2 ventilation times, with the left sided sample ventilated, the second with both and the third with the right sided sample ventilated.

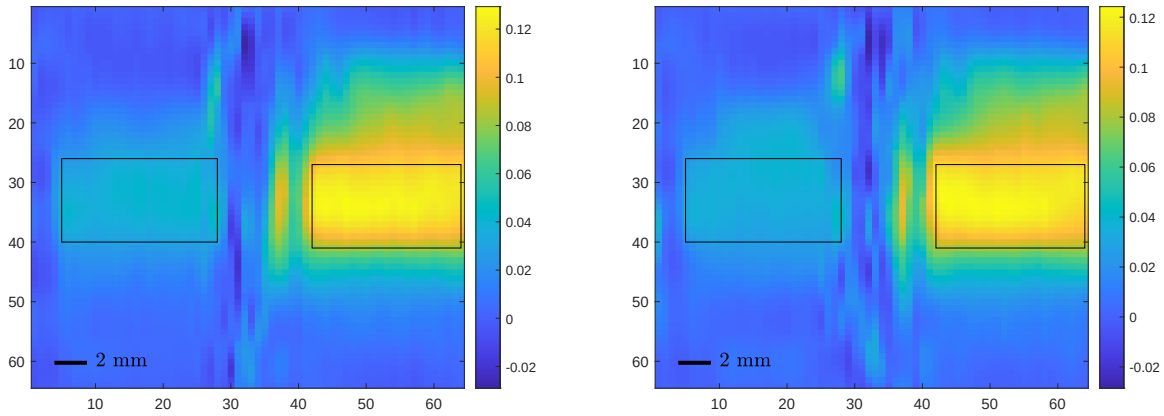

(a) 0 sec

(b) 150 sec

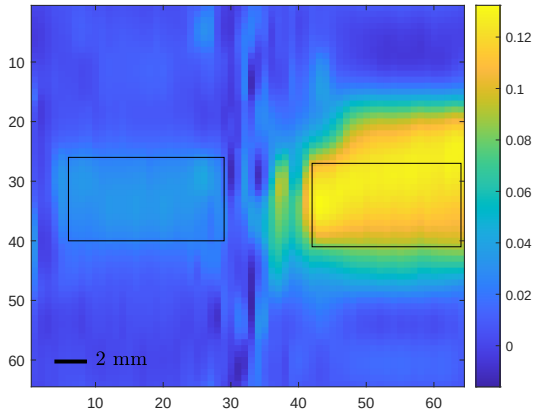

(c) 0 sec

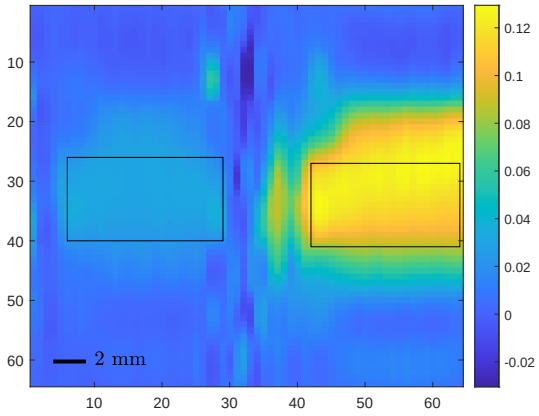

(d) 150 sec

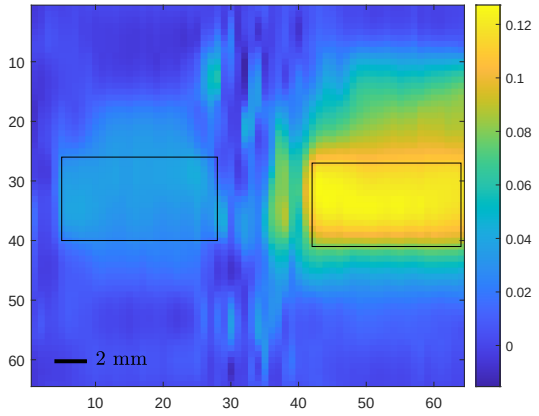

(e) 0 sec

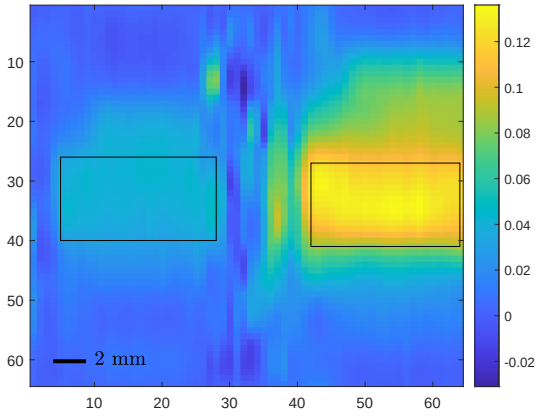

(f) 150 sec

Figure 4.16: Walsh ordering phosphorescence intensity maps obtained with 5% compression ratio, with the D3 on the left side of the holder and D1 on the right. The first row shows the maps for 0 and 150 seconds GN_2 ventilation times, with the left sided sample ventilated, the second with both and the third with the right sided sample ventilated.

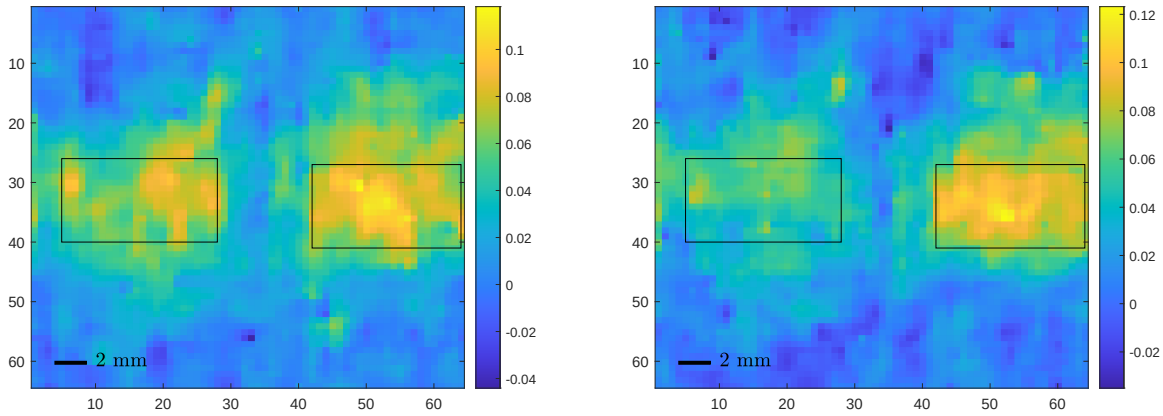

(a) 0 sec

(b) 150 sec

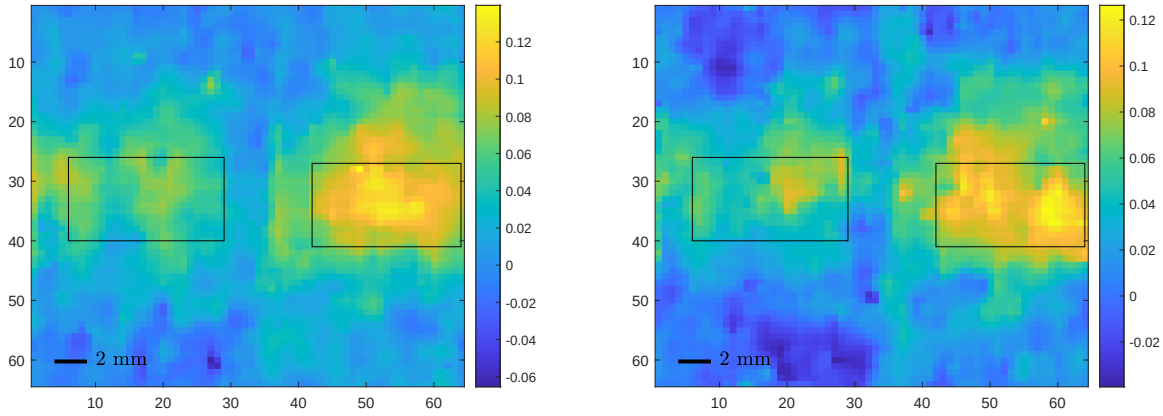

(c) 0 sec

(d) 150 sec

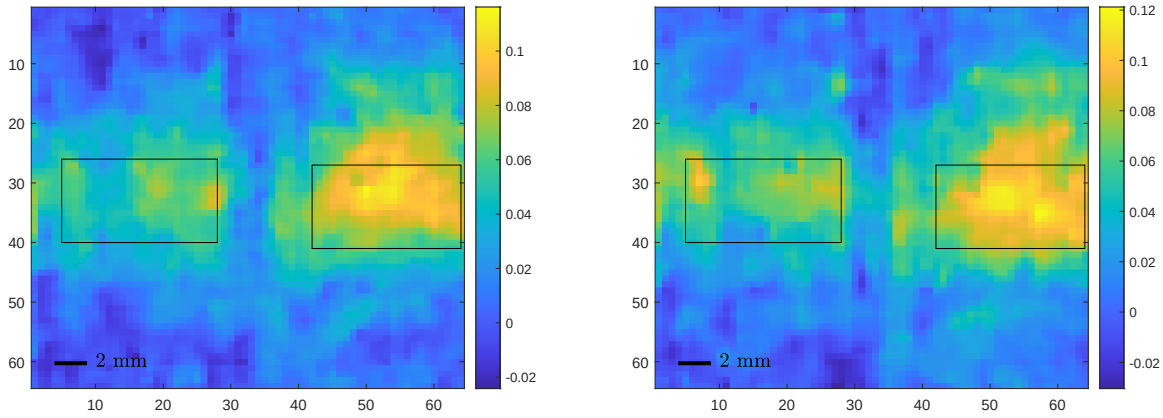

(e) 0 sec

(f) 150 sec

Figure 4.17: Block ordering phosphorescence intensity maps obtained with 5% compression ratio, with the D3 on the left side of the holder and D1 on the right. The first row shows the maps for 0 and 150 seconds GN_2 ventilation times, with the left sided sample ventilated, the second with both and the third with the right sided sample ventilated.

The post-trigger points were used to reconstruct a stack of 189 images. Similarly to the intensity maps, these images were first reshaped to a 64×64 resolution, and then, using a pixel-by-pixel approach, were used to determine the phosphorescence lifetime maps. Figures 4.18 and 4.19 and figures 4.20 and 4.21 show the lifetime maps of D1 and D3 solutions on both positions on the holder and for both Hadamard orderings. As in phosphorescence intensity figures, both 0 and 150 seconds ventilation times maps are shown for the 3 scenarios.

The phosphorescence lifetime depends on the amount of oxygen present on the solutions. Therefore, as the GN_2 ventilation time increases, the lifetime values should increase as well. However, the maps show that D1 solution presents lower lifetime values than D3, regardless the ventilation time.

The results are presented in tables 4.4 and 4.5, with both D1 and D3 ventilated. The other results tables are presented in Appendix A, which provides equivalent information.

Consistent lifetime results for 10% and 5% compression ratios were obtained, suggesting that, for this study, 5% is more suitable to be used, since it enables to reduce the number of coefficients acquired, and so, the acquisition time. Regardless the ordering, the D3 lifetime values are higher than D1 ones and the standard deviations are one or two orders lower than the mean. However, due to the noise in the maps, some standard deviations are higher than the mean, whose corresponding mean values are out of the lifetime ranges of both samples. D1 lifetime mean values vary around 22 μs, while D3 stands around 23-24 μs.

The lifetime values do not increase as the GN_2 ventilation time increases and no pattern is verified along the values, not enabling to relate the lifetime values with the ventilation time.

Regarding the phosphorescence intensity, the mean values of the D1 solution are one order higher than the D3, for both orderings and CRs, with D1 ranging from 0.1277 to 0.0857 AU and D3 from 0.0662 to 0.029 AU. The intensity values are more consistent than the lifetime ones, as expected. The standard deviations are also one order lower than the mean values.

Block ordering lifetime maps seem to be noisier than the Walsh ordering ones, even though both show low SNR. This may explain the fact that the Block ordering presents more inconsistent mean lifetime values than the Walsh one. Therefore, Walsh ordering was proven to be more suitable to this study, providing better image's quality. The non dependency of the intensity nor lifetime over the ventilation time may be justified by the poor system sensitivity to the signal variations caused by the sequential ventilation. Moreover, the ventilation time of 30 seconds may have not been suitable for this study. This value

may be too short to cause any significant variation to be detected by the setup, since in the proof-of-concept it was used 30 minutes of ventilation time and, in this one, it was only used 30 seconds.

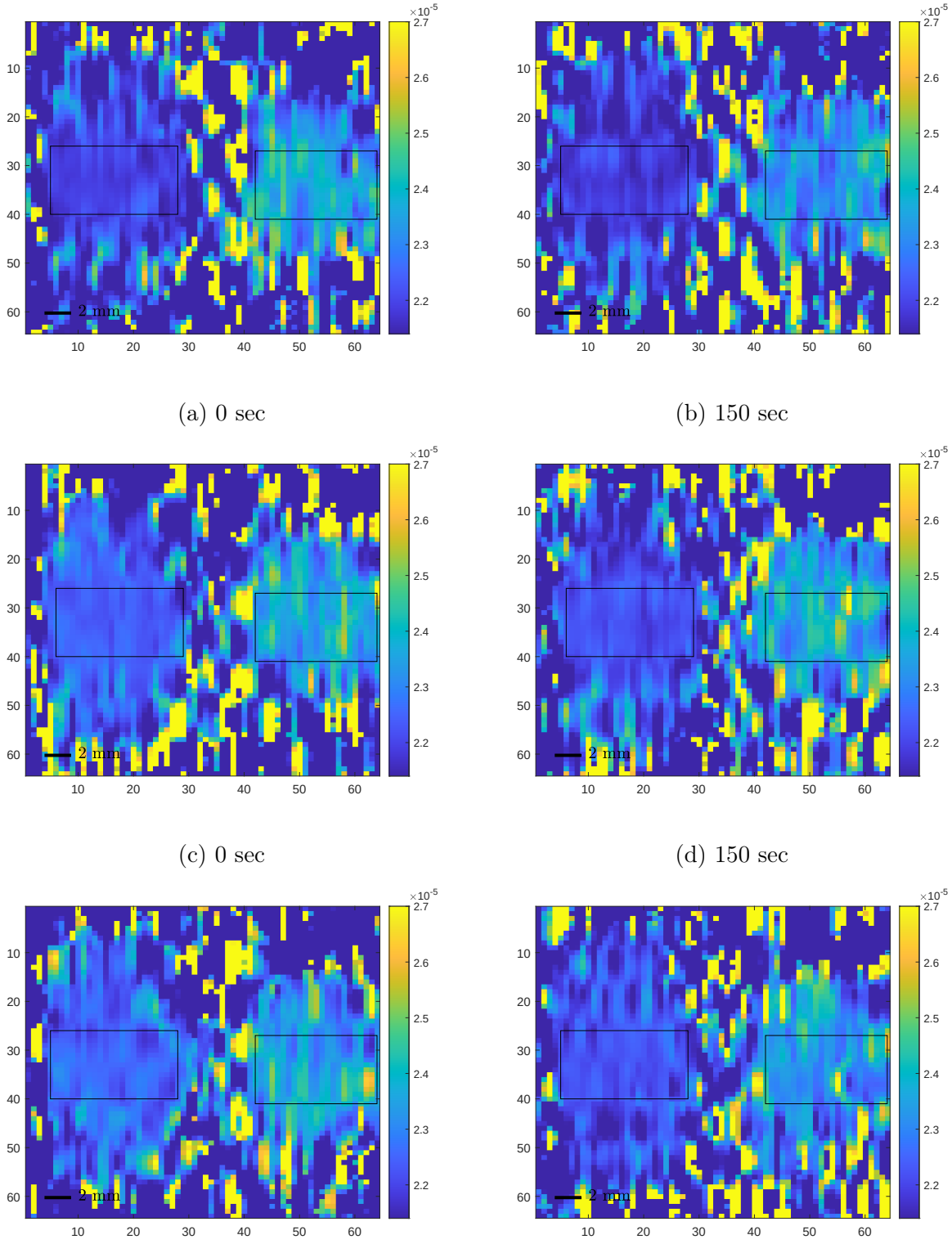

(a) 0 sec

(b) 150 sec

(c) 0 sec

(d) 150 sec

(e) 0 sec

(f) 150 sec

Figure 4.18: Walsh ordering phosphorescence lifetime maps obtained with 5% compression ratio, with the D1 on the left side of the holder and D3 on the right. The first row shows the maps for 0 and 150 seconds GN_2 ventilation times, with the left sided sample ventilated, the second with both and the third with the right sided sample ventilated.

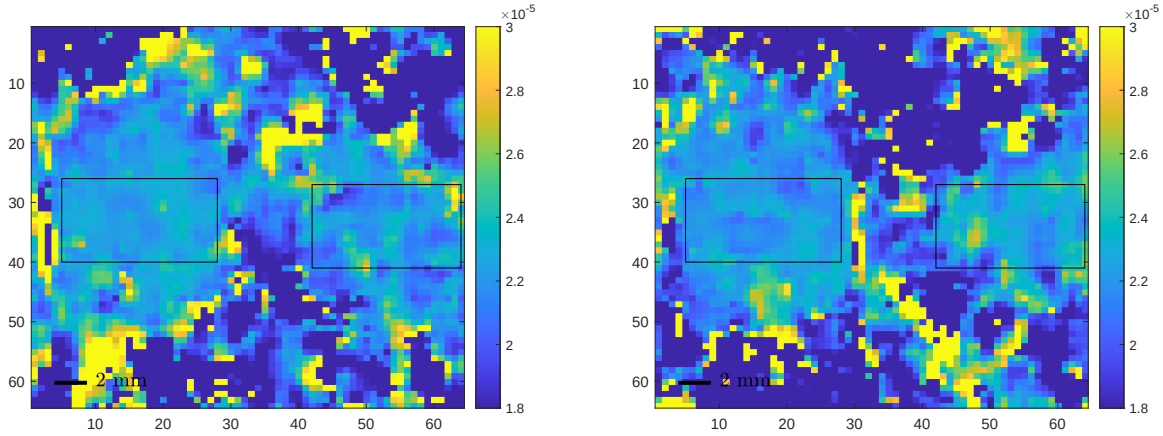

(a) 0 sec

(b) 150 sec

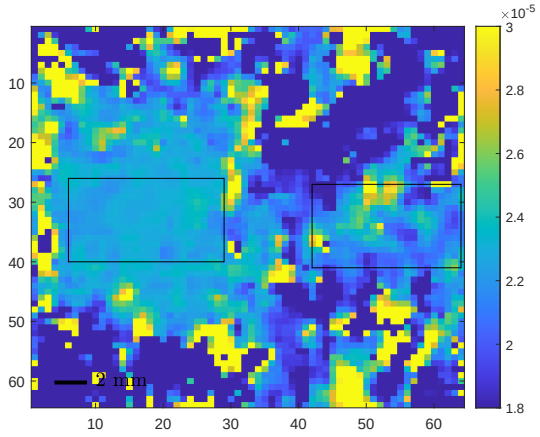

(c) 0 sec

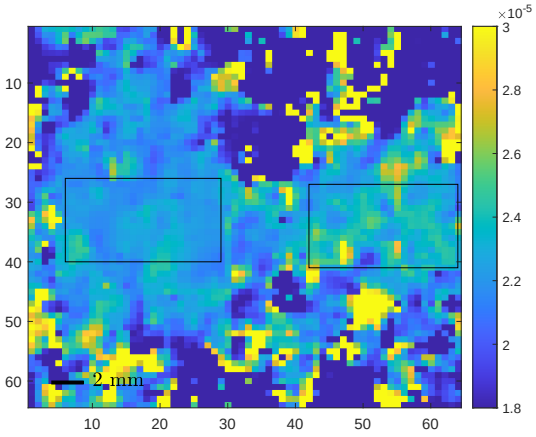

(d) 150 sec

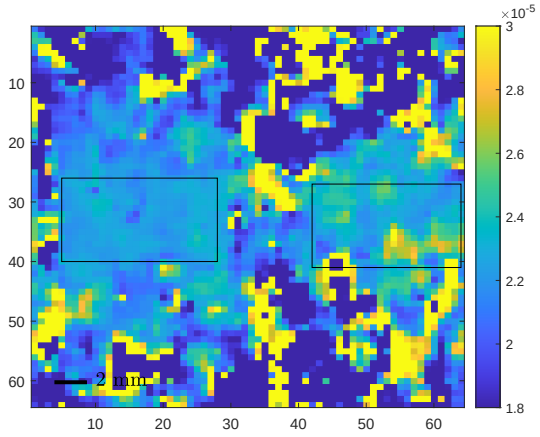

(e) 0 sec

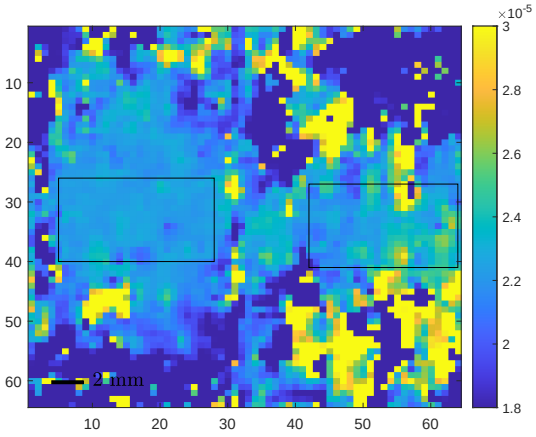

(f) 150 sec

Figure 4.19: Block ordering phosphorescence lifetime maps obtained with 5% compression ratio, with the D1 on the left side of the holder and D3 on the right. The first row shows the maps for 0 and 150 seconds GN_2 ventilation times, with the left sided sample ventilated, the second with both and the third with the right sided sample ventilated.

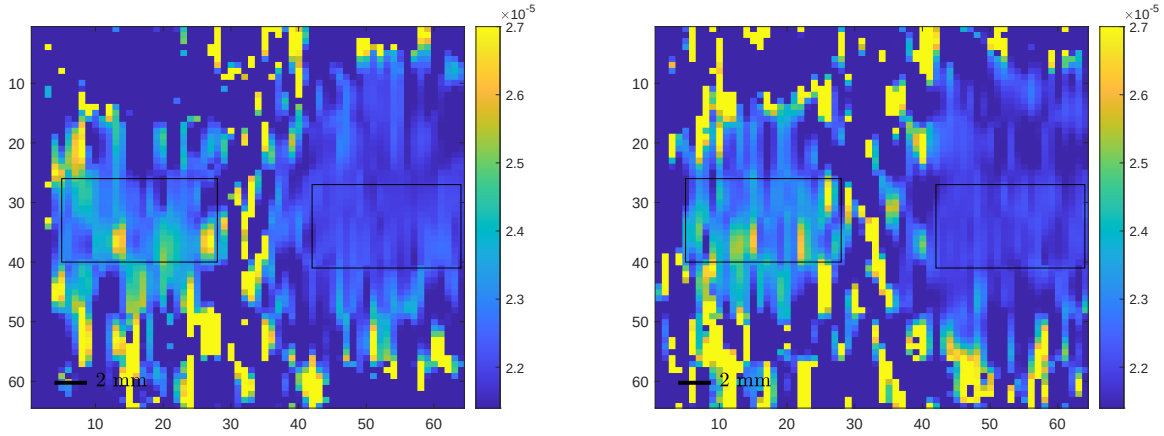

(a) 0 sec

(b) 150 sec

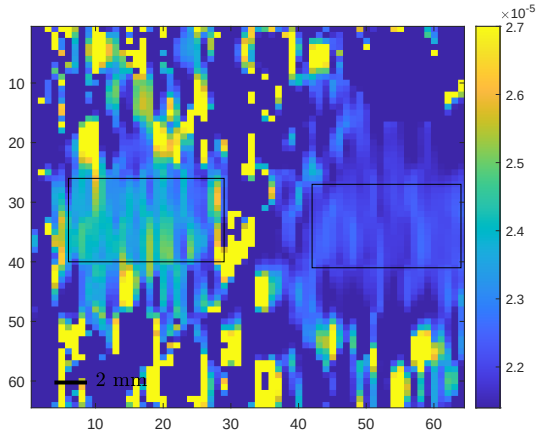

(c) 0 sec

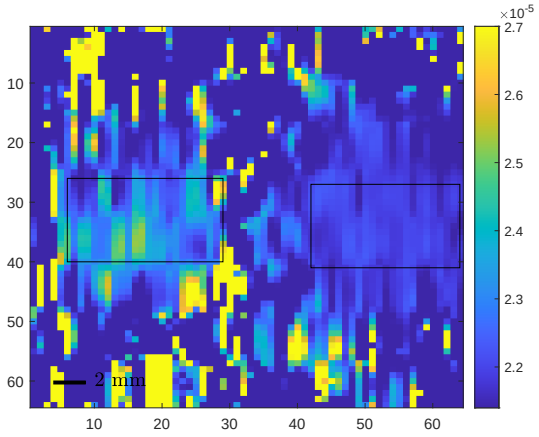

(d) 150 sec

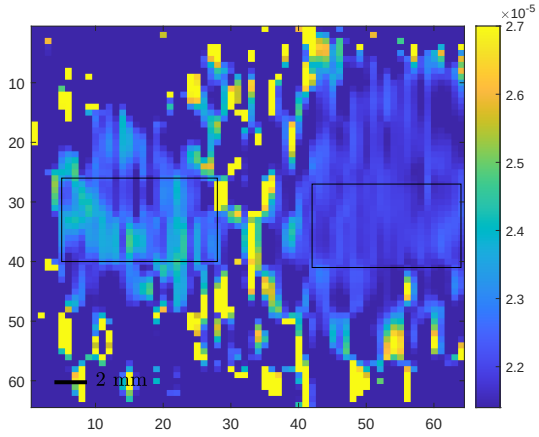

(e) 0 sec

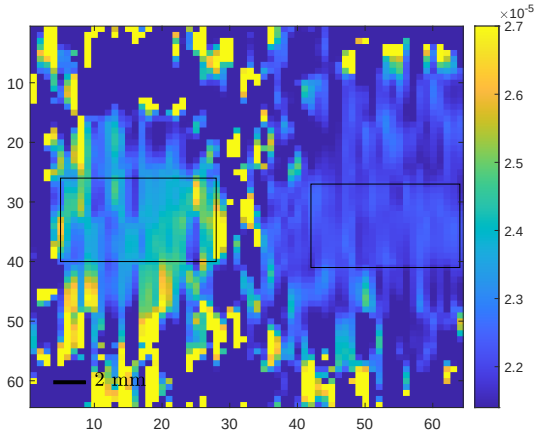

(f) 150 sec

Figure 4.20: Walsh ordering phosphorescence lifetime maps obtained with 5% compression ratio, with the D3 on the left side of the holder and D1 on the right. The first row shows the maps for 0 and 150 seconds GN_2 ventilation times, with the left sided sample ventilated, the second with both and the third with the right sided sample ventilated.

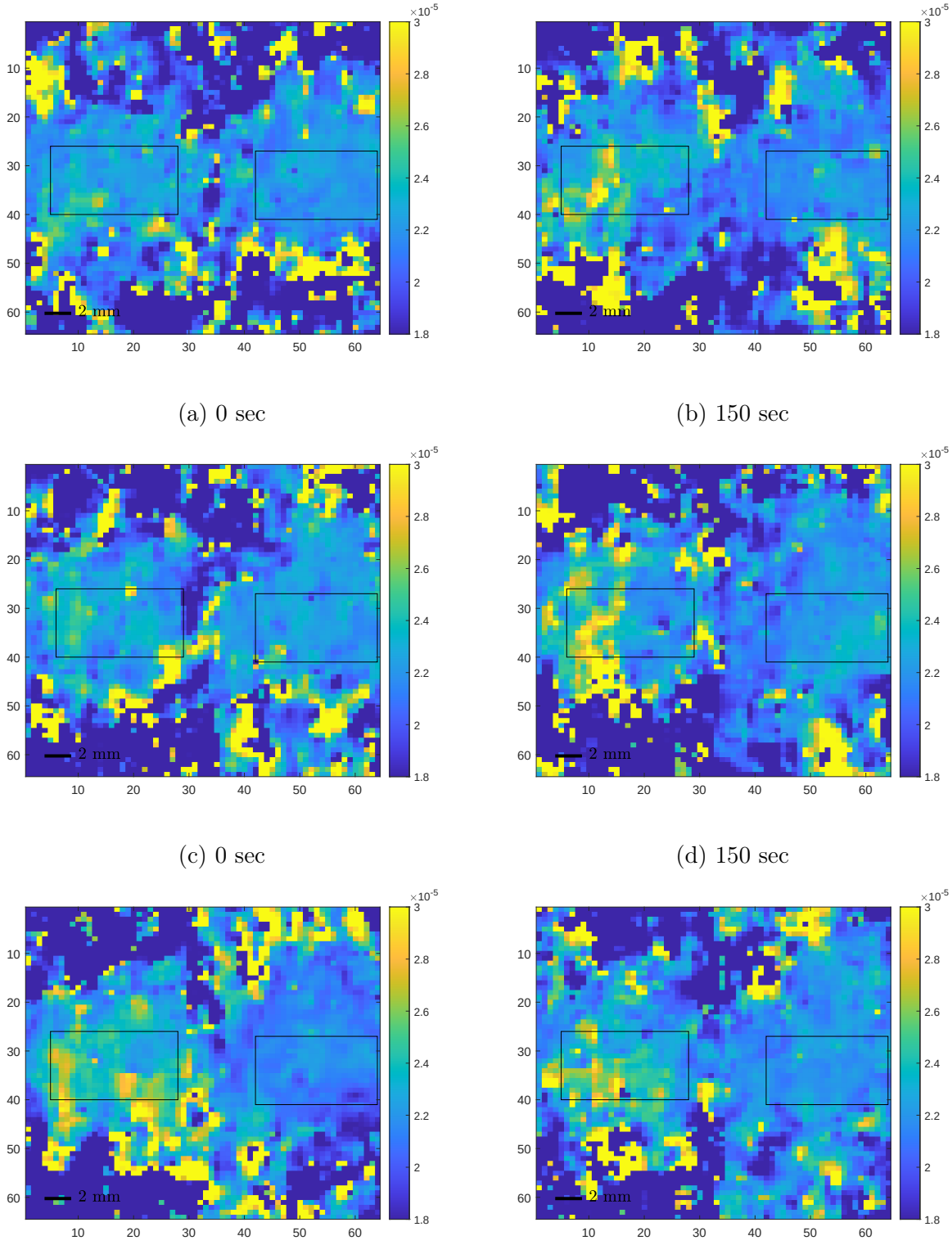

(a) 0 sec

(b) 150 sec

(c) 0 sec

(d) 150 sec

(e) 0 sec

(f) 150 sec

Figure 4.21: Block ordering phosphorescence lifetime maps obtained with 5% compression ratio, with the D3 on the left side of the holder and D1 on the right. The first row shows the maps for 0 and 150 seconds GN_2 ventilation times, with the left sided sample ventilated, the second with both and the third with the right sided sample ventilated.

Table 4.4: Mean phosphorescence lifetime and intensity values and their corresponding values for the GN_2 ventilation times of 0, 30, 60, 90, 120, 150 seconds and for 10% and 5% compression ratios. D1 and D3 were both GN_2 ventilated.

	sec	CR	**D1**				**D3**			
			$\overline{\tau}(\mu s)$	$\sigma_{\overline{\tau}}(\mu s)$	$\overline{I}$	$\sigma_{\overline{I}}$	$\overline{\tau}(\mu s)$	$\sigma_{\overline{\tau}}(\mu s)$	$\overline{I}$	$\sigma_{\overline{I}}$
Walsh	0	10%	22.42	0.3	0.1244	0.012	23.77	1.1	0.042	0.005
		5%	22.42	0.3	0.1249	0.015	23.67	0.7	0.0411	0.005
	30	10%	22.25	0.4	0.118	0.017	23.6	0.9	0.0416	0.004
		5%	22.27	0.3	0.1176	0.015	23.6	0.6	0.0411	0.004
	60	10%	22.2	0.3	0.1214	0.016	23.6	1	0.0423	0.005
		5%	22.2	0.2	0.1205	0.013	23.63	0.8	0.0417	0.004
	90	10%	22.15	0.4	0.1194	0.014	23.69	0.8	0.0416	0.005
		5%	22.14	0.3	0.1192	0.015	23.66	0.6	0.0411	0.004
	120	10%	22.22	0.3	0.12	0.013	23.42	0.9	0.0414	0.005
		5%	22.22	0.2	0.12	0.015	23.42	0.6	0.0408	0.004
	150	10%	22.19	0.3	0.1194	0.013	23.85	1.3	0.0412	0.004
		5%	22.2	0.2	0.1191	0.014	23.79	0.9	0.0408	0.004
Block	0	10%	22.43	0.9	0.1227	0.015	20.12	120.1	0.0392	0.008
		5%	22.8	0.6	0.1277	0.014	22.75	14.1	0.0371	0.01
	30	10%	22.24	0.7	0.1192	0.017	24.32	5.9	0.0368	0.012
		5%	22.33	0.5	0.1149	0.017	23.05	11.1	0.0397	0.011
	60	10%	22.21	0.8	0.1215	0.017	25.62	19.2	0.0374	0.01
		5%	22.78	0.9	0.1176	0.018	22.23	4	0.0377	0.014
	90	10%	22.15	0.8	0.1213	0.016	26.77	23.5	0.0402	0.011
		5%	23.74	22.3	0.1204	0.016	23.27	3	0.0408	0.01
	120	10%	22.16	0.7	0.1218	0.017	25.03	14.5	0.0397	0.011
		5%	22.18	0.5	0.1169	0.016	23.58	1.9	0.0446	0.011
	150	10%	22.22	0.8	0.1188	0.018	26.28	19.3	0.0365	0.01
		5%	22.37	0.8	0.1158	0.016	23.57	2.1	0.0384	0.011

Table 4.5: Mean phosphorescence lifetime and intensity values and their corresponding values for the GN_2 ventilation times of 0, 30, 60, 90, 120, 150 seconds and for 10% and 5% compression ratios. D3 and D1 were both GN_2 ventilated.

	sec	CR	**D3**				**D1**			
			$\overline{\tau}(\mu s)$	$\sigma_{\overline{\tau}}(\mu s)$	$\overline{I}$	$\sigma_{\overline{I}}$	$\overline{\tau}(\mu s)$	$\sigma_{\overline{\tau}}(\mu s)$	$\overline{I}$	$\sigma_{\overline{I}}$
Walsh	0	10%	24.06	3.3	0.0295	0.005	22.12	0.4	0.1169	0.014
		5%	23.73	1.3	0.0294	0.005	22.12	0.2	0.1148	0.013
	30	10%	23.16	2.3	0.0303	0.006	22.01	0.4	0.1165	0.014
		5%	23.3	2	0.0299	0.005	22.04	0.2	0.1144	0.013
	60	10%	23.15	1.7	0.0298	0.005	21.99	0.3	0.117	0.014
		5%	22.98	1.3	0.0296	0.005	22	0.3	0.1148	0.013
	90	10%	23.47	1.5	0.0305	0.005	21.98	0.3	0.1146	0.013
		5%	23.34	0.9	0.0304	0.004	21.99	0.2	0.1126	0.013
	120	10%	23.1	1.8	0.0293	0.005	21.94	0.3	0.1154	0.014
		5%	22.98	1.1	0.0291	0.004	21.93	0.2	0.1132	0.012
	150	10%	23.25	2	0.0291	0.004	21.91	0.3	0.1151	0.014
		5%	23.18	1.2	0.029	0.004	21.93	0.2	0.1129	0.013
Block	0	10%	27.48	32.5	0.0424	0.014	22.44	4.8	0.1133	0.017
		5%	23.29	3.3	0.0539	0.015	22.45	2.2	0.096	0.017
	30	10%	25.26	11.5	0.044	0.015	22.15	1.1	0.1088	0.015
		5%	23.98	2.9	0.0559	0.015	22.25	0.8	0.0918	0.015
	60	10%	24.5	4.9	0.0544	0.017	21.73	0.8	0.1084	0.016
		5%	24.92	2.5	0.0658	0.017	21.3	0.8	0.0904	0.013
	90	10%	24.25	3.9	0.0473	0.014	21.99	0.9	0.1054	0.015
		5%	24.03	2.3	0.057	0.015	21.96	0.8	0.0906	0.016
	120	10%	24.5	5.7	0.0447	0.012	21.76	0.9	0.1026	0.016
		5%	22.99	1.5	0.059	0.014	22.14	0.8	0.0857	0.016
	150	10%	65.2	678.4	0.0387	0.018	21.96	0.8	0.1076	0.017
		5%	23.72	2.7	0.0536	0.016	22.24	1	0.0918	0.015

5 Conclusions

In this thesis, a single pixel camera setup was developed to perform simultaneous phosphorescence intensity and lifetime imaging, using the compressive sensing concepts. TVAL3 was the reconstruction algorithm used to recover images of the scene, which was composed by two cells with solutions containing Pt(II) ring-fused chlorins. In the proof-of-concept, one of these cells was GN_2 ventilated, which produced high intensity values on the reconstructed images and on the intensity maps, while the other sample, with O_2, did not. The low intensity values of the oxygenated cell were in the same order as the background noise, not being possible to identify it. The phosphorescence lifetime maps, which were obtained by fitting a pixel-by-pixel exponential decay, also enable to distinguish the two cells. Similarly, the deoxygenated sample's ROI presented high values, whereas the other was, once again, in the same order as the background noise. The results were consistent for the deoxygenated sample, for 25%, 10% and 5% compression ratios. For 1% , the intensity values were lower, suggesting that this ratio was not as suitable for this study. With this experiment, the SPC efficiency was proven, and so, the following step was to use a sequential GN_2 strategy to relate the lifetime values with the ventilation times and improve some limitations of the previous SPC scheme. One of the main problems was the imbalance on the light collection from the left to the right side of the holder, which was improved by changing the alignment. The solvent of the solution was also changed in order to improve the solution biocompatibility. In the proof-of-concept, a toluene solvent was employed, while in this experiment, it was used DMSO. Other enhancement was to acquire both pre-trigger and post-trigger points, which were used to produce intensity and lifetime maps, respectively. Moreover, in the pilot study, both Walsh and Block orderings were studied, since Block ordering was shown by some studies to present good reconstruction quality for low CRs [19]. With this GN_2 ventilation strategy, the goal was to sequentially ventilate, and so, reduce the amount of O_2 in the solutions, increasing the lifetime values. However, the results did not prove this. No tendency of the lifetime with the ventilation time was verified. The SPC setup was not sensitive enough to distinguish the signal variations caused by the sequential ventilation, being

only sensitive to the biomarker's concentration. Besides, the results showed that the Walsh ordering presents more consistent values than the Block ordering, since the last produces noisier maps.

5.1 Future Work

To improve these poor results, some improvements on the SPC and on the experiment design are needed. The low SNR of the phosphorescence lifetime maps could be enhanced by switching the photodiode to a more sensitive one. Also, in this study, it was assumed that as the GN_2 ventilation time increases, the amount of O_2 in the solutions would sequentially decrease. However, this may not be as straightforward as it was assumed to be. The 30 seconds ventilation time may not be suitable, not reducing the oxygen concentration on the cell as expected. Therefore, it would be useful to use an hypoxia chamber to assure that the cells have a specific percentage of oxygen, so that, it would be reliable to relate directly the amount of oxygen in the samples with the lifetime values. Furthermore, since this study has a biomedical purpose, the next step would be to replace the solution by a tissue phantom including the several pockets of Pt(II) ring-fused chlorins with different oxygen concentrations. Finally, a cell culture with different types of cells would be used to test the probe biocompatibility and the system applicability in real conditions.

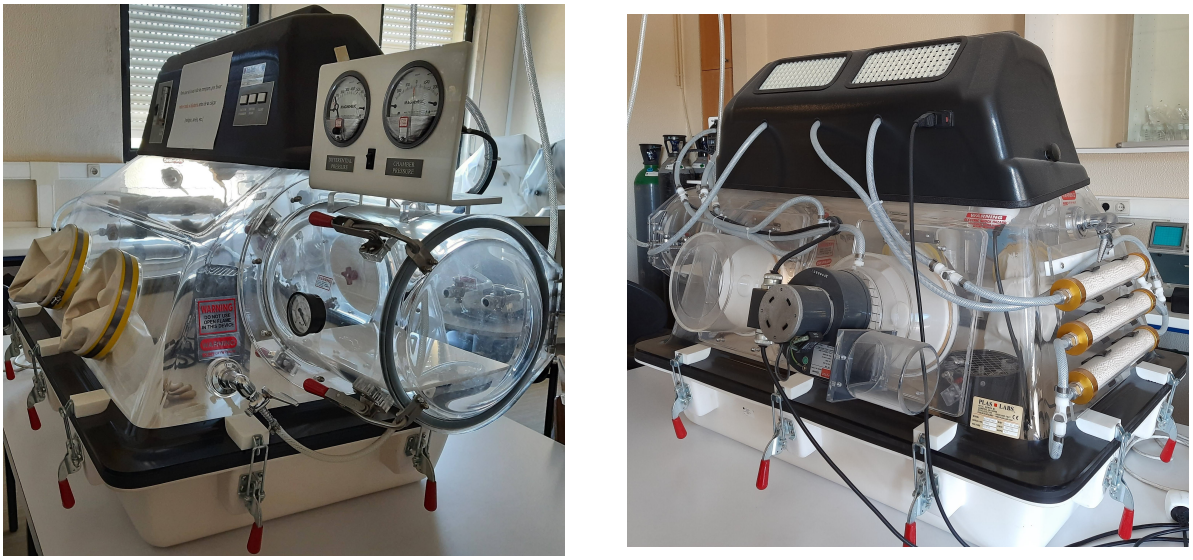

Figure 5.1: Hypoxia Chamber.

6 Bibliography

[1] Pavel S Chelushkin and Sergey P Tunik. Phosphorescence lifetime imaging (plim): State of the art and perspectives. *Progress in Photon Science*, pages 109–128, 2019.

[2] Joseph Peller, Faramarz Farahi, and Susan R Trammell. Single-pixel hyperspectral imaging for real-time cancer detection: detecting damage in ex vivo porcine tissue samples. In *Medical Imaging 2016: Digital Pathology*, volume 9791, page 97910O. International Society for Optics and Photonics, 2016.

[3] Joseph Allen Peller. *A Single-pixel Hyperspectral Imaging System for Cancer Margin Detection*. PhD thesis, The University of North Carolina at Charlotte, 2018.

[4] Marco F Duarte, Mark A Davenport, Dharmpal Takhar, Jason N Laska, Ting Sun, Kevin F Kelly, and Richard G Baraniuk. Single-pixel imaging via compressive sampling. *IEEE signal processing magazine*, 25(2):83–91, 2008.

[5] Nelson AM Pereira, Mafalda Laranjo, João Casalta-Lopes, Arménio C Serra, Marta Piñeiro, João Pina, J Sérgio Seixas de Melo, Mathias O Senge, M Filomena Botelho, Liliana Martelo, et al. Platinum (ii) ring-fused chlorins as near-infrared emitting oxygen sensors and photodynamic agents. *ACS medicinal chemistry letters*, 8(3):310–315, 2017.

[6] Matthew P Edgar, Graham M Gibson, and Miles J Padgett. Principles and prospects for single-pixel imaging. *Nature photonics*, 13(1):13–20, 2019.

[7] Wen-Kai Yu. Super sub-nyquist single-pixel imaging by means of cake-cutting hadamard basis sort. *Sensors*, 19(19):4122, 2019.

[8] Jean-Jacques Peters. A history of television. *European Broadcasting Union*, 2000.

[9] Ziheng Qiu, Zibang Zhang, Jingang Zhong, et al. Comprehensive comparison of single-pixel imaging methods. *Optics and Lasers in Engineering*, 134:106301, 2020.

[10] Jeffrey H Shapiro and Robert W Boyd. The physics of ghost imaging. *Quantum Information Processing*, 11(4):949–993, 2012.

[11] Todd B Pittman, YH Shih, DV Strekalov, and Alexander V Sergienko. Optical imaging by means of two-photon quantum entanglement. *Physical Review A*, 52(5):R3429, 1995.

[12] Alejandra Valencia, Giuliano Scarcelli, Milena D'Angelo, and Yanhua Shih. Two-photon imaging with thermal light. *Physical review letters*, 94(6):063601, 2005.

[13] Jeffrey H Shapiro. Computational ghost imaging. *Physical Review A*, 78(6):061802, 2008.

[14] Pradeep Sen, Billy Chen, Gaurav Garg, Stephen R Marschner, Mark Horowitz, Marc Levoy, and Hendrik PA Lensch. Dual photography. In *ACM SIGGRAPH 2005 Papers*, pages 745–755. 2005.

[15] David L Donoho. Compressed sensing. *IEEE Transactions on information theory*, 52(4):1289–1306, 2006.

[16] Dharmpal Takhar, Jason N Laska, Michael B Wakin, Marco F Duarte, Dror Baron, Shriram Sarvotham, Kevin F Kelly, and Richard G Baraniuk. A new compressive imaging camera architecture using optical-domain compression. In *Computational Imaging IV*, volume 6065, page 606509. International Society for Optics and Photonics, 2006.

[17] Pedro Latorre-Carmona, V Javier Traver, J Salvador Sánchez, and Enrique Tajahuerce. Online reconstruction-free single-pixel image classification. *Image and Vision Computing*, 86:28–37, 2019.

[18] Justin Romberg. Imaging via compressive sampling. *IEEE Signal Processing Magazine*, 25(2):14–20, 2008.

[19] Pedro G Vaz, Daniela Amaral, LF Requicha Ferreira, Miguel Morgado, and João Cardoso. Image quality of compressive single-pixel imaging using different hadamard orderings. *Optics express*, 28(8):11666–11681, 2020.

[20] Emmanuel J Candès and Michael B Wakin. An introduction to compressive sampling. *IEEE signal processing magazine*, 25(2):21–30, 2008.

[21] Panagiotis C Petrantonakis and Panayiota Poirazi. A compressed sensing perspective of hippocampal function. *Frontiers in systems neuroscience*, 8:141, 2014.

[22] Emmanuel J Candes. The restricted isometry property and its implications for compressed sensing. *Comptes rendus mathematique*, 346(9-10):589–592, 2008.

[23] Richard G Baraniuk. Compressive sensing [lecture notes]. *IEEE signal processing magazine*, 24(4):118–121, 2007.

[24] Kathy J Horadam. *Hadamard matrices and their applications*. Princeton university press, 2012.

[25] Cai Zhuoran, Zhao Honglin, Jia Min, Wang Gang, and Shen Jingshi. An improved hadamard measurement matrix based on walsh code for compressive sensing. In *2013 9th International Conference on Information, Communications & Signal Processing*, pages 1–4. IEEE, 2013.

[26] Ming-Jie Sun, Ling-Tong Meng, Matthew P Edgar, Miles J Padgett, and Neal Radwell. A russian dolls ordering of the hadamard basis for compressive single-pixel imaging. *Scientific reports*, 7(1):1–7, 2017.

[27] Chengbo Li. *An efficient algorithm for total variation regularization with applications to the single pixel camera and compressive sensing*. PhD thesis, 2010.

[28] Rachit Manchanda and Kanika Sharma. A review of reconstruction algorithms in compressive sensing. In *2020 International Conference on Advances in Computing, Communication & Materials (ICACCM)*, pages 322–325. IEEE, 2020.

[29] Wotao Yin Chengbo Li and Yin Zhang. TVAL3.

[30] Chengbo Li, Wotao Yin, and Yin Zhang. User's guide for tval3: Tv minimization by augmented lagrangian and alternating direction algorithms. *CAAM report*, 20(46-47):4, 2009.

[31] Edinburgh Instruments. What is the Difference between Luminescence, Photoluminescence, Fluorescence, and Phosphorescence? `https://www.edinst.com/blog/photoluminescence-differences/`. Accessed: 2021-05-10.

[32] LibreTexts Textmap. Physical chemistry for the biosciences. `https://chem.libretexts.org/@go/page/41400`, 2020. Accessed: 2021-05-10.

[33] LibreTexts Textmap. Physical and Theoretical Chemistry. `https://chem.libretexts.org/Bookshelves/Physical_and_Theoretical_Chemistry_Textbook_Maps/`

Supplemental_Modules_(Physical_and_Theoretical_Chemistry)/Electronic_Structure_of_Atoms_and_Molecules/Electronic_Configurations/Pauli_Exclusion_Principle, 2021. Accessed: 2021-06-04.

[34] LibreTexts Textmap. Physical and Theoretical Chemistry. https://chem.libretexts.org/Bookshelves/Physical_and_Theoretical_Chemistry_Textbook_Maps/Supplemental_Modules_(Physical_and_Theoretical_Chemistry)/Electronic_Structure_of_Atoms_and_Molecules/Evaluating_Spin_Multiplicity, 2021. Accessed: 2021-06-04.

[35] Gleb Baryshnikov, Boris Minaev, and Hans Ågren. Theory and calculation of the phosphorescence phenomenon. *Chemical reviews*, 117(9):6500–6537, 2017.

[36] LINDA B McGOWN and Kasem Nithipatikom. Molecular fluorescence and phosphorescence. 2000.

[37] Hiromi Kurokawa, Hidehiro Ito, Mai Inoue, Kenji Tabata, Yoshifumi Sato, Kazuya Yamagata, Shinae Kizaka-Kondoh, Tetsuya Kadonosono, Shigenobu Yano, Masahiro Inoue, et al. High resolution imaging of intracellular oxygen concentration by phosphorescence lifetime. *Scientific reports*, 5(1):1–13, 2015.

[38] LibreTexts Textmap. Physical and Theoretical Chemistry. https://chem.libretexts.org/Bookshelves/Physical_and_Theoretical_Chemistry_Textbook_Maps/Supplemental_Modules_(Physical_and_Theoretical_Chemistry)/Spectroscopy/Electronic_Spectroscopy/Fluorescence_and_Phosphorescence, 2021. Accessed: 2021-06-04.

[39] Yessenia Jauregui-Sánchez, Pere Clemente, Jesús Lancis, and Enrique Tajahuerce. Single-pixel imaging with fourier filtering: application to vision through scattering media. *Optics letters*, 44(3):679–682, 2019.

[40] Kobra Soltanlou and Hamid Latifi. Three-dimensional imaging through scattering media using a single pixel detector. *Applied optics*, 58(28):7716–7726, 2019.

[41] Ming-Jie Sun and Jia-Min Zhang. Single-pixel imaging and its application in three-dimensional reconstruction: a brief review. *Sensors*, 19(3):732, 2019.

[42] Matthew P Edgar, Graham M Gibson, Richard W Bowman, Baoqing Sun, Neal Radwell, Kevin J Mitchell, Stephen S Welsh, and Miles J Padgett. Simultaneous real-time visible and infrared video with single-pixel detectors. *Scientific reports*, 5(1):1–8, 2015.

[43] Rayko Ivanov Stantchev, Xiao Yu, Thierry Blu, and Emma Pickwell-MacPherson. Real-time terahertz imaging with a single-pixel detector. *Nature communications*, 11(1):1–8, 2020.

[44] Yu-Hang He, Ai-Xin Zhang, Ming-Fei Li, Yi-Yi Huang, Bao-Gang Quan, Da-Zhang Li, Ling-An Wu, and Li-Ming Chen. High-resolution sub-sampling incoherent x-ray imaging with a single-pixel detector. *APL Photonics*, 5(5):056102, 2020.

[45] Qi Pian, Ruoyang Yao, and Xavier Intes. Time-resolved hyperspectral single-pixel camera implementation for compressive wide-field fluorescence lifetime imaging. In *Multimodal Biomedical Imaging XI*, volume 9701, page 970115. International Society for Optics and Photonics, 2016.

[46] Florian Stuker, Jorge Ripoll, and Markus Rudin. Fluorescence molecular tomography: principles and potential for pharmaceutical research. *Pharmaceutics*, 3(2):229–274, 2011.

[47] HE Kaiser. Functional comparative histology. 5. communication: History of histology. *Gegenbaurs morphologisches Jahrbuch*, 131(6):815–862, 1985.

[48] Gianmaria Calisesi, Michele Castriotta, Alessia Candeo, Anna Pistocchi, Cosimo D'Andrea, Gianluca Valentini, Andrea Farina, and Andrea Bassi. Spatially modulated illumination allows for light sheet fluorescence microscopy with an incoherent source and compressive sensing. *Biomedical optics express*, 10(11):5776–5788, 2019.

[49] Andor. An overview of SPIM - Selective Plane Illumination Microscopy. `https://andor.oxinst.com/learning/view/article/spim-selective-plane-illumination-microscopy`, note = Accessed: 06-06-2021.

[50] Vasilis Ntziachristos. Fluorescence molecular imaging. *Annu. Rev. Biomed. Eng.*, 8:1–33, 2006.

[51] Yang Liu, Jinli Suo, Yuanlong Zhang, and Qionghai Dai. Single-pixel phase and fluorescence microscope. *Optics express*, 26(25):32451–32462, 2018.

[52] The Royal College of Pathologists. What is a biopsy? Accessed: 12-02-2021.

[53] Chaitanya K Mididoddi and Michael R Hughes. Towards high speed needle microscopy through a multimode fiber by single pixel imaging. In *Endoscopic Microscopy XIV*, volume 10854, page 1085417. International Society for Optics and Photonics, 2019.

[54] Kan Wang, Qun Wang, Qingming Luo, and Xiaoquan Yang. Fluorescence molecular tomography in the second near-infrared window. *Optics express*, 23(10):12669–12679, 2015.

[55] Andrea Farina, M Lepore, Laura Di Sieno, Alberto Dalla Mora, Nicolas Ducros, A Pifferi, Gianluca Valentini, Simon R Arridge, and Cosimo D'Andrea. Diffuse optical tomography by using time-resolved single pixel camera. In *Optical Tomography and Spectroscopy of Tissue XI*, volume 9319, page 93191K. International Society for Optics and Photonics, 2015.

[56] Ruoyang Yao, Qi Pian, and Xavier Intes. Wide-field fluorescence molecular tomography with compressive sensing based preconditioning. *Biomedical optics express*, 6(12):4887–4898, 2015.

[57] Kohki Okabe, Noriko Inada, Chie Gota, Yoshie Harada, Takashi Funatsu, and Seiichi Uchiyama. Intracellular temperature mapping with a fluorescent polymeric thermometer and fluorescence lifetime imaging microscopy. *Nature communications*, 3(1):1–9, 2012.

[58] Rozhin Penjweini, Alessio Andreoni, Tilman Rosales, Jeonghan Kim, Michael D Brenner, Dan L Sackett, Jay H Chung, and Jay R Knutson. Intracellular oxygen mapping using a myoglobin-mcherry probe with fluorescence lifetime imaging. *Journal of biomedical optics*, 23(10):107001, 2018.

[59] Angel Orte, Jose M Alvarez-Pez, and Maria J Ruedas-Rama. Fluorescence lifetime imaging microscopy for the detection of intracellular ph with quantum dot nanosensors. *ACS nano*, 7(7):6387–6395, 2013.

[60] Wolfgang Becker. Fluorescence lifetime imaging–techniques and applications. *Journal of microscopy*, 247(2):119–136, 2012.

[61] Olympus. Fluorescence Resonance Energy Transfer (FRET) Microscopy. `https://www.olympus-lifescience.com/pt/microscope-resource/primer/techniques/fluorescence/fret/fretintro/`, note = Accessed: 04-04-2021.

[62] Applications Department BioTek Instruments Paul Held, Ph.D. An overview of SPIM - Selective Plane Illumination Microscopy. https://www.biotek.com/resources/white-papers/an-introduction-to-fluorescence-resonance-energy-transfer-fret-technology-and-its note = Accessed: 04-04-2021.

[63] Edmund Optics. Hyperspectral and multispectral imaging. https://www.edmundoptics.com/knowledge-center/application-notes/imaging/hyperspectral-and-multispectral-imaging. Accessed: 04-06-2021.

[64] Richard M Levenson and James R Mansfield. Multispectral imaging in biology and medicine: slices of life. *Cytometry Part A: the journal of the International Society for Analytical Cytology*, 69(8):748–758, 2006.

[65] Yamin Song, Fuhong Cai, Julian Evans, Erik Forsberg, and Sailing He. Compressive sampling multispectral imaging and unmixing method for fluorescent imaging. *Progress In Electromagnetics Research*, 46:135–142, 2016.

[66] Florian Rousset, Nicolas Ducros, Françoise Peyrin, Gianluca Valentini, Cosimo D'andrea, and Andrea Farina. Time-resolved multispectral imaging based on an adaptive single-pixel camera. *Optics express*, 26(8):10550–10558, 2018.

[67] Florian Rousset, Nicolas Ducros, Andrea Farina, Gianluca Valentini, Cosimo d'Andrea, and Françoise Peyrin. Time-resolved wavelet-based acquisitions using a single-pixel camera. In *Three-Dimensional and Multidimensional Microscopy: Image Acquisition and Processing XXIV*, volume 10070, page 1007016. International Society for Optics and Photonics, 2017.

[68] Florian Rousset, Nicolas Ducros, Andrea Farina, Gianluca Valentini, Cosimo D'Andrea, and Françoise Peyrin. Adaptive basis scan by wavelet prediction for single-pixel imaging. *IEEE Transactions on Computational Imaging*, 3(1):36–46, 2016.

[69] Karolina Jahn, Volker Buschmann, and Carsten Hille. Simultaneous fluorescence and phosphorescence lifetime imaging microscopy in living cells. *Scientific reports*, 5(1):1–13, 2015.

[70] VI Shcheslavskiy, A Neubauer, R Bukowiecki, F Dinter, and Wolfgang Becker. Combined fluorescence and phosphorescence lifetime imaging. *Applied Physics Letters*, 108(9):091111, 2016.

[71] Kenneth Yin Zhang, Qi Yu, Huanjie Wei, Shujuan Liu, Qiang Zhao, and Wei Huang. Long-lived emissive probes for time-resolved photoluminescence bioimaging and biosensing. *Chemical reviews*, 118(4):1770–1839, 2018.

[72] Texas Instruments. TI DLP® LightCrafter™ 4500 Evaluation Module User's Guide. https://www.ti.com/lit/ug/dlpu011f/dlpu011f.pdf, 2017. Accessed: 06-07-2021.

[73] Zibang Zhang, Xueying Wang, Guoan Zheng, and Jingang Zhong. Hadamard single-pixel imaging versus fourier single-pixel imaging. *Optics Express*, 25(16):19619–19639, 2017.

[74] Texas Instruments. Adjustable Gain Avalanche Photodetectors APD410x Operation Manual. https://www.thorlabs.com/drawings/8721461480cb10f-04B59D90-9661-FECA-3F66B5058EA83E2A/APD410A_M-Manual.pdf, 2020. Accessed: 06-07-2021.

[75] Edmund Optics. 769nm CWL, 25mm Dia, 41nm Bandwidth, OD 6 Fluorescence Filter. https://www.edmundoptics.com/p/769nm-cwl-25mm-dia-41nm-bandwidth-od-6-fluorescence-filter/27213/. Accessed: 06-07-2021.

[76] Alexander Tomlinson. pycrafter4500. : https://pypi.org/project/pycrafter4500/.

[77] National Instruments. DEVICE SPECIFICATIONS. https://www.ni.com/pdf/manuals/374650c.pdf, 2016. Accessed: 06-07-2021.

[78] Digilent. Analog Discovery 2™ Reference Manual. http://www.farnell.com/datasheets/2702629.pdf, 2015. Accessed: 06-07-2021.

[79] Kosuke Kuroda, Tetsuo Komori, Kojiro Ishibashi, Takuya Uto, Isao Kobayashi, Riki Kadokawa, Yui Kato, Kazuaki Ninomiya, Kenji Takahashi, and Eishu Hirata. Non-aqueous, zwitterionic solvent as an alternative for dimethyl sulfoxide in the life sciences. *Communications Chemistry*, 3(1):1–7, 2020.

[80] Razel Scientific Instruments. Razel r99-e syringe pump user's manual. https://conquerscientific.com/wp-content/product-images/2014/02/Razel-R99-E.pdf, 2017. Accessed: 06-07-2021.

A Appendix

A.1 TVAL3

To solve the objective function defined 2.13, the function is separated into two subproblems:

1. **w-subproblem:**

   The minimization problem considering only the minimization of w_i is formulated by:

$$\min_{w_i} = \sum_i (\|w_i\| - \mu_i^T (D_i x_k - w_i) + \frac{\beta_i}{2} \|D_i x_k - w_{i2}^2) \tag{A.1}$$

   This subproblem can be solved by employing:

$$w_{i,k+1} = \max\{\|D_i x_k - \frac{\nu_i}{\beta_i}\| - \frac{1}{\beta}, 0\} \frac{(D_i x_k - \nu_i/\beta_i)}{\|D_i x_k - \nu_i/\beta_i\|}, \tag{A.2}$$

   that devolves a closed form solution, where $0 \bullet (0/0) = 0$ and $\|.\|$ is the 2-norm. The overall equations used to minimized w_i are the "shrinkage-like formulas", that is shorten for "skrike":

$$w_{i,k+1} = shrike(D_i x_k; \nu_i, \beta_i) \tag{A.3}$$

2. **x-subproblem:**

   The x-subproblem is formulated by:

$$\min_x \mathbf{Q}_k(x) \triangleq \sum_i (-\nu_i^T (D_i x - w_{i,k+1}) + \frac{\beta_i}{2} \|D_i x - w_{i,k+1}\|_2^2) - \lambda^T (\Phi x - b) + \frac{\mu}{2} \|\Phi x - b_2^2\| \tag{A.4}$$

   where $\mathbf{Q}_k(x)$ is a quadratic function.

   x-subproblem is solved by one-step steepest descent method iteratively applying:

$$\tilde{x} = x_k - \alpha d \tag{A.5}$$

where d is the gradient direction:

$$d_k(x) = \sum_i (\beta_i D_i^T(-D_i x - w_{i,k+1}) - D_i T \mu_i) + \nu \Phi^T(\Phi x - b) - \Phi^T \lambda \tag{A.6}$$

To obtain α, it is used the Barzilai and Borwein (BB):

$$\alpha = \frac{s_k^T s_k}{s_k^T y_k} \text{ or } \alpha = \frac{s_k^T y_k}{y_k^T y_k}, \tag{A.7}$$

that is validated by nonmonotone line search algorithm.

A.2 Results

Figures A.1, A.2, A.3 and A.4 show the phosphorescence intensity and lifetime maps, obtained with 10% compression ratio, for both Walsh and block orderings, with D1 positioned on the left side of the holder and D3 on the right.

Figures A.5, A.6, A.7 and A.8 show the phosphorescence intensity and lifetime maps, obtained with 10% compression ratio, for both Walsh and block orderings, with D3 positioned on the left side of the holder and D1 on the right.

Tables A.1, A.2, A.3 and A.4 show the results for D1 and D3 on both sides of the holder and for both orderings and CRs, when the left and the right position sample was ventilated individually.

Tables A.5, A.6, A.7, A.8, A.9 and A.10 show the mean phosphorescence intensity and lifetime and their standard deviations of D1 and D2 solutions on both positions on the holder.

Tables A.11, A.12, A.13, A.14, A.15 and A.16 show the results for D2 and D3 on both side of the holder and for both orderings and CRs.

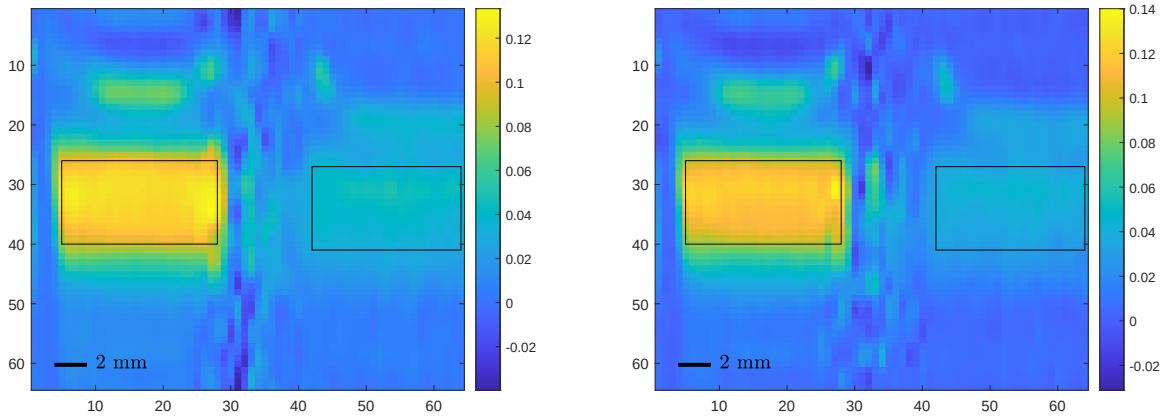

(a) 0 sec

(b) 150 sec

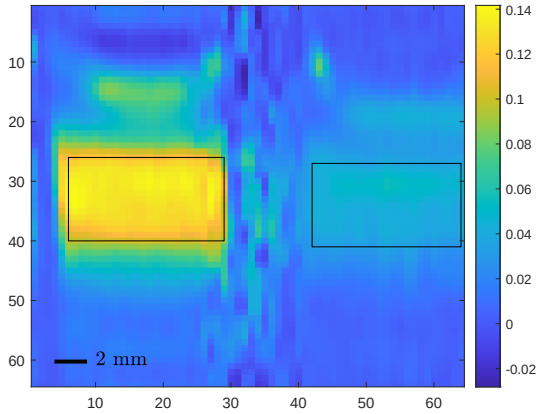

(c) 0 sec

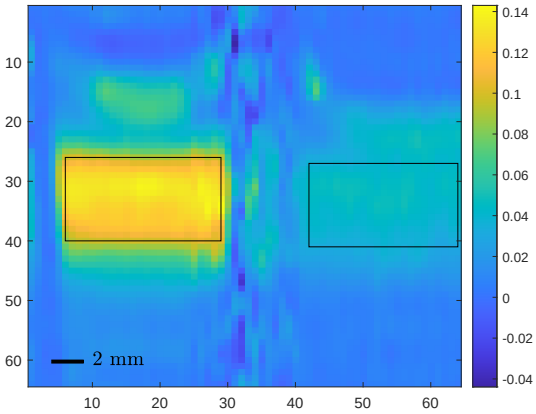

(d) 150 sec

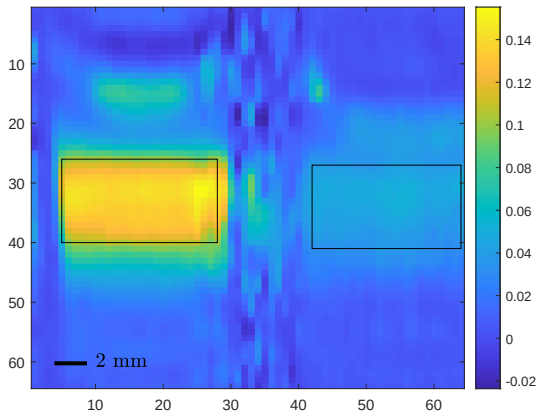

(e) 0 sec

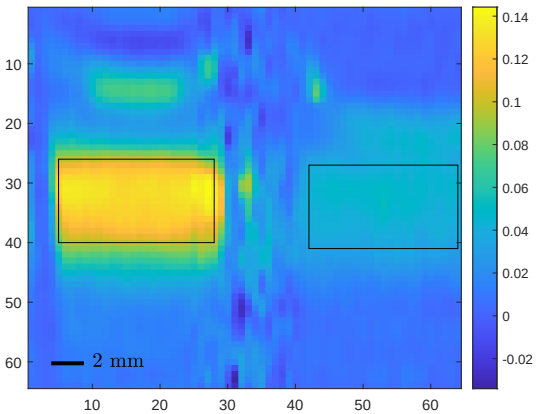

(f) 150 sec

Figure A.1: Walsh ordering phosphorescence intensity maps obtained with 10% compression ratio, with the D1 on the left side of the holder and D3 on the right. The first row shows the maps for 0 and 150 seconds GN_2 ventilation times, with the left sided sample ventilated, the second with both and the third with the right sided.

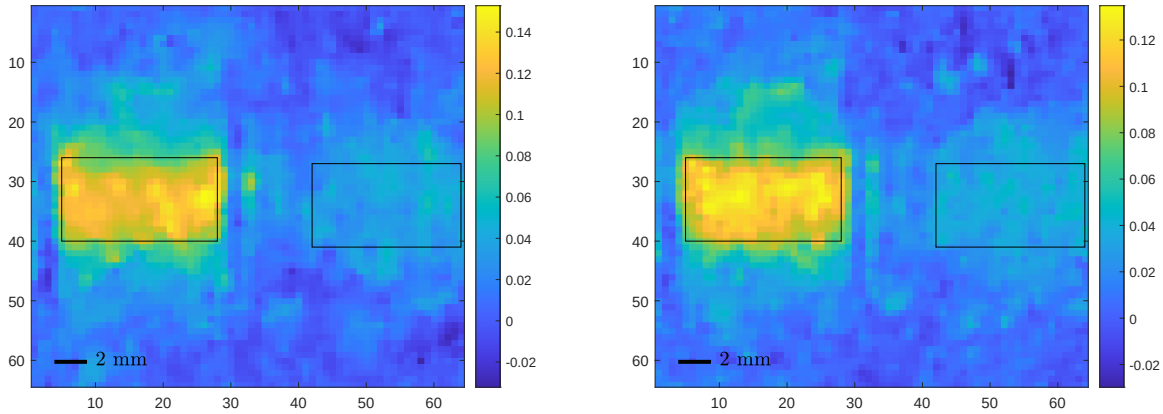

(a) 0 sec

(b) 150 sec

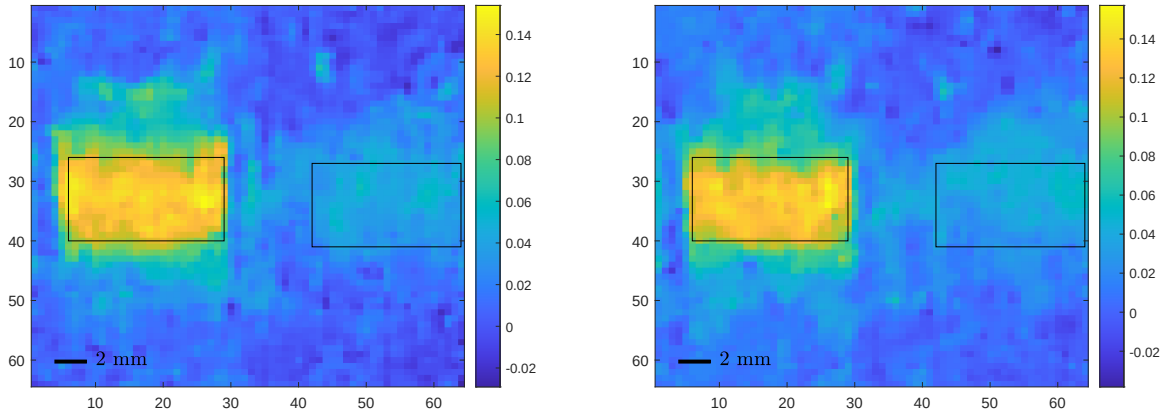

(c) 0 sec

(d) 150 sec

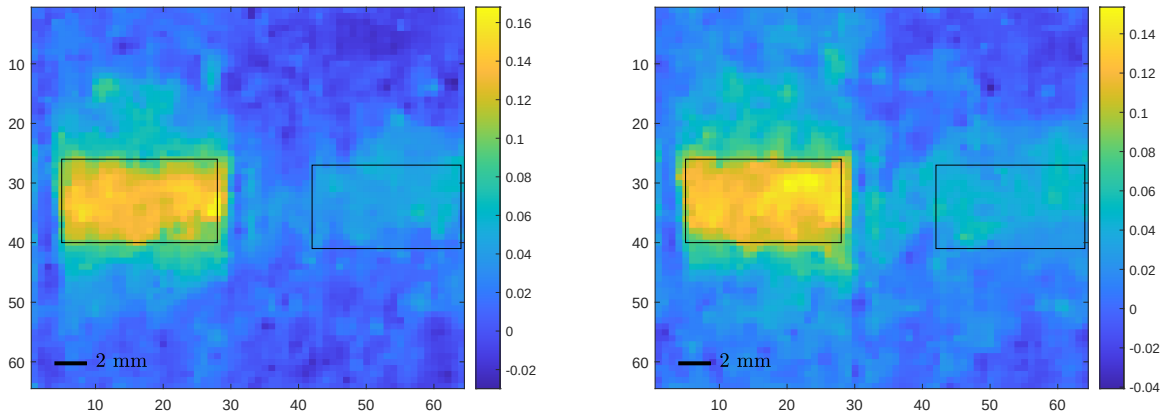

(e) 0 sec

(f) 150 sec

Figure A.2: Block ordering phosphorescence intensity maps obtained with 10% compression ratio, with the D1 on the left side of the holder and D3 on the right. The first row shows the maps for 0 and 150 seconds GN_2 ventilation times, with the left sided sample ventilated, the second with both and the third with the right sided.

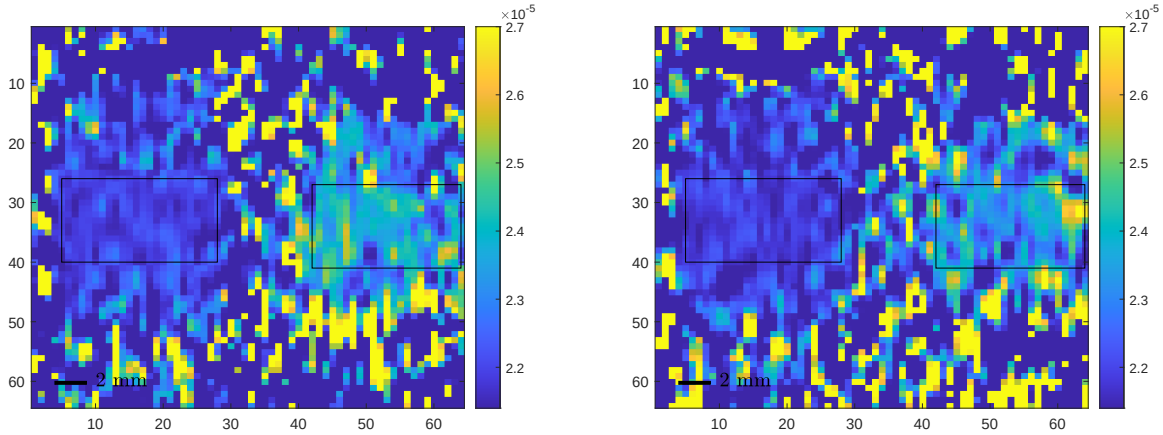

(a) 0 sec

(b) 150 sec

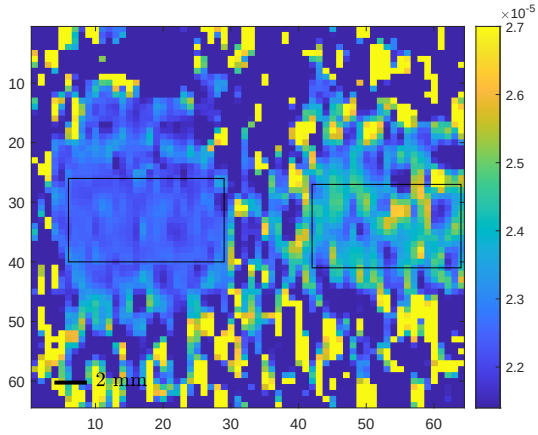

(c) 0 sec

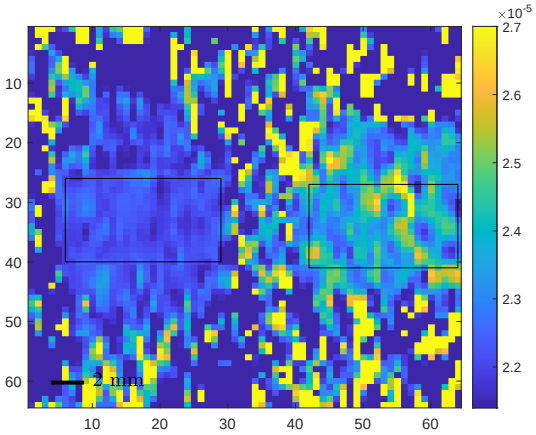

(d) 150 sec

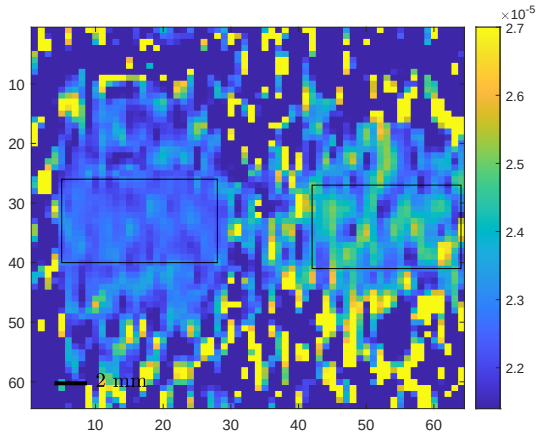

(e) 0 sec

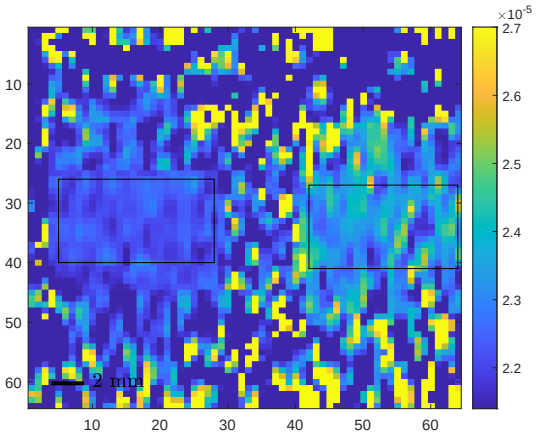

(f) 150 sec

Figure A.3: Walsh ordering phosphorescence lifetime maps obtained with 10% compression ratio, with the D1 on the left side of the holder and D3 on the right. The first row shows the maps for 0 and 150 seconds NG_2 ventilation times, with the left sided sample ventilated, the second with both and the third with the right sided.

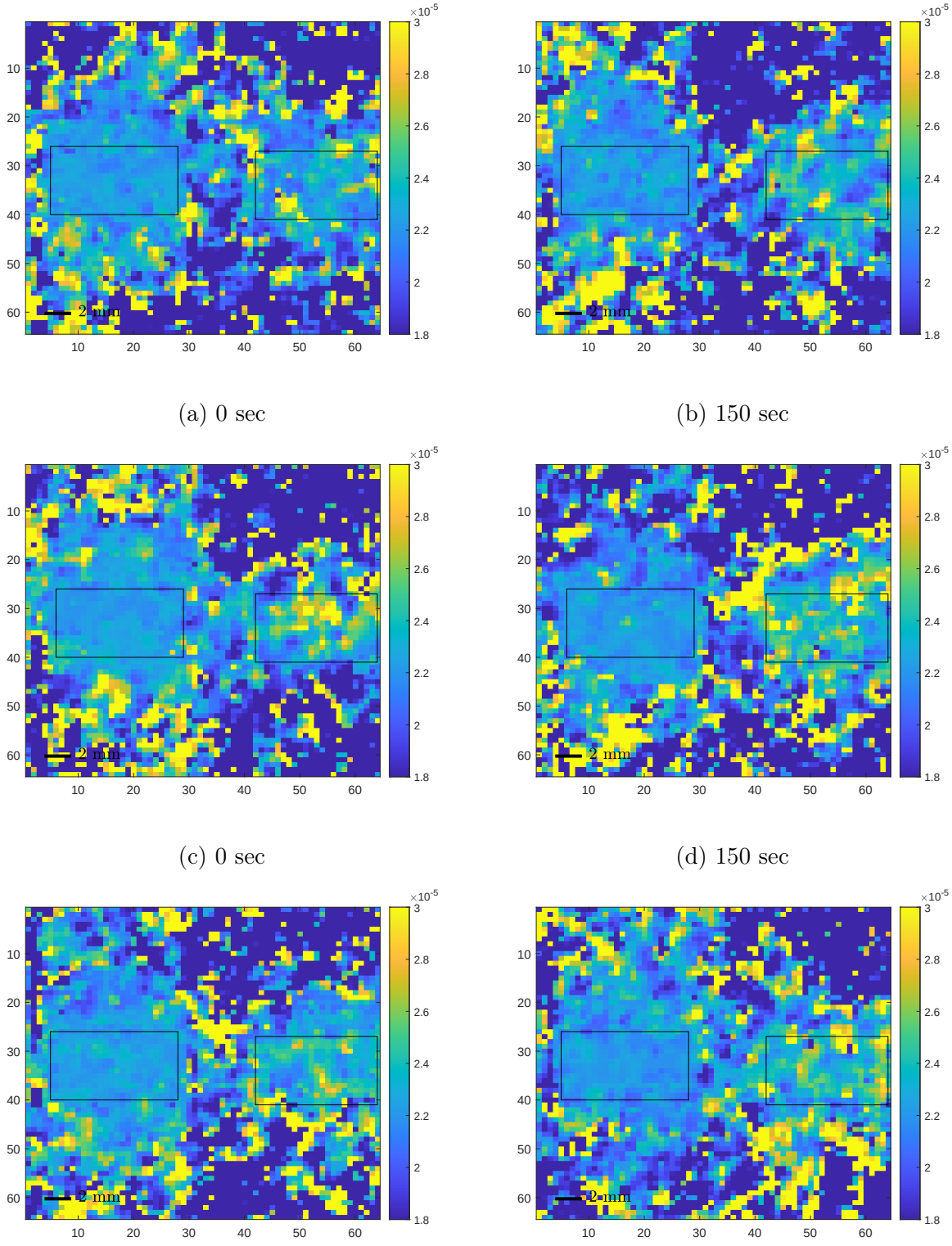

(a) 0 sec

(b) 150 sec

(c) 0 sec

(d) 150 sec

(e) 0 sec

(f) 150 sec

Figure A.4: Block ordering phosphorescence lifetime maps obtained with 10% compression ratio, with the D1 on the left side of the holder and D3 on the right. The first row shows the maps for 0 and 150 seconds NG_2 ventilation times, with the left sided sample ventilated, the second with both and the third with the right sided.

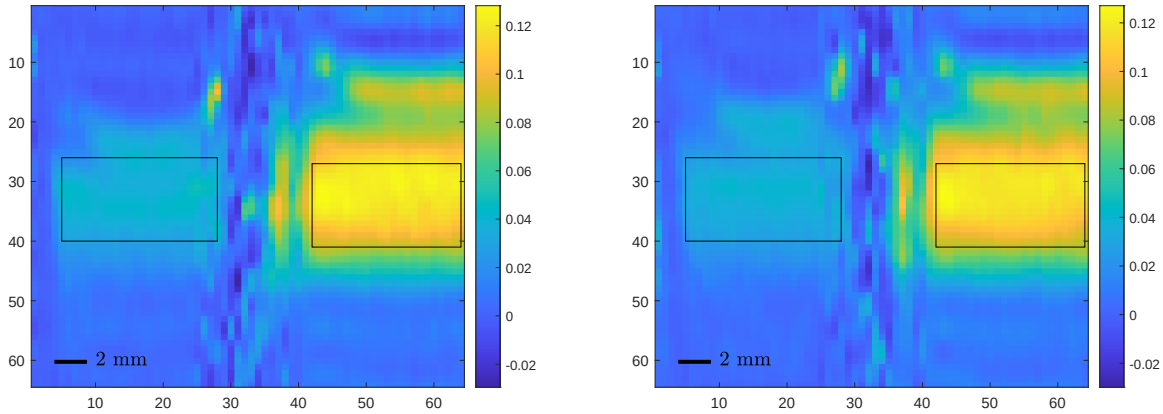

(a) 0 sec

(b) 150 sec

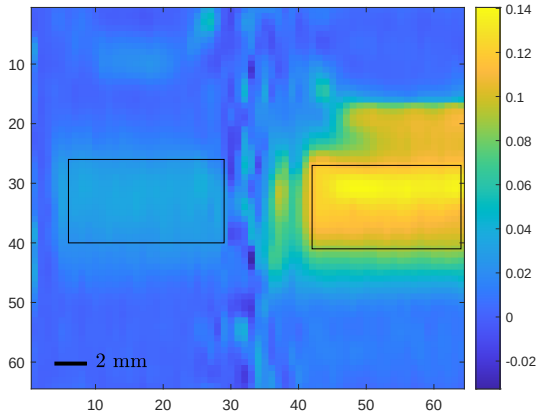

(c) 0 sec

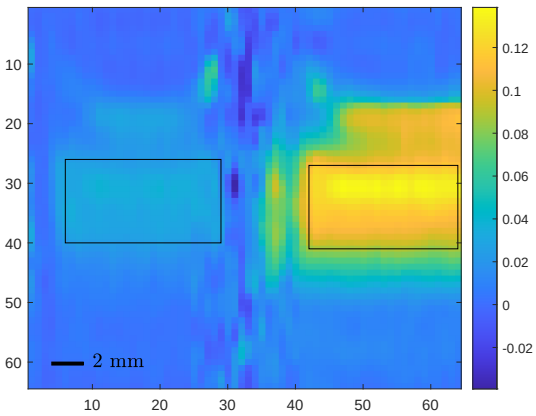

(d) 150 sec

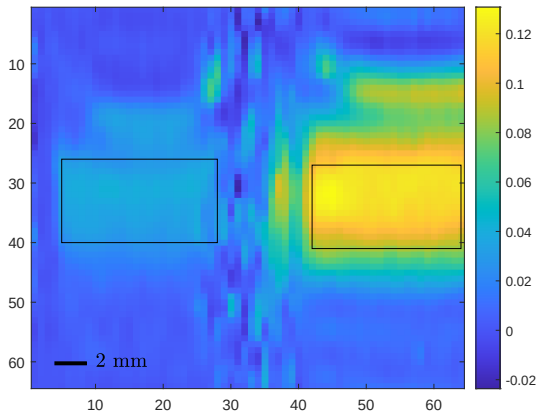

(e) 0 sec

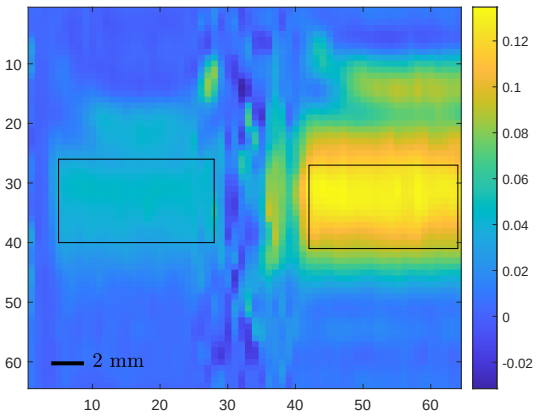

(f) 150 sec

Figure A.5: Walsh ordering phosphorescence intensity maps obtained with 10% compression ratio, with the D3 on the left side of the holder and D1 on the right. The first row shows the maps for 0 and 150 seconds GN_2 ventilation times, with the left sided sample ventilated, the second with both and the third with the right sided.

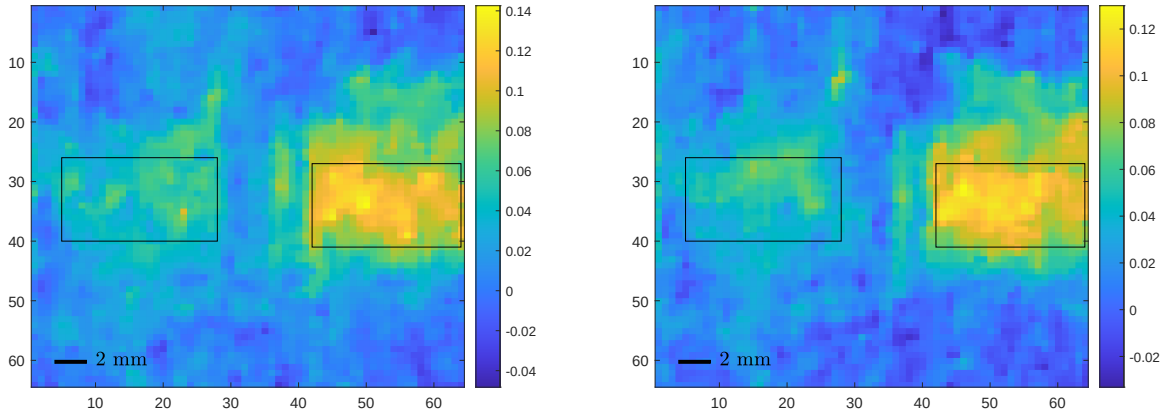

(a) 0 sec

(b) 150 sec

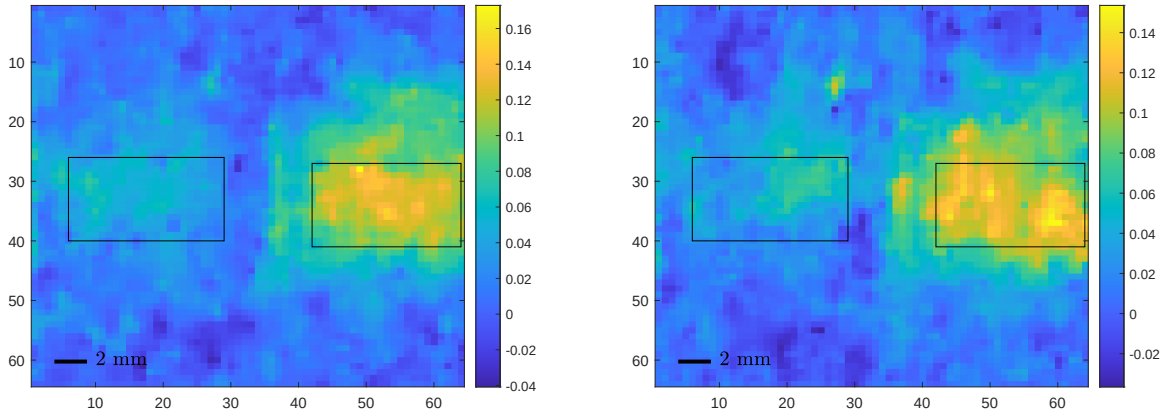

(c) 0 sec

(d) 150 sec

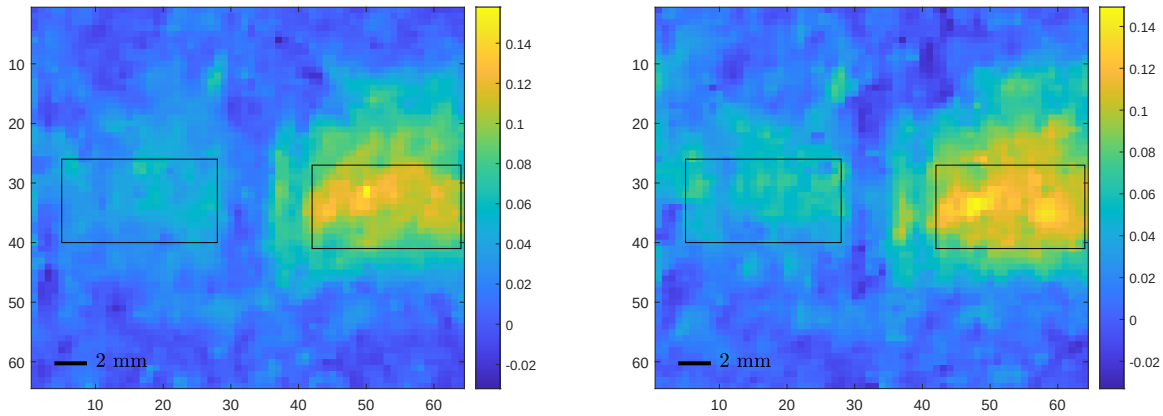

(e) 0 sec

(f) 150 sec

Figure A.6: Block ordering phosphorescence intensity maps obtained with 10% compression ratio, with the D3 on the left side of the holder and D1 on the right. The first row shows the maps for 0 and 150 seconds GN_2 ventilation times, with the left sided sample ventilated, the second with both and the third with the right sided.

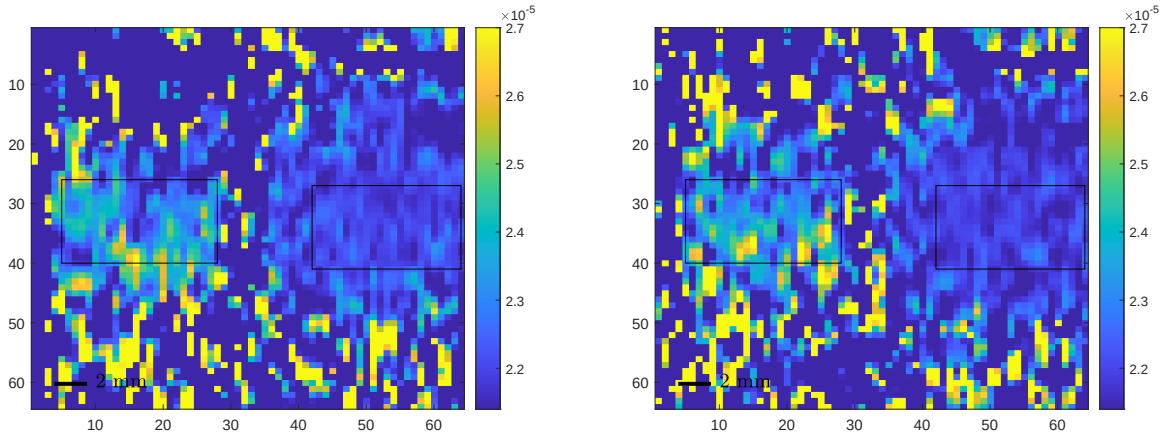

(a) 0 sec

(b) 150 sec

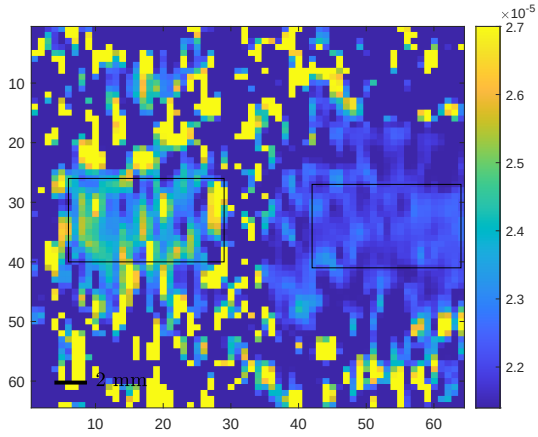

(c) 0 sec

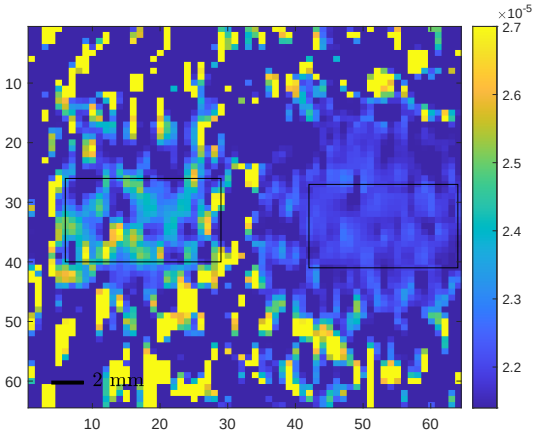

(d) 150 sec

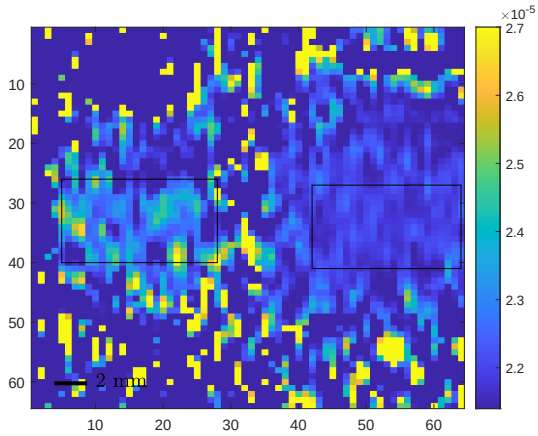

(e) 0 sec

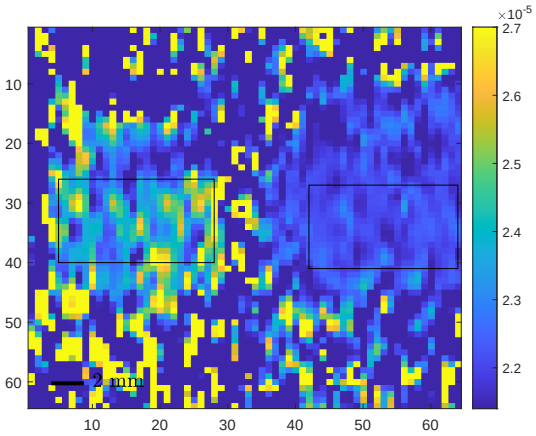

(f) 150 sec

Figure A.7: Walsh ordering phosphorescence lifetime maps obtained with 10% compression ratio, with the D3 on the left side of the holder and D1 on the right. The first row shows the maps for 0 and 150 seconds GN_2 ventilation times, with the left sided sample ventilated, the second with both and the third with the right sided.

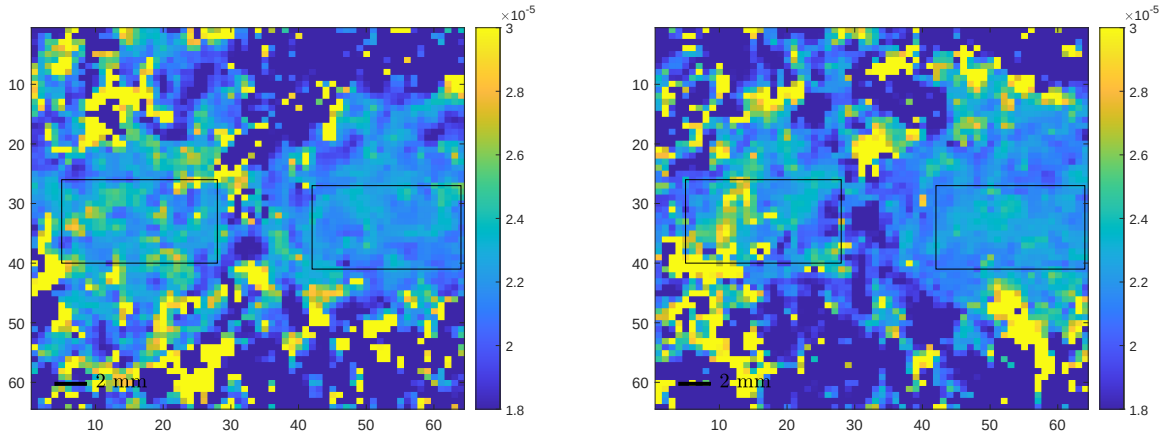

(a) 0 sec

(b) 150 sec

(c) 0 sec

(d) 150 sec

(e) 0 sec

(f) 150 sec

Figure A.8: Block ordering phosphorescence lifetime maps obtained with 10% compression ratio, with the D3 on the left side of the holder and D1 on the right. The first row shows the maps for 0 and 150 seconds GN_2 ventilation times, with the left sided sample ventilated, the second with both and the third with the right sided.

Table A.1: Mean phosphorescence lifetime and intensity values and their corresponding values for the GN_2 ventilation times of 0, 30, 60, 90, 120, 150 seconds and for 10% and 5% compression ratios. D1 was GN_2 ventilated, while the D3 was not.

	sec	CR	**D1**				D3			
			$\overline{\tau}(\mu s)$	$\sigma_{\overline{\tau}}(\mu s)$	$\overline{I}$	$\sigma_{\overline{I}}$	$\overline{\tau}(\mu s)$	$\sigma_{\overline{\tau}}(\mu s)$	$\overline{I}$	$\sigma_{\overline{I}}$
Walsh	0	10%	21.95	0.3	0.1125	0.01	23.65	1.1	0.0383	0.005
		5%	21.94	0.2	0.1131	0.014	23.63	0.7	0.0374	0.004
	30	10%	21.92	0.3	0.1114	0.011	23.77	1.1	0.0385	0.005
		5%	21.92	0.3	0.1118	0.013	23.74	0.8	0.0376	0.004
	60	10%	21.95	0.3	0.1118	0.011	23.47	1	0.0381	0.004
		5%	21.96	0.2	0.112	0.013	23.52	1.3	0.0373	0.004
	90	10%	21.9	0.3	0.1106	0.01	23.79	1.3	0.0378	0.004
		5%	21.89	0.2	0.1108	0.013	23.67	0.8	0.037	0.004
	120	10%	21.85	0.3	0.11	0.01	23.45	0.9	0.0373	0.004
		5%	21.85	0.3	0.1103	0.014	23.46	0.7	0.0366	0.004
	150	10%	21.87	0.4	0.11	0.01	23.34	1.2	0.0375	0.005
		5%	21.87	0.3	0.1102	0.013	23.28	0.7	0.0368	0.004
Block	0	10%	22.35	0.7	0.1129	0.016	18.29	116.9	0.0359	0.008
		5%	22.67	0.8	0.1118	0.014	22.52	2.6	0.0381	0.009
	30	10%	22.11	0.9	0.1134	0.016	25.73	18.4	0.0322	0.009
		5%	22.16	0.5	0.1155	0.015	25.19	23.2	0.0313	0.008
	60	10%	21.97	0.7	0.1122	0.013	25.84	8	0.0337	0.008
		5%	21.87	0.6	0.1145	0.012	21.16	58.1	0.0321	0.009
	90	10%	21.93	0.7	0.1103	0.012	27.94	30.7	0.0331	0.01
		5%	22.13	0.6	0.1087	0.011	23.72	12.4	0.0351	0.008
	120	10%	21.97	0.7	0.1102	0.013	23.35	2.7	0.0345	0.009
		5%	22.47	0.8	0.1139	0.012	23.89	30.7	0.0331	0.01
	150	10%	22.27	0.8	0.1063	0.016	23.26	2.8	0.0352	0.006
		5%	22.22	0.8	0.1046	0.013	22.73	1.6	0.0358	0.008

Table A.2: Mean phosphorescence lifetime and intensity values and their corresponding values for the GN_2 ventilation times of 0, 30, 60, 90, 120, 150 seconds and for 10% and 5% compression ratios. D3 was GN_2 ventilated, while D1 was not.

	sec	CR	D1				**D3**			
			$\overline{\tau}(\mu s)$	$\sigma_{\overline{\tau}}(\mu s)$	$\overline{I}$	$\sigma_{\overline{I}}$	$\overline{\tau}(\mu s)$	$\sigma_{\overline{\tau}}(\mu s)$	$\overline{I}$	$\sigma_{\overline{I}}$
Walsh	0	10%	22.53	0.3	0.1263	0.016	23.66	1.1	0.0427	0.005
		5%	22.52	0.3	0.1263	0.018	23.64	0.8	0.042	0.005
	30	10%	22.28	0.3	0.1216	0.014	23.45	1	0.0427	0.005
		5%	22.28	0.2	0.1219	0.017	23.42	0.7	0.0421	0.004
	60	10%	22.22	0.3	0.1212	0.013	23.57	1.1	0.0414	0.005
		5%	22.22	0.2	0.1216	0.017	23.52	0.7	0.0408	0.004
	90	10%	22.18	0.3	0.1209	0.013	23.38	0.9	0.0418	0.005
		5%	22.18	0.2	0.1211	0.016	23.37	0.8	0.0412	0.004
	120	10%	22.1	0.3	0.1202	0.013	23.48	1	0.0417	0.005
		5%	22.08	0.3	0.1205	0.016	23.5	0.7	0.0411	0.005
	150	10%	22.23	0.3	0.1191	0.013	23.4	0.9	0.0418	0.004
		5%	22.23	0.3	0.1193	0.016	23.39	0.8	0.0414	0.004
Block	0	10%	22.49	0.7	0.123	0.018	23.95	4.3	0.04	0.012
		5%	22.5	0.6	0.1246	0.015	19.12	145.6	0.0378	0.012
	30	10%	22.35	0.8	0.1225	0.018	24.36	6.3	0.0404	0.01
		5%	22.18	0.8	0.1215	0.015	24.94	13.5	0.0421	0.011
	60	10%	22.45	1	0.1207	0.017	8.25	435.4	0.0378	0.01
		5%	22.5	0.9	0.1197	0.015	23.63	1.8	0.0402	0.01
	90	10%	22.51	1	0.1204	0.017	24.44	7	0.0369	0.01
		5%	22.36	0.9	0.1172	0.016	24.26	5.5	0.041	0.011
	120	10%	22.5	1	0.1233	0.017	16.99	116.1	0.0373	0.009
		5%	22.38	0.6	0.1216	0.016	22.88	6.7	0.0378	0.008
	150	10%	22.04	0.7	0.1181	0.017	25.29	17	0.0378	0.01
		5%	22.36	0.6	0.1217	0.016	23.55	6.6	0.0346	0.011

Table A.3: Mean phosphorescence lifetime and intensity values and their corresponding values for the GN_2 ventilation times of 0, 30, 60, 90, 120, 150 seconds and for 10% and 5% compression ratios. D3 was GN_2 ventilated, while D1 was not.

	sec	CR	**D3**				D1			
			$\overline{\tau}(\mu s)$	$\sigma_{\overline{\tau}}(\mu s)$	$\overline{I}$	$\sigma_{\overline{I}}$	$\overline{\tau}(\mu s)$	$\sigma_{\overline{\tau}}(\mu s)$	$\overline{I}$	$\sigma_{\overline{I}}$
Walsh	0	10%	23.22	1.3	0.0365	0.005	22.04	0.3	0.1133	0.012
		5%	23.19	1.1	0.0365	0.004	22.05	0.2	0.1137	0.013
	30	10%	23.34	1.2	0.0352	0.004	21.97	0.3	0.1116	0.012
		5%	23.3	0.8	0.035	0.004	21.98	0.3	0.1121	0.013
	60	10%	23.23	1.6	0.0349	0.005	21.88	0.3	0.1103	0.011
		5%	23.16	0.9	0.0347	0.004	21.89	0.3	0.1108	0.012
	90	10%	23.33	1.3	0.0346	0.005	21.83	0.3	0.1099	0.011
		5%	23.29	0.9	0.0343	0.004	21.85	0.2	0.1104	0.012
	120	10%	24.77	15	0.0333	0.004	21.82	0.3	0.1097	0.011
		5%	23.44	1	0.0332	0.004	21.85	0.2	0.1101	0.012
	150	10%	23.32	1.5	0.033	0.004	21.91	0.3	0.1097	0.011
		5%	23.31	1.1	0.0328	0.005	21.94	0.2	0.11	0.012
Block	0	10%	23.3	3.4	0.0479	0.013	22.1	1.1	0.1003	0.016
		5%	22.69	1.1	0.0662	0.014	22.11	0.7	0.0795	0.015
	30	10%	23.01	2	0.0465	0.011	22.12	1	0.0983	0.015
		5%	23.38	1.2	0.0601	0.012	21.71	0.9	0.0817	0.016
	60	10%	21.61	190.4	0.0423	0.013	21.62	0.8	0.1005	0.013
		5%	24.74	14	0.0506	0.011	21.68	0.6	0.0897	0.015
	90	10%	23.62	11.5	0.0429	0.013	21.73	1	0.0991	0.012
		5%	22.76	1.9	0.0529	0.015	21.88	0.7	0.0841	0.013
	120	10%	24.42	4.7	0.052	0.013	22.06	0.8	0.1036	0.015
		5%	23.99	1.8	0.065	0.013	21.91	1.1	0.0853	0.014
	150	10%	14.99	171.5	0.0458	0.013	22.26	0.9	0.0975	0.014
		5%	23.86	4.2	0.0522	0.012	22	1.1	0.0869	0.012

Table A.4: Mean phosphorescence lifetime and intensity values and their corresponding values for the GN_2 ventilation times of 0, 30, 60, 90, 120, 150 seconds and for 10% and 5% compression ratios. D1 was GN_2 ventilated, while D3 was not.

	sec	CR	D3				**D1**			
			$\overline{\tau}(\mu s)$	$\sigma_{\overline{\tau}}(\mu s)$	$\overline{I}$	$\sigma_{\overline{I}}$	$\overline{\tau}(\mu s)$	$\sigma_{\overline{\tau}}(\mu s)$	$\overline{I}$	$\sigma_{\overline{I}}$
Walsh	0	10%	23	4.7	0.0334	0.005	21.95	0.3	0.1122	0.012
		5%	24.45	23.7	0.0331	0.005	21.96	0.2	0.1126	0.013
	30	10%	22.98	1.5	0.0324	0.005	21.88	0.3	0.1099	0.013
		5%	22.92	0.8	0.0322	0.005	21.88	0.2	0.1098	0.012
	60	10%	23.37	2.4	0.033	0.005	21.82	0.3	0.1083	0.012
		5%	23.19	1	0.0328	0.004	21.83	0.3	0.1084	0.012
	90	10%	23.44	1.4	0.0326	0.005	21.82	0.3	0.1073	0.013
		5%	23.46	1.7	0.0322	0.004	21.83	0.3	0.1072	0.012
	120	10%	23.38	1.4	0.0327	0.005	21.75	0.4	0.1072	0.013
		5%	23.42	1.3	0.0324	0.004	21.74	0.3	0.1071	0.012
	150	10%	23.96	1.9	0.0391	0.005	22.14	0.3	0.1173	0.013
		5%	23.84	1.5	0.0389	0.004	22.14	0.2	0.1175	0.013
Block	0	10%	27.29	22.6	0.0388	0.012	21.71	0.9	0.1023	0.016
		5%	24.44	1.7	0.0534	0.012	21.39	0.8	0.0825	0.015
	30	10%	24.91	3.8	0.0426	0.011	21.31	0.9	0.0971	0.015
		5%	22.35	1.3	0.0558	0.013	22.14	1.1	0.0818	0.015
	60	10%	23.03	3.2	0.0367	0.011	21.76	1.1	0.1045	0.015
		5%	22.69	5.2	0.05	0.013	21.86	1.1	0.0865	0.015
	90	10%	22.84	2	0.0368	0.008	21.86	1	0.1009	0.014
		5%	22.36	1.5	0.0538	0.012	22.35	1	0.0816	0.015
	120	10%	26.29	20.7	0.0355	0.011	21.36	0.9	0.0982	0.017
		5%	23.2	1.6	0.0517	0.011	21.28	1.1	0.0807	0.016
	150	10%	33.46	109.5	0.0472	0.015	22.15	0.9	0.1061	0.015
		5%	23.97	2.7	0.0586	0.016	21.96	0.8	0.089	0.015

Table A.5: Mean phosphorescence lifetime and intensity values and their corresponding values for the GN_2 ventilation times of 0, 30, 60, 90, 120, 150 seconds and for 10% and 5% compression ratios. D1 was GN_2 ventilated, while D2 was not.

	sec	CR	**D1**				D2			
			$\overline{\tau}(\mu s)$	$\sigma_{\overline{\tau}}(\mu s)$	$\overline{I}$	$\sigma_{\overline{I}}$	$\overline{\tau}(\mu s)$	$\sigma_{\overline{\tau}}(\mu s)$	$\overline{I}$	$\sigma_{\overline{I}}$
Walsh	0	10%	21.14	1.3	0.0779	0.023	24.69	0.7	0.0949	0.025
		5%	21.08	1	0.0787	0.022	24.66	0.4	0.0964	0.026
	30	10%	21.13	0.6	0.0782	0.022	24.5	0.6	0.0956	0.027
		5%	21.07	0.5	0.0786	0.022	24.55	0.4	0.0964	0.027
	60	10%	20.98	0.5	0.0771	0.021	24.71	0.8	0.0959	0.026
		5%	21.96	0.2	0.112	0.013	23.52	1.3	0.0373	0.004
	90	10%	21.17	0.7	0.0769	0.021	24.59	0.6	0.0937	0.026
		5%	21.18	0.6	0.0776	0.021	24.62	0.4	0.0942	0.026
	120	10%	21.7	0.5	0.0966	0.024	24.36	0.6	0.1007	0.028
		5%	21.6	0.6	0.098	0.029	24.42	0.5	0.1011	0.03
	150	10%	21.01	2.1	0.0755	0.026	24.57	0.6	0.0917	0.025
		5%	21.08	1.1	0.0762	0.025	24.64	0.6	0.0929	0.025
Block	0	10%	21.67	1.3	0.0875	0.022	24.75	1.9	0.0845	0.018
		5%	21.85	1.2	0.0935	0.02	25.46	14.8	0.0789	0.016
	30	10%	21.46	1.4	0.0858	0.019	24.7	1.6	0.094	0.019
		5%	21.64	0.8	0.0906	0.017	24.84	1.1	0.088	0.019
	60	10%	21.57	5.7	0.0842	0.018	25.97	25	0.0876	0.017
		5%	21.79	0.8	0.0964	0.017	24.57	1.6	0.0771	0.016
	90	10%	21.37	1.7	0.0872	0.02	24.88	1.4	0.0845	0.016
		5%	21.42	1	0.0977	0.021	25.04	2.7	0.0715	0.017
	120	10%	25.62	65.3	0.0873	0.02	24.96	1.6	0.0823	0.017
		5%	21.5	1	0.0966	0.02	24.99	1.3	0.0727	0.018
	150	10%	21.6	2	0.0829	0.023	24.8	1.9	0.0816	0.017
		5%	22.09	1.1	0.09	0.02	25.38	12.7	0.0712	0.02

Table A.6: Mean phosphorescence lifetime and intensity values and their corresponding values for the GN_2 ventilation times of 0, 30, 60, 90, 120, 150 seconds and for 10% and 5% compression ratios. D1 and D2 were both GN_2 ventilated.

	sec	CR	**D1**				**D2**			
			$\overline{\tau}(\mu s)$	$\sigma_{\overline{\tau}}(\mu s)$	$\overline{I}$	$\sigma_{\overline{I}}$	$\overline{\tau}(\mu s)$	$\sigma_{\overline{\tau}}(\mu s)$	$\overline{I}$	$\sigma_{\overline{I}}$
Walsh	0	10%	22.34	0.6	0.0699	0.024	23.43	0.8	0.0612	0.011
		5%	22.32	0.4	0.0704	0.018	23.38	0.7	0.0585	0.012
	30	10%	22.19	0.7	0.0668	0.022	23.17	0.9	0.0585	0.011
		5%	22.18	0.4	0.0673	0.016	23.16	0.6	0.056	0.011
	60	10%	22.17	0.6	0.0667	0.022	23.18	0.9	0.059	0.011
		5%	22.19	0.4	0.0672	0.016	23.09	0.6	0.0565	0.012
	90	10%	22.15	0.6	0.0681	0.022	23.26	1	0.0595	0.011
		5%	22.17	0.4	0.0687	0.016	23.15	0.7	0.0567	0.011
	120	10%	22.16	1	0.0629	0.022	23.42	0.9	0.0584	0.012
		5%	22.17	0.6	0.0635	0.018	23.32	0.5	0.0564	0.013
	150	10%	22.04	0.6	0.0652	0.021	23.11	0.8	0.0583	0.012
		5%	22.09	0.4	0.0656	0.015	23.04	0.6	0.0561	0.012
Block	0	10%	20.63	1	0.0738	0.013	24.64	1.3	0.078	0.018
		5%	21.35	0.9	0.0815	0.013	24.56	1.6	0.0687	0.019
	30	10%	20.93	1.4	0.0695	0.015	23.65	1.4	0.0745	0.017
		5%	21.09	1	0.0745	0.016	23.78	1.2	0.0673	0.014
	60	10%	10.09	205.8	0.0731	0.018	24.5	1.6	0.0708	0.016
		5%	21.18	1	0.0833	0.017	24.67	1.9	0.0587	0.017
	90	10%	20.71	1.2	0.0742	0.017	25.94	12.8	0.0672	0.014
		5%	21.13	0.9	0.0783	0.016	25.02	13.9	0.0622	0.015
	120	10%	20.79	1	0.0688	0.017	24.28	1.8	0.0718	0.014
		5%	21.27	2.3	0.0728	0.018	23.84	1.2	0.0689	0.015
	150	10%	20.53	2	0.0718	0.017	24.52	2	0.0667	0.016
		5%	20.93	1	0.0787	0.017	24.48	2.5	0.06	0.014

Table A.7: Mean phosphorescence lifetime and intensity values and their corresponding values for the GN_2 ventilation times of 0, 30, 60, 90, 120, 150 seconds and for 10% and 5% compression ratios. D2 was GN_2 ventilated, while D1 was not.

	sec	CR	D1				**D2**			
			$\overline{\tau}(\mu s)$	$\sigma_{\overline{\tau}}(\mu s)$	$\overline{I}$	$\sigma_{\overline{I}}$	$\overline{\tau}(\mu s)$	$\sigma_{\overline{\tau}}(\mu s)$	$\overline{I}$	$\sigma_{\overline{I}}$
Walsh	0	10%	20.81	0.8	0.0712	0.021	24.51	0.4	0.0942	0.022
		5%	20.82	0.6	0.072	0.02	24.49	0.4	0.0941	0.023
	30	10%	20.72	0.7	0.0675	0.021	24.35	0.7	0.0915	0.022
		5%	20.78	0.7	0.0682	0.02	24.36	0.4	0.0925	0.02
	60	10%	20.86	0.7	0.0691	0.02	24.45	0.5	0.0912	0.022
		5%	20.77	0.5	0.0697	0.019	24.45	0.4	0.0921	0.021
	90	10%	20.76	0.7	0.0679	0.021	24.53	0.7	0.0901	0.021
		5%	20.72	0.6	0.0684	0.019	24.49	0.4	0.091	0.02
	120	10%	20.78	0.7	0.0674	0.02	24.37	0.6	0.0896	0.021
		5%	20.79	0.5	0.0679	0.019	24.36	0.4	0.0905	0.02
	150	10%	20.55	0.8	0.0672	0.02	24.43	0.5	0.0904	0.021
		5%	20.55	0.5	0.0678	0.019	24.41	0.5	0.0913	0.02
Block	0	10%	20.89	1.4	0.076	0.018	24.82	1.7	0.083	0.016
		5%	21.69	0.9	0.0852	0.017	24.98	1.4	0.0702	0.015
	30	10%	21.74	2.1	0.0845	0.018	25.29	10.5	0.0701	0.019
		5%	22.09	1.9	0.088	0.017	24.36	1.8	0.0654	0.018
	60	10%	21.29	3.3	0.0784	0.018	25.02	1.8	0.0745	0.017
		5%	21.58	0.9	0.0838	0.018	24.25	1.6	0.0701	0.017
	90	10%	21.65	0.9	0.0832	0.02	25.06	7	0.0712	0.018
		5%	21.78	0.8	0.0929	0.018	27.71	48.4	0.0617	0.019
	120	10%	17.77	68.9	0.0797	0.017	25.33	2.1	0.0711	0.016
		5%	21.72	2.5	0.0899	0.02	25.76	3.9	0.0631	0.015
	150	10%	20.81	1.7	0.0762	0.016	24.8	2.8	0.0789	0.018
		5%	21.19	0.9	0.0847	0.016	24.67	1.5	0.0693	0.017

Table A.8: Mean phosphorescence lifetime and intensity values and their corresponding values for the GN_2 ventilation times of 0, 30, 60, 90, 120, 150 seconds and for 10% and 5% compression ratios. D2 was GN_2 ventilated, while D1 was not.

	sec	CR	**D2**				D1			
			$\overline{\tau}(\mu s)$	$\sigma_{\overline{\tau}}(\mu s)$	$\overline{I}$	$\sigma_{\overline{I}}$	$\overline{\tau}(\mu s)$	$\sigma_{\overline{\tau}}(\mu s)$	$\overline{I}$	$\sigma_{\overline{I}}$
Walsh	0	10%	24.71	0.6	0.0923	0.016	21.1	0.3	0.097	0.014
		5%	24.69	0.4	0.0925	0.015	21.09	0.3	0.0955	0.011
	30	10%	24.53	0.7	0.0919	0.017	20.97	0.4	0.0957	0.013
		5%	24.5	0.4	0.0919	0.016	20.91	0.3	0.0942	0.011
	60	10%	24.38	0.7	0.0893	0.017	21.02	0.4	0.0933	0.013
		5%	24.31	0.6	0.0896	0.016	21.03	0.3	0.0918	0.011
	90	10%	24.33	0.6	0.0869	0.018	20.89	0.4	0.0934	0.013
		5%	24.34	0.5	0.0866	0.016	20.91	0.3	0.0919	0.011
	120	10%	24.32	0.7	0.0881	0.017	20.88	0.4	0.0942	0.013
		5%	24.35	0.6	0.0877	0.016	20.85	0.3	0.0927	0.011
	150	10%	24.49	1	0.0885	0.018	20.87	0.4	0.0936	0.013
		5%	24.46	0.8	0.0879	0.017	20.85	0.4	0.0923	0.011
Block	0	10%	24.42	1.3	0.0993	0.016	20.59	1.8	0.0766	0.013
		5%	25.53	25.6	0.1108	0.016	20.88	1.9	0.0635	0.013
	30	10%	25.45	16.9	0.0966	0.019	20.7	3.4	0.0771	0.015
		5%	24.17	2.8	0.1062	0.02	20.44	1.3	0.0682	0.014
	60	10%	24.43	4.4	0.0969	0.023	20.53	1.2	0.0725	0.01
		5%	23.76	1	0.1025	0.022	21.02	1.4	0.0661	0.011
	90	10%	25.04	9	0.092	0.016	20.81	3.4	0.0749	0.012
		5%	15.21	126.8	0.0949	0.018	20.64	1.2	0.0719	0.009
	120	10%	24.22	1.7	0.0932	0.015	20.73	1.2	0.0773	0.014
		5%	24.39	1.3	0.1017	0.019	20.87	1.2	0.0704	0.014
	150	10%	23.51	1.1	0.097	0.018	20.78	1.4	0.0708	0.013
		5%	25.26	39	0.1029	0.019	21.53	1.3	0.0637	0.013

Table A.9: Mean phosphorescence lifetime and intensity values and their corresponding values for the GN_2 ventilation times of 0, 30, 60, 90, 120, 150 seconds and for 10% and 5% compression ratios. D2 and D1 were both GN_2 ventilated.

	sec	CR	**D2**				**D1**			
			$\overline{\tau}(\mu s)$	$\sigma_{\overline{\tau}}(\mu s)$	$\overline{I}$	$\sigma_{\overline{I}}$	$\overline{\tau}(\mu s)$	$\sigma_{\overline{\tau}}(\mu s)$	$\overline{I}$	$\sigma_{\overline{I}}$
Walsh	0	10%	23.66	2	0.0595	0.013	22.42	0.4	0.1022	0.024
		5%	23.34	0.9	0.0567	0.013	22.4	0.4	0.0999	0.024
	30	10%	23.13	1	0.0568	0.013	22.25	0.3	0.0976	0.023
		5%	23.13	0.7	0.0543	0.013	22.3	0.3	0.0957	0.023
	60	10%	23.19	1.1	0.0545	0.013	22.2	0.4	0.0982	0.023
		5%	23.18	0.9	0.0526	0.013	22.21	0.3	0.0959	0.023
	90	10%	23.17	1.2	0.0559	0.013	22.08	0.4	0.0967	0.023
		5%	23.09	0.8	0.0539	0.013	22.1	0.3	0.0945	0.023
	120	10%	23.41	1.1	0.0558	0.015	22.21	0.5	0.0972	0.023
		5%	23.33	0.8	0.0542	0.013	22.18	0.3	0.0955	0.024
	150	10%	23.86	2.4	0.0598	0.018	22.15	0.4	0.096	0.022
		5%	23.74	0.8	0.0603	0.021	22.13	0.3	0.094	0.023
Block	0	10%	23.11	1.8	0.0662	0.016	22.4	1.2	0.0918	0.025
		5%	23.1	1.3	0.0745	0.015	22.75	0.9	0.0771	0.022
	30	10%	24.16	2.6	0.0613	0.015	21.6	1.3	0.087	0.029
		5%	23.25	1.2	0.0762	0.017	21.68	1.4	0.0667	0.023
	60	10%	23.94	2.8	0.0541	0.012	21.78	1.2	0.0907	0.026
		5%	23.39	2.2	0.068	0.014	22	1.8	0.0708	0.022
	90	10%	23.03	1.6	0.0584	0.012	22.05	2.2	0.0878	0.03
		5%	22.41	1.2	0.0733	0.013	26.46	59.8	0.068	0.023
	120	10%	24.36	4.9	0.0569	0.013	21.29	1.1	0.0888	0.026
		5%	23.49	1.2	0.0719	0.014	21.35	1	0.07	0.021
	150	10%	25.04	12.5	0.0683	0.021	21.94	1.1	0.0882	0.025
		5%	23.49	1.4	0.0807	0.022	21.75	1.4	0.073	0.023

Table A.10: Mean phosphorescence lifetime and intensity values and their corresponding values for the GN_2 ventilation times of 0, 30, 60, 90, 120, 150 seconds and for 10% and 5% compression ratios. D1 was GN_2 ventilated, while D2 was not.

	sec	CR	D2				**D1**			
			$\overline{\tau}(\mu s)$	$\sigma_{\overline{\tau}}(\mu s)$	$\overline{I}$	$\sigma_{\overline{I}}$	$\overline{\tau}(\mu s)$	$\sigma_{\overline{\tau}}(\mu s)$	$\overline{I}$	$\sigma_{\overline{I}}$
Walsh	0	10%	24.43	0.6	0.087	0.015	20.74	0.4	0.088	0.012
		5%	24.4	0.5	0.0875	0.017	20.71	0.3	0.0867	0.01
	30	10%	24.53	0.6	0.0845	0.015	20.7	0.4	0.0849	0.013
		5%	24.53	0.6	0.0846	0.014	20.7	0.3	0.0836	0.01
	60	10%	24.45	0.7	0.081	0.016	20.52	0.4	0.0854	0.012
		5%	24.41	0.8	0.0795	0.015	20.52	0.3	0.084	0.009
	90	10%	24.43	1.7	0.0804	0.016	20.6	0.5	0.0844	0.011
		5%	24.42	1.5	0.0797	0.014	20.59	0.4	0.0828	0.009
	120	10%	24.65	2	0.0799	0.016	20.54	0.5	0.0837	0.012
		5%	24.74	1.5	0.0794	0.015	20.52	0.3	0.0824	0.01
	150	10%	24.34	0.7	0.0807	0.016	20.6	0.5	0.0843	0.012
		5%	24.33	0.7	0.0797	0.014	20.58	0.3	0.0831	0.01
Block	0	10%	23.94	1.4	0.0972	0.02	20.51	1.5	0.0618	0.012
		5%	23.23	0.8	0.1026	0.018	20.53	2.5	0.0554	0.016
	30	10%	23.86	1.1	0.0964	0.017	20.56	1.1	0.0642	0.011
		5%	23.8	0.9	0.0995	0.019	19.64	1.4	0.0577	0.008
	60	10%	24.37	1.3	0.0896	0.018	20.53	1.3	0.0649	0.009
		5%	24.33	1.5	0.0946	0.018	20.16	0.9	0.0599	0.009
	90	10%	23.83	2.1	0.0899	0.016	20.87	2.9	0.0659	0.011
		5%	22.98	0.7	0.0931	0.018	21.01	2.6	0.0608	0.011
	120	10%	16.2	148.8	0.0824	0.016	22.69	21.6	0.0674	0.01
		5%	23.76	2	0.0875	0.015	20.76	1.1	0.0635	0.01
	150	10%	24.11	1.2	0.0856	0.017	19.82	1.4	0.0663	0.011
		5%	23.92	1.1	0.094	0.016	20.07	1.2	0.0599	0.013

Table A.11: Mean phosphorescence lifetime and intensity values and their corresponding values for the GN_2 ventilation times of 0, 30, 60, 90, 120, 150 seconds and for 10% and 5% compression ratios. D2 was GN_2 ventilated, while D3 was not.

	sec	CR	**D2**				D3			
			$\overline{\tau}(\mu s)$	$\sigma_{\overline{\tau}}(\mu s)$	$\overline{I}$	$\sigma_{\overline{I}}$	$\overline{\tau}(\mu s)$	$\sigma_{\overline{\tau}}(\mu s)$	$\overline{I}$	$\sigma_{\overline{I}}$
Walsh	0	10%	23.29	0.8	0.0666	0.017	23.09	1.1	0.0309	0.004
		5%	23.23	0.7	0.0653	0.016	23.03	0.7	0.0302	0.003
	30	10%	23.29	0.9	0.0629	0.015	23.19	1	0.029	0.003
		5%	23.25	0.7	0.0617	0.015	23.16	0.7	0.0292	0.003
	60	10%	23.26	0.8	0.0648	0.015	22.98	0.9	0.0301	0.004
		5%	23.19	0.7	0.0634	0.015	22.97	0.8	0.0295	0.003
	90	10%	23.28	1.2	0.0637	0.019	22.99	1	0.0297	0.003
		5%	23.22	1.2	0.0623	0.019	22.92	0.9	0.029	0.003
	120	10%	23.19	0.8	0.0633	0.016	22.95	0.9	0.0292	0.003
		5%	23.18	0.7	0.062	0.016	22.91	0.7	0.0286	0.003
	150	10%	23.35	0.8	0.0639	0.015	22.84	1	0.0287	0.003
		5%	23.36	0.6	0.0626	0.015	22.76	0.7	0.0281	0.003
Block	0	10%	24.36	0.9	0.0791	0.014	23.41	2.2	0.0413	0.008
		5%	24.2	1	0.0805	0.012	23.42	1.2	0.0404	0.009
	30	10%	24.16	1.1	0.0787	0.014	24.67	2.2	0.0427	0.009
		5%	24.4	1.1	0.0732	0.011	23.46	1.7	0.046	0.009
	60	10%	24.12	0.9	0.0802	0.011	23.75	1.7	0.0416	0.01
		5%	23.82	0.8	0.0753	0.01	24.21	1.4	0.0441	0.008
	90	10%	24.23	0.9	0.085	0.012	23.53	2.9	0.0386	0.008
		5%	23.98	0.7	0.0824	0.012	23.77	2	0.0384	0.009
	120	10%	24.36	1.4	0.0768	0.012	23.47	2	0.043	0.007
		5%	24.61	1	0.0718	0.01	22.79	1	0.0466	0.009
	150	10%	24.3	1.3	0.0773	0.012	23.49	3.2	0.042	0.007
		5%	24.03	0.9	0.0803	0.01	24.6	14.6	0.0371	0.007

Table A.12: Mean phosphorescence lifetime and intensity values and their corresponding values for the GN_2 ventilation times of 0, 30, 60, 90, 120, 150 seconds and for 10% and 5% compression ratios. D2 and D3 were both GN_2 ventilated.

	sec	CR	**D2**				**D3**			
			$\overline{\tau}(\mu s)$	$\sigma_{\overline{\tau}}(\mu s)$	$\overline{I}$	$\sigma_{\overline{I}}$	$\overline{\tau}(\mu s)$	$\sigma_{\overline{\tau}}(\mu s)$	$\overline{I}$	$\sigma_{\overline{I}}$
Walsh	0	10%	23.72	0.6	0.0587	0.016	22.25	1	0.0254	0.003
		5%	23.83	0.6	0.0581	0.017	22.29	0.9	0.0248	0.003
	30	10%	23.82	1.1	0.0586	0.017	22.45	1.1	0.0247	0.003
		5%	23.86	0.7	0.0585	0.019	22.54	1.4	0.0241	0.003
	60	10%	23.36	1	0.0595	0.017	22.38	1	0.0237	0.003
		5%	23.35	1.3	0.058	0.016	22.32	1.1	0.0231	0.003
	90	10%	23.49	2.6	0.058	0.017	22.33	1	0.0234	0.003
		5%	23.32	1.5	0.0566	0.016	22.37	1	0.0228	0.003
	120	10%	23.49	1	0.059	0.017	22.2	1.1	0.0226	0.003
		5%	23.44	1.1	0.0575	0.016	22.17	0.8	0.0221	0.003
	150	10%	23.59	1	0.0611	0.019	21.91	1.1	0.0226	0.003
		5%	23.57	1.5	0.0595	0.018	21.89	0.8	0.022	0.003
Block	0	10%	23.65	1.4	0.0594	0.017	23.15	5.3	0.0226	0.004
		5%	23.38	1.3	0.0548	0.015	23.49	2.3	0.0259	0.005
	30	10%	23.91	1.4	0.0611	0.018	21.65	2.8	0.0214	0.006
		5%	23.95	1.4	0.0604	0.016	22.03	3.4	0.0219	0.004
	60	10%	22.82	1.7	0.0614	0.017	25.18	13.5	0.0211	0.006
		5%	22.35	1.6	0.0638	0.017	23.53	118.3	0.0167	0.007
	90	10%	22.52	1.4	0.0591	0.017	24.24	3.4	0.0198	0.006
		5%	22.41	1.4	0.0599	0.015	23.22	3.2	0.0185	0.006
	120	10%	22.93	1.3	0.0595	0.015	21.93	3.9	0.0211	0.006
		5%	22.63	1.2	0.0592	0.014	22.28	4.8	0.0204	0.006
	150	10%	22.77	1.7	0.0609	0.018	23.75	3.9	0.0204	0.006
		5%	22.94	1.5	0.0597	0.016	23.82	3.4	0.0199	0.008

Table A.13: Mean phosphorescence lifetime and intensity values and their corresponding values for the GN_2 ventilation times of 0, 30, 60, 90, 120, 150 seconds and for 10% and 5% compression ratios. D3 was GN_2 ventilated, while D2 was not.

	sec	CR	D2				**D3**			
			$\overline{\tau}(\mu s)$	$\sigma_{\overline{\tau}}(\mu s)$	$\overline{I}$	$\sigma_{\overline{I}}$	$\overline{\tau}(\mu s)$	$\sigma_{\overline{\tau}}(\mu s)$	$\overline{I}$	$\sigma_{\overline{I}}$
Walsh	0	10%	23.43	0.9	0.0665	0.015	22.77	1	0.0286	0.003
		5%	23.24	0.6	0.0649	0.015	22.76	0.9	0.0283	0.002
	30	10%	23.43	1	0.0609	0.016	22.65	0.9	0.0269	0.003
		5%	23.35	0.7	0.0594	0.015	22.64	0.7	0.0266	0.003
	60	10%	23.47	1	0.0603	0.016	22.69	1	0.0269	0.003
		5%	23.35	0.9	0.059	0.015	22.67	0.7	0.0265	0.003
	90	10%	23.35	0.8	0.0613	0.016	22.43	1.1	0.0256	0.003
		5%	23.27	0.8	0.06	0.015	22.39	0.7	0.0253	0.003
	120	10%	23.57	1	0.0594	0.015	22.7	1	0.0257	0.003
		5%	23.45	0.7	0.058	0.015	22.66	0.6	0.0254	0.003
	150	10%	23.4	0.9	0.0598	0.015	22.55	1	0.0252	0.003
		5%	23.37	0.8	0.0583	0.015	22.54	0.8	0.0249	0.003
Block	0	10%	24.26	0.9	0.08	0.012	23.69	1.8	0.0396	0.008
		5%	24.18	0.8	0.084	0.012	23.63	2.9	0.0328	0.007
	30	10%	24.34	1	0.079	0.014	24.21	16	0.037	0.008
		5%	23.95	0.9	0.0772	0.013	24.23	2	0.0366	0.009
	60	10%	23.91	1	0.0798	0.012	24.38	2.9	0.036	0.008
		5%	23.98	0.9	0.0783	0.011	24.15	1.5	0.0346	0.008
	90	10%	24.08	1	0.078	0.012	23.97	2.4	0.0401	0.01
		5%	23.25	0.8	0.0806	0.012	25.5	3.7	0.0354	0.009
	120	10%	24.11	1	0.0767	0.014	25.76	19.8	0.0401	0.008
		5%	24.07	0.8	0.0764	0.012	23.8	1.9	0.0391	0.008
	150	10%	24.68	1.3	0.078	0.013	22.87	2.3	0.0369	0.009
		5%	24.52	0.8	0.079	0.011	23.08	2.1	0.0343	0.009

Table A.14: Mean phosphorescence lifetime and intensity values and their corresponding values for the GN_2 ventilation times of 0, 30, 60, 90, 120, 150 seconds and for 10% and 5% compression ratios. D3 was GN_2 ventilated, while D2 was not.

	sec	CR	**D3**				D2			
			$\overline{\tau}(\mu s)$	$\sigma_{\overline{\tau}}(\mu s)$	$\overline{I}$	$\sigma_{\overline{I}}$	$\overline{\tau}(\mu s)$	$\sigma_{\overline{\tau}}(\mu s)$	$\overline{I}$	$\sigma_{\overline{I}}$
Walsh	0	10%	23.22	0.9	0.0401	0.006	24.1	0.4	0.0795	0.009
		5%	23.2	0.6	0.0394	0.004	24.11	0.3	0.0784	0.008
	30	10%	23.51	0.7	0.0393	0.006	24.1	0.5	0.0797	0.009
		5%	23.61	1	0.0388	0.005	24.08	0.3	0.0785	0.008
	60	10%	23.4	0.8	0.0396	0.006	24.04	0.4	0.0793	0.009
		5%	23.4	0.7	0.039	0.005	24.04	0.3	0.0782	0.008
	90	10%	23.35	1	0.0401	0.006	24.05	0.4	0.0786	0.009
		5%	23.31	0.6	0.0394	0.005	24.04	0.3	0.0776	0.008
	120	10%	23.58	0.9	0.0393	0.005	23.97	0.4	0.0782	0.009
		5%	23.58	0.6	0.0387	0.005	23.98	0.3	0.0772	0.008
	150	10%	23.49	0.8	0.04	0.005	24.03	0.4	0.078	0.009
		5%	23.4	0.7	0.0394	0.005	24.03	0.3	0.0769	0.008
Block	0	10%	31.75	66.4	0.0148	0.005	22.86	1.5	0.0635	0.01
		5%	23.81	2.2	0.0267	0.006	26	183.7	0.0488	0.011
	30	10%	26.8	8.2	0.0199	0.005	22.43	1.7	0.0536	0.01
		5%	24.17	2.4	0.0294	0.006	22.31	1.6	0.0409	0.008
	60	10%	27.84	27.1	0.0174	0.005	22.41	1.3	0.056	0.01
		5%	24.71	3.6	0.0269	0.008	22.79	3.4	0.0436	0.009
	90	10%	30.77	29.4	0.0164	0.004	22.41	1.4	0.0549	0.011
		5%	23.02	1.7	0.0282	0.006	22.55	1.5	0.0402	0.007
	120	10%	24.17	3.5	0.0184	0.005	22.43	1.3	0.055	0.01
		5%	22.92	1.6	0.0289	0.005	22.29	1.6	0.0415	0.008
	150	10%	24.63	4.9	0.0194	0.005	22.87	1.2	0.0604	0.015
		5%	22.55	1.6	0.0342	0.007	23.16	1.8	0.0446	0.012

Table A.15: Mean phosphorescence lifetime and intensity values and their corresponding values for the GN_2 ventilation times of 0, 30, 60, 90, 120, 150 seconds and for 10% and 5% compression ratios. D3 and D2 were both GN_2 ventilated.

	sec	CR	**D3**				**D2**			
			$\overline{\tau}(\mu s)$	$\sigma_{\overline{\tau}}(\mu s)$	$\overline{I}$	$\sigma_{\overline{I}}$	$\overline{\tau}(\mu s)$	$\sigma_{\overline{\tau}}(\mu s)$	$\overline{I}$	$\sigma_{\overline{I}}$
Walsh	0	10%	22.7	1.5	0.0154	0.004	23.56	1.1	0.0594	0.013
		5%	22.7	1.3	0.0153	0.002	23.47	0.5	0.0577	0.013
	30	10%	22.41	1.8	0.0152	0.004	23.54	0.8	0.0601	0.013
		5%	22.18	1.4	0.0153	0.003	23.36	0.5	0.0584	0.013
	60	10%	22.39	1.7	0.0151	0.003	23.59	0.9	0.0599	0.013
		5%	22.38	1.6	0.015	0.003	23.48	0.6	0.0582	0.013
	90	10%	19.9	48.8	0.0142	0.003	23.39	1	0.0586	0.013
		5%	22	1.4	0.0142	0.002	23.32	0.6	0.0569	0.013
	120	10%	22.11	1.8	0.0139	0.003	23.4	0.9	0.0593	0.013
		5%	21.91	1.5	0.014	0.003	23.37	0.6	0.0575	0.013
	150	10%	21.92	1.6	0.0142	0.003	23.6	0.9	0.06	0.014
		5%	21.93	1.8	0.0141	0.002	23.52	0.6	0.0583	0.014
Block	0	10%	23.8	1.9	0.0454	0.007	24	1.3	0.0696	0.01
		5%	23.54	1.1	0.0506	0.007	24.13	0.9	0.059	0.012
	30	10%	24.76	13.4	0.0418	0.009	23.75	1.2	0.0718	0.011
		5%	23.79	1.1	0.0535	0.009	24.04	1.6	0.055	0.013
	60	10%	25.07	13.8	0.0414	0.008	23.37	1.2	0.0711	0.011
		5%	23.58	1.4	0.0486	0.009	23.73	1.3	0.0615	0.012
	90	10%	18.08	116.8	0.0403	0.008	24.11	1.3	0.0706	0.01
		5%	23.7	1.1	0.0477	0.008	23.97	1.8	0.0599	0.011
	120	10%	23.69	3.3	0.0406	0.008	23.85	1.2	0.0725	0.011
		5%	23.72	1.2	0.0482	0.007	23.92	1.5	0.0626	0.012
	150	10%	23.6	2.2	0.0434	0.008	24.1	1.4	0.0682	0.011
		5%	23.96	1.2	0.049	0.007	23.7	1	0.0601	0.013

Table A.16: Mean phosphorescence lifetime and intensity values and their corresponding values for the GN_2 ventilation times of 0, 30, 60, 90, 120, 150 seconds and for 10% and 5% compression ratios. D2 was GN_2 ventilated, while D3 was not.

	sec	CR	D3				**D2**			
			$\overline{\tau}(\mu s)$	$\sigma_{\overline{\tau}}(\mu s)$	$\overline{I}$	$\sigma_{\overline{I}}$	$\overline{\tau}(\mu s)$	$\sigma_{\overline{\tau}}(\mu s)$	$\overline{I}$	$\sigma_{\overline{I}}$
Walsh	0	10%	23.65	5.2	0.0402	0.007	24.19	0.5	0.0798	0.008
		5%	23.29	0.8	0.0399	0.006	24.19	0.3	0.0794	0.006
	30	10%	23.38	0.9	0.0407	0.006	24.01	0.4	0.0778	0.008
		5%	23.36	0.7	0.0404	0.005	24.03	0.3	0.077	0.006
	60	10%	23.56	1.1	0.0393	0.005	24.02	0.4	0.0769	0.008
		5%	23.46	0.7	0.039	0.005	24.01	0.3	0.0761	0.006
	90	10%	23.56	1	0.04	0.005	24.06	0.5	0.0762	0.008
		5%	23.53	0.7	0.0398	0.004	24.05	0.3	0.0753	0.006
	120	10%	23.46	1	0.0397	0.005	23.92	0.4	0.0757	0.008
		5%	23.43	0.7	0.0394	0.004	23.93	0.3	0.0749	0.006
	150	10%	23.6	1	0.0398	0.005	23.81	0.5	0.0758	0.008
		5%	23.55	0.7	0.0394	0.004	23.81	0.4	0.0751	0.006
Block	0	10%	24.02	152.5	0.0193	0.005	22.46	1.4	0.0547	0.01
		5%	25.41	2.4	0.0296	0.005	21.95	1.5	0.0421	0.009
	30	10%	14.62	187.9	0.0193	0.006	22.47	1	0.0571	0.01
		5%	24.47	2.9	0.0258	0.004	22.13	1.4	0.0469	0.011
	60	10%	1.32	411.3	0.0198	0.006	22.49	1.2	0.055	0.009
		5%	24.27	3.8	0.0273	0.006	22.22	1.5	0.0452	0.009
	90	10%	24.89	6	0.0191	0.005	22.93	0.9	0.0576	0.009
		5%	23.52	2.3	0.0311	0.007	24.62	22.4	0.0425	0.01
	120	10%	23.89	4.6	0.0194	0.005	22.45	0.9	0.0538	0.01
		5%	24.65	3.9	0.0256	0.005	22.76	9.7	0.0453	0.009
	150	10%	25.38	5	0.0186	0.004	22.58	1.3	0.0594	0.011
		5%	22.64	1.7	0.0297	0.006	23.27	1.8	0.0456	0.01